University of Namur

DOCTOR OF SCIENCES

Designing and synthesis of hierarchically porous semiconductor materials for efficient pollutants elimination and sustainable energy evolution

DING, Yang

Award date:
2022

Awarding institution:
University of Namur

Link to publication

Université de Namur

Faculté des Sciences
DÉPARTEMENT DE CHIMIE
Laboratoire de Chimie des Matériaux Inorganiques

Designing and synthesis of hierarchically porous semiconductor materials for efficient pollutants elimination and sustainable energy evolution

- Version finale-

Dissertation présentée par
Yang Ding
en vue de l'obtention du grade
de Docteur en Sciences

Composition du jury:

Prof. Vincent Liègeois (Président, UNamur)
Prof. Alexandru Vlad (UCLouvain)
Prof. Olivier Deparis (UNamur)
Prof. Li-Hua Chen (WHUT)
Dr. Tarek Barakat (Vocalise)
Prof. Bao-Lian Su (UNamur, Promoteur)

October 2022

University of Namur
FACULTY OF SCIENCE
Rue de Bruxelles 61 - 5000 Namur
Phone: +32 491984794

Designing and synthesis of hierarchically porous semiconductor materials for efficient pollutants elimination and sustainable energy evolution

Yang Ding

Abstract

Currently, the environmental deterioration and energy shortage issues have appealed tremendous attention by scientists. The new technologies and devices to alleviate these problems such as catalysis, photocatalysis, and electrocatalysis have been intensively explored. In these regards, the exploitation of highly efficient materials is a core factor to achieve the goal of substituting traditional fuels with sustainable and clean energy, and achieve efficient pollutants treatment. As an important class of nano-structured materials, hierarchically porous semiconductor materials have aroused significant attention during the past decade. Compared with bulk materials, hierarchically porous semiconductor materials materials possess a series of merits including large specific surface area, rich surface active sites, convenient mass transportation channels. These intrinsic advantages ensure hierarchically porous semiconductor materials with huge application potentials in photocatalytic pollutants treatment and sustainable energy production.

In this thesis, we will talk about the utilization of a series of hierarchically porous semiconductor photocatalysts in environmental and energy fields. The relationship between the improved photocatalytic ability with the fabrication and utilization of hierarchically porous materials is thoroughly discussed. Moreover, the potentials and challenges for the large-scale industrial applications of hierarchically porous semiconductors are also outlooked.

1. The first work focus on the synthesis of a hydrophilic bi-functional hierarchical architecture by the assembly of B-doped g-C_3N_4 nanoplatelets. Such hierarchically porous B-doped g-C_3N_4 material enables full utilization of their highly enhanced visible light absorption and photogenerated carrier separation in aqueous medium, leading to an excellent photocatalytic H_2O_2 production rate and photoelectrochemical water splitting performance.

2. The second work report the visible-light H_2O_2 artificial photosynthesis by digging pro-superoxide radical carbon vacancies in three-dimensional hierarchical porous g-C_3N_4 through a simple hydrolysis-freeze-drying-thermal treatment. A significant electronic

structure change is revealed upon the implantation of carbon vacancies, broadening visible-light absorption and facilitating the photogenerated charge separation. The strong electron affinity of the carbon vacancies promotes superoxide radical formation, significantly boosting the H_2O_2 photocatalytic production

3. Finally, the ternary 3D ordered macroporous (3DOM) hybrid nanocomposites (platinum/bismuth molybdate/3DOM TiO_2: 3DOM-Pt/Bi_2MoO_6/TiO_2) are designed and synthesized as multifunctional platform for photocatalytic dye degradation, photoelectrocatalytic (PEC) water splitting, and thermal-catalytic toluene decomposition with high performance. A series of structural, optical, and electronic characterizations demonstrates that the remarkably improved photocatalytic degradation and PEC water splitting activities are attributed to the combined effects of enhanced light harvesting, abundant reactive sites, facile reactants transfer, and efficient charges-holes pair separation.

Essay submitted for the degree of Doctor of Science
October 2022
Supervisor: Prof. Bao-Lian Su

Contents

Chapter I

A literature survey for the applications of hierarchically porous semiconductor materials

Lots of works have been conducted to enhance the performances of hierarchically porous semiconductor materials in environmental and energy fields. In this chapter, a brief literature review is presented to introduce the research background and progress in hierarchically porous semiconductor materials. Meanwhile, the related applications regarding hierarchically porous semiconductors in energy and environmental fields are summarized. Finally, the aim and major research results of this thesis are discussed.

(In this chapter, some contents have been published on **EnergyChem 4 (2022) 100081** and **Interdisciplinary Materials 2022;1:213-255** by Yang Ding et al.)

1. Introduction

1.1 The background of hierarchically porous semiconductor materials

Currently, the environmental deterioration and energy shortage issues have appealed tremendous attention by scientists. The new technologies and devices to alleviate these problems such as catalysis, solar cells, Li ion batteries and super-capacitor have been intensively explored.[1-5] In these regards, the exploitation of highly efficient materials is a core factor to achieve the goal of substituting traditional fuels with sustainable and clean energy, and create advanced energy storage devices. Up to now, a variety of nano-structured materials including one-dimensional (1D) (like nanowires and nanotubes), two-dimensional (2D) (such as nanosheets), and three-dimensional (3D) architectures have been designed for efficient catalysts, solar cells and advanced energy storage systems (**Figure 1a**).[6-10] As an important class of nano-structured materials, hierarchically porous materials have aroused significant attention during the past decade. Compared with bulk materials, hierarchically porous materials possess a series of merits including large specific surface area, rich surface active sites, convenient mass transportation channels owing to their interpenetrating porous structure. Moreover, as specially hierarchically porous materials, three-dimensionally ordered macroporous (3DOM) materials, also display a unique slow photo effect for enhancing light utilization due to their periodic porous structure (**Figure 1b**).[11] These intrinsic advantages ensure hierarchically porous materials with huge application potentials in photocatalysis, electrocatalysis, solar cells, Li ion batteries and supercapacitor fields.[12-17] In terms of photocatalysis on semiconductors, the overall photocatalytic reaction rate mainly results from three kinetic parameters including the efficiency of light absorption (η_{abs}), the dissociation of photoinduced charge pairs (η_{sep}) and the surface electron transfer (η_{tran}),[18-20] which can be expressed as follows:$\eta_{total}=\eta_{abs} \times \eta_{sep} \times \eta_{tran}$ (**Figure 1c**).[20] All the three processes will be upgraded over hierarchically porous materials, thus bringing out the improved photocatalytic rate. Similar to photocatalysis, electrolysis is also determined by three steps: reactants absorption, migration of charges between catalysts and reactants, and exportation of charges from the electrodes and desorption of products.[18] These processes will be certainly accelerated on the hierarchically porous structure, thus leading to efficiently electrocatalytic reaction process. It is noteworthy that light absorption and formation of photogenerated carriers are not involved in the electrocatalytic process. Compared with the photocatalytic reactions using typical semiconductor materials like metal oxides and sulfides, the carbon-based materials and phosphide are frequently utilized in electrocatalytic reactions.

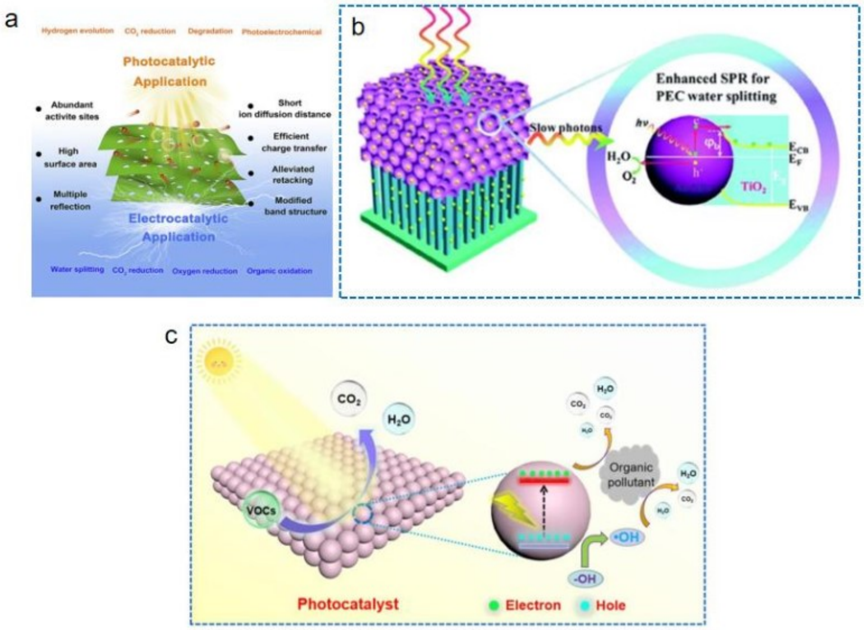

Figure 1. (a) The applications of hierarchically porous semiconductor materials in various photo- and electrocatalytic reactions. (b) Schematic illustration of the slow photos effect for promoting photocatalytic reaction on the 3DOM structured photocatalyst and (c) schematic process for the photocatalytic reaction on the surface of semiconductor photocatalyst.

1.2 The applications of hierarchically porous semiconductor materials

In this section, the utilization of hierarchically porous semiconductor materials in energy and environmental fields involving photocatalysis and electrocatalysis are thoroughly discussed. Meanwhile, the strategies for designing hierarchically porous semiconductor materials and the enhanced performances for applications are correlated, which can be significantly valuable to help readers to promptly acquire the comprehensive knowledge and to inspire new concepts in exploiting hierarchically porous semiconductor materials for further increased performances.

1.2.1. Photocatalytic applications

Photocatalytic technology holds a great potential for sustainable energy conversion.[21-25] So far, a variety of photocatalysts with different nanostructures have been manufactured for photocatalytic reactions.[26-31] Hierarchically porous semiconductor materials as photocatalysts have been extensively used in various reactions for sustainable energy conversion and pollutants treatment such as organics degradation, hydrogen production, CO_2 reduction, H_2O_2 production and organics photoreformation. In addition to their obvious advantages like high surface area and facile ions transfer channels, for the special 3DOM materials, their periodic inverse opal structure also endows the intrinsic photonic band gap and the slow photon effects can also exert important function for promoting photocatalytic reactions. Specifically, the light at specific wavelengths irradiating on the inverse opal structure along a certain angle leads to the stop-band reflection, being well known as photonic band gap. The light group velocity will decrease when light illuminates on 3DOM materials at their blue or red edge of the photonic band gap, which is attributed to the slow photon effects and results in the enhanced interaction between light and materials, giving rise to efficient harvesting of light and improved photocatalytic activity.[32-35] In this section, we outline a series of photocatalytic reactions including hydrogen production, CO_2 reduction, H_2O_2 production and organics photoreforming over hierarchically porous semiconductor materials.

1.2.1.1 Pollutants degradation

In fact, our group conducted lots of work in regard to photocatalytic pollutants degradation over 3DOM materials.[36-39] For example, a variety of $BiVO_4$/3DOM-TiO_2 photocatalysts were fabricated by combining various amounts of $BiVO_4$ with 3DOM TiO_2 for photocatalytic RhB degradation.[36] Pure $BiVO_4$ and $BiVO_4$/P25 as reference samples were also synthesized. It is found that the $BiVO_4$/3DOM-TiO_2 photocatalyst exhibits about 4.2, 3.2 and 3.1 folds higher visible light driven RhB degradation rates than that of $BiVO_4$, 3DOM TiO_2 and $BiVO_4$/P25 photocatalysts, respectively. The improved photocatalytic rate is ascribed to increased mass transfer, high surface area, efficient visible light absorption and intimate contact between $BiVO_4$ and 3DOM-TiO_2. Specifically, $BiVO_4$ as a sensitizer broadens light absorption edge of 3DOM-TiO_2 from 380 to 550 nm. Meanwhile, the formed heterostructure between $BiVO_4$ and 3DOM-TiO_2 can effectively promote photogenerated electron-hole pairs separation, and provides more reactive oxygen species like $\cdot O_2^-$ and $\cdot OH$ radicals for accelerating RhB decomposition. Similarly, ZnO quantum dots decorated 3DOM TiO_2 photocatalyst (ZnO/3DOM-TiO_2) was also fabricated (**Fig. 2a**).[37] Owing to the synergy of inverse opal structure and the heterostructure between ZnO and TiO_2, the efficient photocatalytic dye molecules decomposition is achieved on the ZnO/3DOM-TiO_2 photocatalyst.

As well as the binary $BiVO_4$/3DOM TiO_2 and ZnO/3DOM TiO_2 photocatalysts, a ternary ZnO/$BiVO_4$/3DOM-TiO_2 composite was also prepared for the enhanced photocatalytic RhB and Tartrazine degradation (**Fig. 2b-d**).[38] The inverse opal structure offers convenient channels for reactants transmission and multiple scattering for increased light utilization. Moreover, an innovative cascade energy level is formed in the ternary photocatalyst. Under visible light illumination, the electron-hole pairs are generated on $BiVO_4$ component and then the photoelectrons flow to ZnO and 3DOM-TiO_2 to form $\cdot O_2^-$ for decomposing dye molecules whereas the holes directly oxidize dye molecules. Thus, the cascade energy level promotes the electron-hole pairs dissociation and leads to an excellent photocatalytic dye molecules degradation rate (**Fig. 2e**).

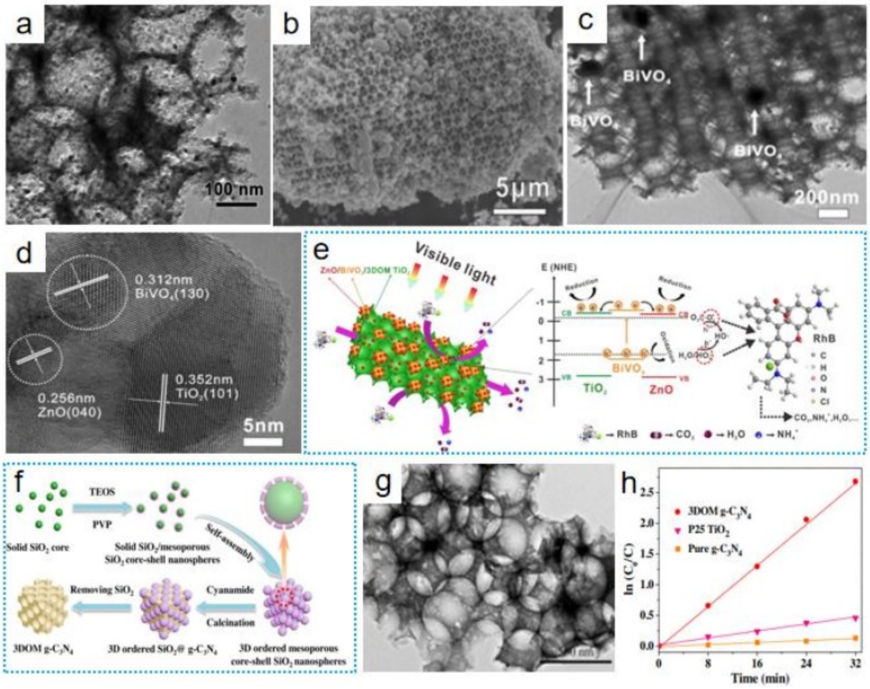

Fig. 2. (a) TEM picture of the prepared photocatalyst.[37] (b) SEM, (c) TEM and (d) HR-TEM pictures of the ternary photocatalyst; (e) illustrations of RhB degradation over the ternary photocatalyst and the corresponding photoelectrons transfer mechanism.[38] (f) Schematic preparation process of 3DOM g-C_3N_4, (g) TEM picture of 3DOM g-C_3N_4, and (h) RhB degradation over the as-prepared photocatalysts and commercial P25.[41]

In addition to dye molecules elimination, photocatalytic phenol degradation over 3DOM photocatalysts was also reported. Chen's team synthesized the ternary 3DOM CDs/Bi-TiO_2 photocatalyst by decorating carbon dots on the 3DOM Bi doped TiO_2.**[40]** Both Bi doping and CDs decorating can favor visible light utilization and promote photogenerated hole-electron pairs delocalization. Specifically, the impurity energy level stemming from Bi doping in TiO_2 prohibits photoinduced carriers recombination while the decorated CDs as electron collectors can effectively attract photoelectrons from CB of TiO_2 to participate in photoredox reaction. Moreover, the facile reactants transmission, the enhanced interaction between light and matter, and the slow photo effect originating from the 3DOM structure further elevate the photocatalytic ability. Finally, the 3DOM CDs/Bi-TiO_2 photocatalyst delivers 3.3 times higher photocatalytic phenol degradation rate than that of pure 3DOM TiO_2. Compared with 3DOM TiO_2, g-C_3N_4 with inverse opal structure is not easy to be prepared because the usual g-C_3N_4 is difficult to be filled into the voids of the templates. On account of this fact, Yang's team developed a thermal condensation-helped template strategy to synthesize the 3DOM g-C_3N_4.[41] As shown in **Fig 2f**, the 3D ordered mesoporous core-shell silica as template facilitates the precursor to merge into the cavities of SiO_2 array and prohibit the damage of active component during heating treatment. Accordingly, 3DOM g-C_3N_4 with the macropore diameter about 300 nm and mesopore diameter around 30 nm is obtained (**Fig. 2g**). Meanwhile, the 3DOM g-C_3N_4 displays around 2.5 times large surface area than that of bulk g-C_3N_4. The unique structure and large surface area endow rapid mass diffusion and transmission, multiple light scattering, plentiful surface active sites and efficient charge carriers delocalization. Moreover, the stronger adsorption for pollution molecules over the 3DOM g-C_3N_4 is also verified. Accounting of the above advantages, the 3DOM g-C_3N_4 photocatalyst exhibits about 5 times higher RhB photodegradation efficiency than that of bulk g-C_3N_4 (**Fig. 2h**). The holes and $\bullet O_2^-$ are found as the active radicals for RhB molecule decomposition. In addition to the increased mass and electrons transfer as well as high surface area, it is found that the active species like $\bullet O_2^-$ and $\cdot OH$ are prone to be formed on the 3DOM materials, thus further accelerating the organic pollutant degradation.

1.2.1.2. Hydrogen production

So far, 3DOM materials for photocatalytic hydrogen production have appealed numerous attention and great progresses have been achieved.**[50-61]** Typically, our group reported that a ternary photocatalyst 3DOM TiO_2-Au-CdS composite for increased photocatalytic H_2

formation was fabricated by loading Au nanoparticles and CdS crystallites on 3DOM TiO_2 (**Fig. 3a**).[50] The co-existence of Au nanoparticles and CdS brings out the wide light absorption to 600 nm due to the photosensitive effect of CdS and the surface plasmon effect of Au nanoparticles (**Fig. 3b**). Furthermore, the Au nanoparticles as active sites exert significant functions in photoelectrons collect and transfer (**Fig. 3c**), thus promoting the photoinduced carriers separation and the reduction of H^+ to form H_2. As depicted in **Fig. 3d**, the formed photoelectrons on the CB of TiO_2 can be migrated and connected with the holes of CdS by the Au bridge under UV-vis light illumination, the photoelectrons on the CB of CdS directly participate in hydrogen generation. Differently, the photoelectrons migration to the CB of TiO_2 from CdS through the Au bridge to take part in hydrogen reduction reaction under visible light. Both two photoelectrons transmission pathways can effectively promote electron-hole pairs separation and thus improve photocatalytic hydrogen production. Finally, 3DOM TiO_2-Au-CdS photocatalyst delivers 13 folds greater visible light driven hydrogen productivity about 1.8 mmol h^{-1} g^{-1} than that of 3DOM TiO_2-CdS photocatalyst. To further improve photocatalytic H_2 production, a series of ternary photocatalyst 3DOM TiO_2-Au-CdS photocatalysts with various macropore sizes about 160, 200, 250 and 340 nm were synthesized.[51] In this work, the relationship between slow photon and photocatalytic performance is investigated for the first time. As illustrated in **Fig 3e**, the 3DOM structure maintains the reflectance character at various light illumination angles, therefore, the influence of incident light angle on the photocatalytic H_2 formation over 3DOM TiO_2-Au-CdS photocatalyst is eliminated. As shown in light reflectance spectra, the photonic band gap of 3DOM TiO_2 is not changed after Au and CdS loading (**Fig. 3f**). However, modulating the macropore diameter of the 3DOM TiO_2-Au-CdS composites can effectively change their photonic band gap (**Fig. 3g**), meanwhile, the distinct peaks of reflectance spectra suggest the good crystallinity of these as-prepared 3DOM TiO_2-Au-CdS nanocomposites. It is well known that when the red-margin or blue-margin of the photonic band gap covers the bandgap absorption of photocatalysts, the slow photons effect is achieved to improve the excitation of photoelectrons and more carriers are formed, thus enhancing the photocatalytic activity. For the UV-Vis reflectance spectra, it is obvious that the red-margin of 3DOM TAC-160 and the blue-margin of 3DOM TAC-250 match with the absorption of CdS at around 250 nm, thus causing the slow photon effect and favoring the improved photocatalytic performance. As shown in **Fig 3h**, 3DOM TAC-250 shows the highest photocatalytic H_2 productivity of 3.5 mmol h^{-1} g^{-1} among all the as-synthesized samples. Significantly, 3DOM TAC-250 reflects photons with low energies and fully utilize high energy photons to activate

CdS to produce carriers, while 3DOM TAC-160 reflects high energy photons and absorbs low energy photons which can activate CdS to produce carriers. Hence, 3DOM TAC-250 possessing blue-margin slow photon effect brings out large hydrogen generation rate than that of 3DOM TAC-160 giving red-margin slow photon effect. Furthermore, the influence of the size of Au NPs in TiO_2-Au-CdS on photocatalytic performance was also studied. It is found that the ternary TiO_2-Au-CdS photocatalyst with about 10 nm Au NPs gives rise to the highest hydrogen evolution rate.**[52]** In summary, slow photo effect exerts significant roles in promoting photocatalytic hydrogen formation, the precise control of the sizes of macropores for acquiring the best light harvesting efficiency should be highly concerned in the future research.

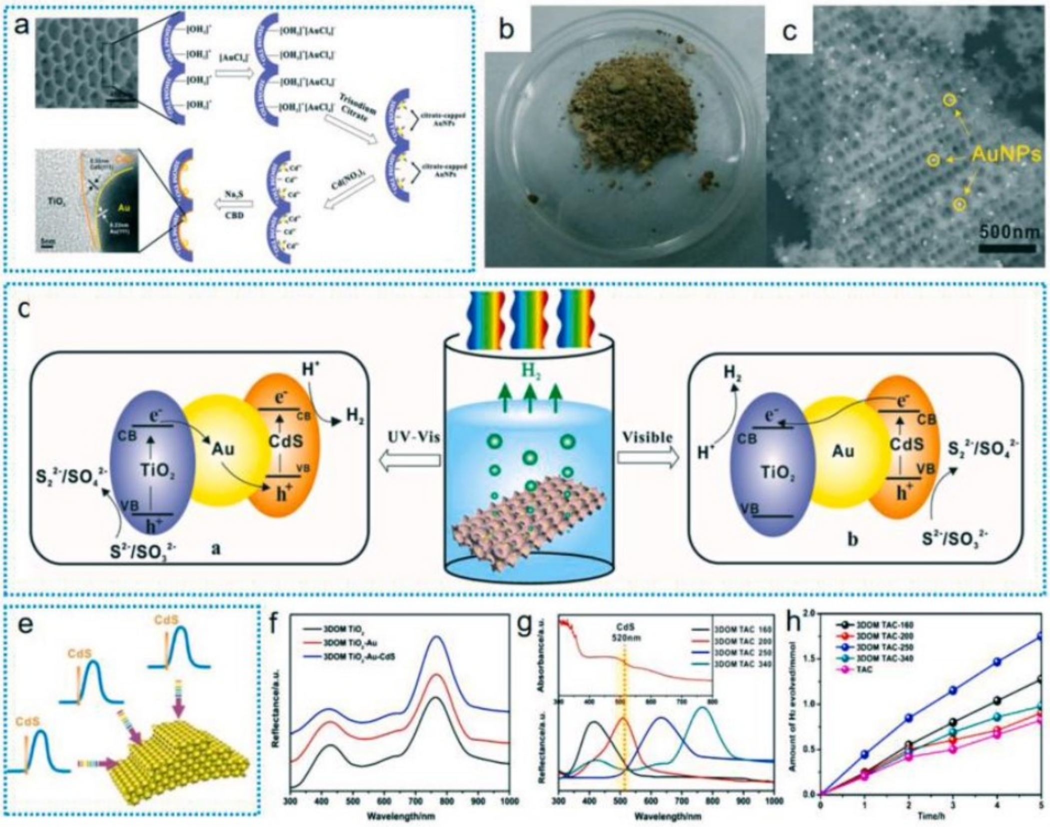

Fig. 3. (a) Schematic preparation route of the 3DOM TiO_2-Au-CdS photocatalyst, (b) photograph and (c) back scattered electron picture of as-prepared samples, and (d) the photocatalytic hydrogen production mechanism and photoelectrons transfer pathways over the photocatalyst under visible light and UV-Vis light illustrations.**[50]** (e) Schematic illustration of various incident light angles on 3DOM TiO2-Au-CdS, (f-g) light reflectance spectra of

different photocatalysts, and (h) time dependent photocatalytic hydrogen generation over the as-fabricated photocatalysts.**[51]**

1.2.1.3. CO_2 reduction

The crisis of energy shortage and CO_2 gas emission have appealed huge attention during the past few decades. The conversion CO_2 into the value-added organics and fuels via a photocatalytic reduction pathway has been intensively studied by scientists due to its facile, sustainable and environmentally friendly process.**[62-64]** However, the efficient photocatalytic CO_2 reduction still encounters from several bottlenecks, such as poor light conversion efficiency and low selectivity of products formation. Hence, designing highly efficient photocatalyst is a key factor in photocatalytic CO_2 reduction.**[65-68]** For example, SnS_2 loaded 3DOM-$SrTiO_3$ composite (SnS_2/3DOMSrTiO3) was prepared via a hydrothermal route for efficient photocatalytic CO_2 reduction (**Fig. 4a, b**).[62] The unique 3DOM structure of the composite delivers the slow light effect for improving visible light utilization and the abundant mass diffusion and transport channels, meanwhile the alkalis strontium favors the enhanced CO_2 adsorption. Moreover, the heterostructure between SnS_2 and 3DOM-$SrTiO_3$ provides a Z-scheme photoinduced charges transfer pathway for the fast electron-hole pairs separation. Photocatalytic tests suggest that the loading of SnS_2 on 3DOM-$SrTiO_3$ alters the photo-reduced product from CO for 3DOM-$SrTiO_3$ to CH_4 for SnS_2/3DOM-$SrTiO_3$. The formed Z-scheme heterostructure promotes the photoelectrons on the CB of SnS_2 combining with the holes from VB of $SrTiO_3$ under light illumination, thus endowing more photoelectrons on the CB of $SrTiO_3$ to take part in CO_2 reduction. Finally, the SnS_2/3DOM-$SrTiO_3$ photocatalyst presents an increased activity and selectivity for light driven CH_4 generation (**Fig. 4c, d**). In addition to construct heterostructure, noble metal nanoparticles loading on 3DOM photocatalysts is considered as an effective method for promoting photocatalytic CO_2 reduction due to their inherent SPR (surface plasmon resonance) effect for increasing visible light harvesting and low Fermi level for trapping photoelectrons. Specifically, SPR is a indication of the resonance effect because of the interaction of conduction electrons of noble metal nanoparticles with illuminated photons, which can broaden visible light response range for the enhanced photocatalytic performance. A series of Au nanoparticles decorated 3DOM TiO_2 with different Au amounts were prepared for efficient CO_2 photoreduction (**Fig. 4e**).**[63]** TEM pictures indicate that the Au nanoparticles are

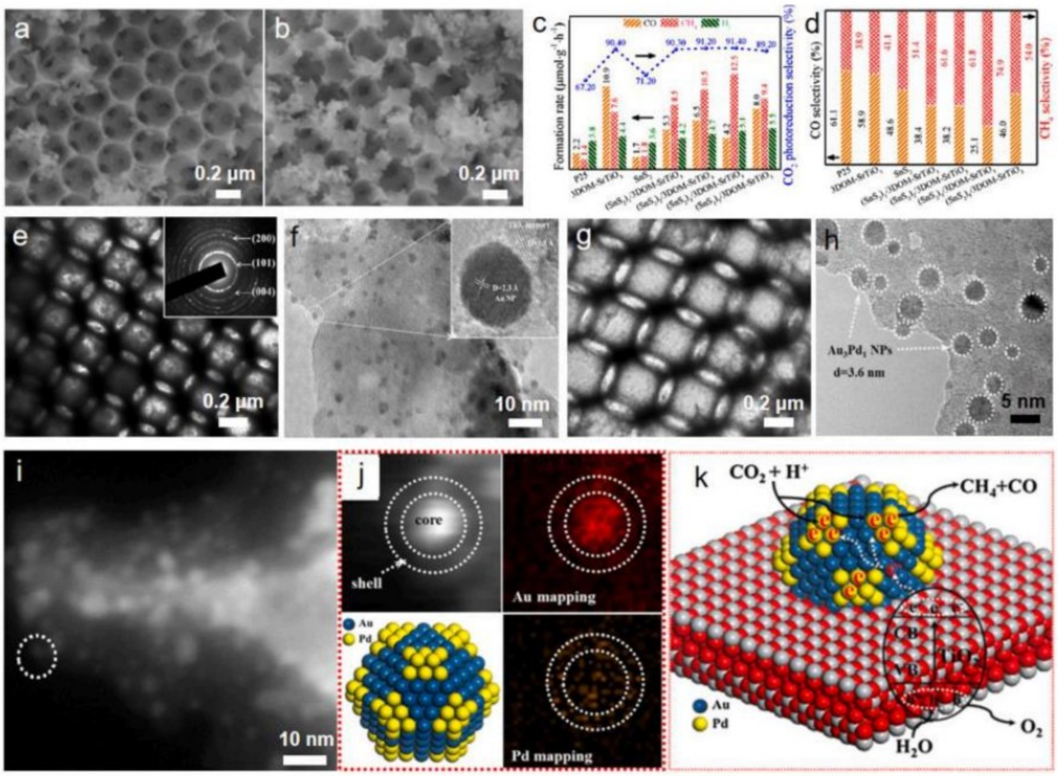

Fig. 4. SEM pictures of the as-synthesized (a) 3DOM-$SrTiO_3$ and (b) SnS_2/3DOM-$SrTiO_3$, (c) CO, CH_4 and H_2 productivity by CO_2 reduction and (d) photoreduction CO and CH_4 selectivity. Reproduced with permission.[62] Copyright 2020, Elsevier. (e) TEM and (f) HR-TEM pictures of the as-prepared Au decorated 3DOM TiO_2.[63] (g) TEM, (h) HR-TEM, (i) HAADF-STEM and (j) EDS elemental mapping pictures of the as-prepared AuPd nanoparticles loaded 3DOM TiO_2 photocatalyst; (k) schematic route of photocatalytic CO_2 reduction and photoelectrons migration mechanism on the AuPd/3DOM TiO_2 photocatalyst.[64]

homogeneously decorated on the inner walls of 3DOM TiO_2 (**Fig. 4f**). Both slow photo phenomenon of the 3DOM structure and the SPR effect of Au nanoparticles are profitable for light harvesting. Moreover, the conductive Au nanoparticles prohibit the recombination of photoexcited charge pairs therefore offering more photoelectrons for light driven CO_2 reduction. Finally, the 3DOM Au/TiO_2 photocatalyst brings out the efficient CH_4 productivity about 2.89 μmol g^{-1} h^{-1}, being around 2 and 3 folds greater than that of P25 and 3DOM TiO_2 photocatalysts, respectively. In addition to monometallic NPs loading, bimetallic nanoparticles deposited 3DOM materials for efficient photoreduction of CO_2 have been also reported. Typically, the core-shell configurated AuPd particles loaded 3DOM TiO_2 samples were obtained via a gas bubbling-helped reduction route (**Fig. 4g**).[64] As displayed in Fig. 3h, AuPd nanoparticles are uniformly loaded on the 3DOM-TiO_2. HAADF-STEM and EDS elemental mapping characterizations demonstrate a clear core-shell structure where Au is plentiful in the core whereas Pd component is mainly located in the shell (**Fig. 4i, j**). The AuPd with unique structure significantly facilitates the photoelectrons trapping for the subsequent photoredox reaction. Moreover, the 3DOM structure endowing the slow photon effect enhances visible light utilization and the loaded AuPd nanoparticles further improve visible light response owing to their SPR effect, which are profitable for efficient photoexcited CO_2 reduction. In fact, bimetallic AuPd nanoparticles possessing low Fermi level exert huge capacity to trap photoinduced electrons, thus promoting the photoelectrons migration from TiO_2 to AuPd nanoparticles to participate in CO_2 reduction (**Fig. 4k**). Photocatalytic CO_2 reduction experiments illustrate that the CH_4 production ability decreases and the CO generation increases with reducing the ratios of Au/Pd, therefore demonstrating that the high amount of Pd prohibits the conversion CO_2 into CH_4 and preferably promotes the conversion of CO_2 into CO. A series of 3DOM photocatalysts like TiO_2 and $SrTiO_3$ have been prepared for efficient light driven CO_2 conversion. The main products of CO and CH_4 are formed. Thus, the further modification on 3DOM photocatalysts should be carried out to promote the production of more valued products such as methanol and ethanol.**[65-68]**

1.2.1.4. Organics photoreforming

Visible light driven organics photoreforming presents a great potential for preparing value-added organics by biomass conversion.**[69–73]** However, the poor photoreforming selectivity and the detrimental reaction condition like strong alkalinity or toxic solvent are unfavorable for the large-scale production. In this context, Zhao et al. synthesized the gold nanoparticles loaded 3DOM TiO_2 (Au-3DOM TiO_2) photocatalyst for green, efficient and highly selective glucose photoreforming reaction.**[74]** The prepared Au-3DOM TiO_2 photocatalyst gives rise to the enhanced interaction between reactants and photocatalyst, sufficient surface active sites, fast photogenerated carriers separation and increased light harvesting because of the surface plasmon resonance of Au. The loading Au nanoparticles obviously improve the selectivity of photoreforming glucose into arabinose, meanwhile the value added organics like hydrogen and methane are also produced form the dehydration and hydrogenation reactions. Compared with 3DOM TiO_2 and Au loaded bulk TiO_2, the Au-3DOM TiO_2 displays about 8 and 2 times higher arabinose generation rate, respectively, implying that both the 3DOM architecture and Au loading are beneficial for the glucose photoreforming reaction. Soon after, they further fabricated 3DOM TiO_2-Au-CdS hybrid photocatalyst for light driven cellulose β-1,4-glycosidic cleavage.[75] The as-fabricated ternary photocatalyst shows an efficient Z-scheme photoelectrons transfer mechanism. Moreover, the 3DOM structure ensures the fast mass diffusion and light harvesting efficiency. As a result, the prepared 3DOM photocatalyst gives rise to the O substitution at C1 site followed with the shearing reaction, thus cleaving the β-1,4-glycosidic bond and leads to the evolution of gluconic acid and glucose.

1.2.1.5. H_2O_2 production

Solar light driven H_2O_2 generation has appealed a great attention because of its facile, safe, green and sustainable process.[76–83] Generally, H_2O_2 can be obtained by the photoredox reaction with H_2O and O_2 as raw materials under light illumination at room temperature. H_2O_2 is the only product without the formation of other toxic by-products. In order to improve the photocatalytic H_2O_2 generation, Zhang's team prepared the 3DOM C_3N_4 with surface carbon vacancies (3DOMCNCv) for efficient visible light driven H_2O_2 production.[84] As expected, the 3DOM-CNCv presents about 2.1 and 1.7 folds greater H_2O_2 productivity than that of the bulk C_3N_4 and bulk C_3N_4 with carbon vacancies, respectively. Thus the improved H_2O_2 evolution over 3DOM-CNCv is ascribed to the plentiful active sites, increased interaction between light and photocatalyst as well as convenient mass transmission channels owing to the 3DOM structure, as well as the rapid photoinduced carriers separation and enhanced visible light utilization due to the existence of carbon vacancies. This work brings out an efficient photocatalyst for H_2O_2 production by combining the merits of 3DOM structure and defect engineering. Shortly after, Ti_3C_2 quantum dots loaded 3DOM g-C_3N_4 with carbon defects by an electrostatic self-assembly process for photocatalytic H_2O_2 production.[85] Owing to the synergy between carbon vacancies, 3DOM structure and the formation of heterostructure, the fast photoinduced carriers separation and transfer is achieved (Fig. 5f). Finally, the further improved photocatalytic H_2O_2 evolution of 560.7 $\mu M\ h^{-1}$ is reached. In summary, a variety of photocatalytic reactions for sustainable energy formation involving H_2 production, CO_2 conversion, organics photoreforming and H_2O_2 production over 3DOM materials are well discussed. Apart from their obvious merits like large surface area and facile mass transfer channels, 3DOM materials deliver the intrinsic slow photon effects can also exert significant function for promoting photocatalytic reactions. Moreover, some specific active radicals like •O_2^- and •OH are favorable to be produced on 3DOM materials, thus further increasing the photocatalytic ability.

1.2.2. Electrocatalytic applications

So far, the loading of noble particles as co-catalysts has been frequently adopted to improve the performances of electrocatalysis reactions like oxygen evolution reaction (OER), oxygen reduction reaction (ORR) and hydrogen evolution reaction (HER).**[86-90]** However, their high cost and scarcity significantly limit the large-scale applications.**[91-97]** Hierarchically porous materials with obvious merits like plentiful surface active sites, facile mass diffusion channels and good electron transfer have gradually become a research hotspot in electrocatalytic fields.**[98-105]**.

1.2.2.1. Hydrogen evolution reaction

As an important process for electrochemical water decomposition process, the electrocatalytic hydrogen evolution needs highly efficient, stable and cost-effective electrocatalysts to realize desirable HER performance. Noble metals like Pt are frequently used in commercially electrocatalytic hydrogen evolution reaction due to their high efficiency. However, the several drawbacks are still existed for the Pt catalyst like highly expensive, rare storage in the earth and pollution issue during its generation. Up to now, lots of inexpensive materials have been explored as electrocatalysts for highly efficient HER. For instance, phosphides, sulfides, vanadates and molybdate are promising candidates, because their unique d-orbital electron vacancies can effectively promote the H_2O decomposition.**[90]** However, these materials often endow poor conductivity and limited surface active sites, thus restricting the further improved electrocatalytic activity. 3DOM materials possess several obvious advantages such as plentiful surface active sites, convenient mass diffusion channels and fast electron transfer kinetics, which can certainly accelerate the whole hydrogen evolution reaction process. Therefore, the fabrication of 3DOM structured electrocatalysts for efficient HER is becoming a research hotspot. Iron phosphide has appealed lots of attention in electrocatalytic hydrogen generation owing to its inexpensive cost, earth abundance and good electrochemical properties.[91,92] However, its electrocatalytic hydrogen generation activity is still far from the theoretical value due to its unsatisfactory conductivity, limited surface active sites and slow reactants and carriers transfer rates. Hence, constructing iron phosphide with a 3DOM structure is expected to an ideal method to fulfill the efficient electrocatalytic hydrogen generation. In this regard, Li's team prepared the 3DOM iron phosphide on carbon cloth (3DOM-FeP/CC) via an electrostatic self-assembly route followed with calcination and phosphorization (**Fig. 5a**).[92] The 3DOM-FeOx/CC sample obtained from template elimination displays the uniform macroporous structure with the size from 100 to 300 nm. After the phosphorization treatment, the structure of 3DOM-FeP/CC is maintained. The obtained 3DOM-FeP/CC delivers several distinct advantages such as the interpenetrated ordered macropores, plentiful channels, high surface area and good conductivity, thus being profitable for the fast reactant migration, abundant accessible active sites and outstanding carriers separation. As shown in **Fig 5b**, the fabricated 3DOM-FeP/CC electrocatalyst brings out a highly efficient electrocatalytic hydrogen evolution performance in acid medium, giving rise to an enhanced current density of 10 mA cm^{-2} under a small overpotential of 68 mV compared with that of FeP/CC and 3DOM FeP electrocatalysts. Ni-based metals display promising alternatives to Pt for the HER in alkaline medium due to their good activity and stability. In order to achieve higher HER activity, Sun et al. reported the fabrication of 3D ordered macro/mesoporous (3DOM/m) Ni via a chemical reduction deposition route.[93] The obtained 3DOM/m Ni displays the order macropores with size about 330 nm and the abundant mesopores with size around 4 nm exist in the macroporous walls, giving rise to the hierarchically ordered macro/mesoporous structure of the 3DOM/m Ni. Accordingly, the obtained 3DOM/m Ni possessing abundant mesopores with 3D interconnected ordered macropores can provide rich surface active sites because of its high surface area, convenient mass diffusion, and good conductivity thanks to the accelerated electron transfer and facilitated ion diffusion, thus endowing the 3DOM/m Ni a huge potential for highly efficient HER. As expected, the 3DOM/m Ni electrocatalyst displays the improved HER activity than that of 3DOM Ni without mesopores and Ni nanoparticles. A small onset overpotential of 63 mV and an excellent HER stability in alkaline electrolyte are realized on the 3DOM/m Ni, being comparable with the commercial Pt/C electrocatalyst. Xia's team prepared Cu3N decorated 3DOM titanium oxynitride (Cu3N@3DOM-TiOxNy) by a template method followed by an ammonia annealing treatment.[94] The 3DOM structure can offer the interconnected pores and channels for rapid mass transportation and a large surface area for abundant surface active sites. The loaded Cu3N as active sites can give rise to the reduced reaction activation barriers and thus result in a fast hydrogen gas release process. Meanwhile, the prepared catalyst also presents the stable and efficient HER ability in acidic, neutral and alkaline electrolytes. Moreover, both the TiOxN and the surface carbon residues endow outstanding conductivity and further improve its electrocatalytic activity. As expected, the prepared Cu3N@3DOM-TiOxNy nanocomposite presents highly efficient HER performance with a small over-potential from 71 to 79 mV. Moreover, the small Tafel slope of the Cu3N@3DOM-TiOxNy indicates the accelerated charges migration rate during the reaction procedure. The excellent HER ability is ascribed to the synergy of the 3DOM structure and TiOxNy loading. In this part, a series of 3DOM structured electrocatalysts are developed for the improved HER owing to their efficient electrons and mass transfer as well as sufficient surface active sites. Moreover, the loading of active species like Cu3N can further improve the HER activity.

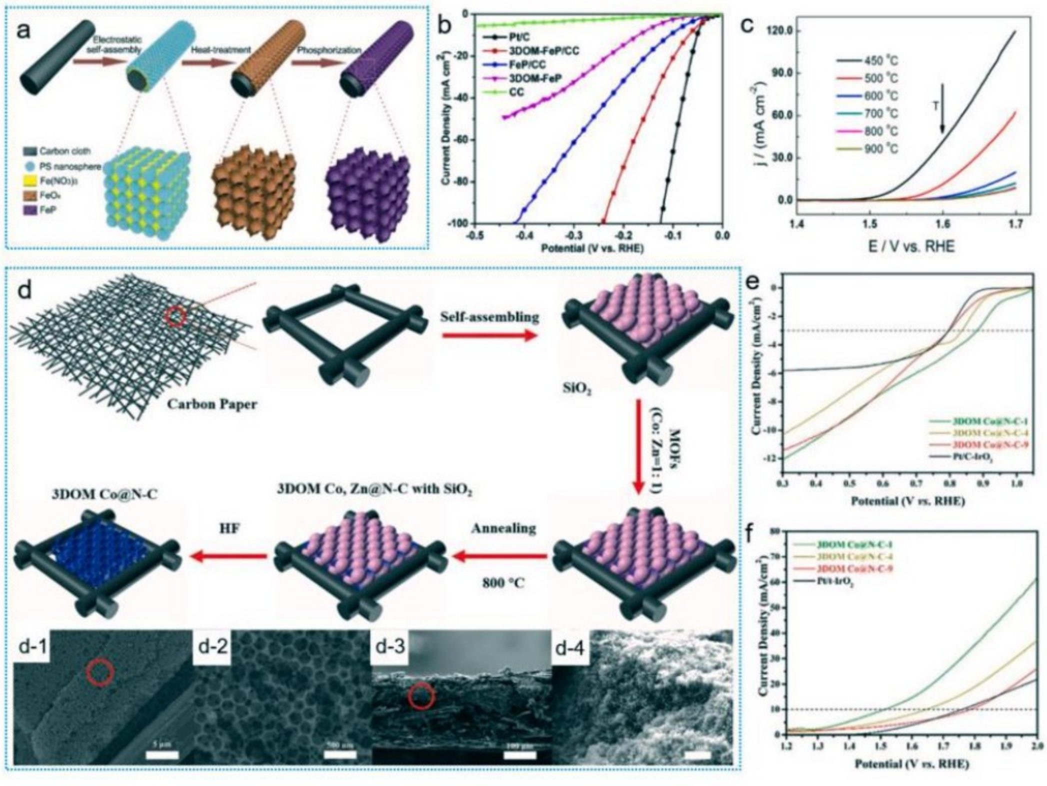

Fig. 5. (a) Schematic process for the fabrication of 3DOM-FeP/CC catalyst. (b) HER performance over the prepared catalysts.**[92]** (c) OER performances over the prepared catalysts with different treatment temperatures. Reproduced with permission.**[97]** (d) Schematic

illustration for the synthesis of 3DOM Co@N-C catalyst and the corresponding SEM pictures (d-1-d-4), (e) ORR and (f) OER performances over the synthesized catalysts.**[102]**

1.2.2.2. Oxygen evolution reaction

Compared with the well-studied HER, exploiting efficient and robust catalysts towards OER via an anodic reaction in water electrolysis is relatively difficult. Generally, the electrocatalysts in anode are easily to be oxidized and decomposited, thus leading to unsatisfactory OER performance.[96,97] For example, Pt is widely used as an ideal catalyst for HER in acidic medium, however its electrocatalytic performance for OER is relatively low because of the generation of a poorly conductive oxide film at potentials of water electrolysis anodes. Among all the inorganic materials, the optimal electrocatalysts for OER are IrO_2 and RuO_2 or their alloys owing to their good conductivity and chemical stability.[97] Up to now, various methods such as morphology modulation and other transition metals oxides combination have been exploited to obtain the further improved OER activity. Typically, 3DOM IrO_2 prepared via a silica colloidal crystal template strategy was reported by Chen's team.[96] In brief, $H_2IrCl_6 \, . \, 6H_2O$ solution as precursor was immersed into the cavities SiO_2 templates and followed by the calcination in air at 450℃ to acquire the IrO_2/TiO_2 composite. Finally, HF was used to treat the composite after calcination to eliminate the SiO_2 templates and the 3DOM IrO_2 was prepared. SEM images show that the 3DOM IrO_2 endows highly ordered macropores with size about 300 nm. Meanwhile, abundant mesopores are also produced on the walls of macropores. The unique 3DOM structure provides huge surface area for abundant reaction active sites and convenient mass diffusion channels, being favorable for the superior OER activity. Accordingly, about 2.5 times enhancement in OER activity is achieved by using 3DOM IrO_2 as the electrode materials compared with that of IrO_2 prepared by conventional colloidal strategy, showing the prospect of 3DOM materials in reducing the demand of the expensive electrocatalysts for OER in water electrolysis. Soon after, their team further investigated the effect of the condescending temperature on the pore size and the electrocatalytic property of 3DOM IrO_2 material.[97] A template-precursor (H_2IrCl_6/TiO_2) composite was treated at various temperatures from 350 to 900°C. A series of characterizations suggest that the IrO_2 sample obtained at 450°C exhibits the honeycomb array of macropores with cross-linking mesopores on the pore walls. When the temperature over 450°C, the IrO_2 sample shows the formation of crystallite size on the walls of macropores and thus leads to the reduction of surface area. The 3DOM structure of IrO_2 will be restricted to generation as calcination temperature exceeds 700°C due to the higher temperature for SiO_2 template phase-transition. Among the as-prepared samples, the 3DOM IrO_2 obtained at 450°C presents the best OER performance owing to its optimal structure merits (**Fig. 5c**). This work clearly reveals that the effective OER performance of the 3DOM IrO_2 depends on large surfaces and larger pore volume as well as facile mass transfer channels. Compared with a great numbers of materials for HER, the electrocatalysts for efficient OER are mainly IrO_2 and RuO_2 based materials. Therefore, more advanced electrocatalysts for OER should be exploited in the future.

1.2.2.3. Oxygen reduction reaction

In general, ORR is often associated with metal-air batteries.[99] For example, the charge-discharge performance of the Zinc-air batteries mainly depends on both the ORR and OER.[100] However, Zinc-air batteries suffer from the poor electrocatalysis activity on their air cathode and thus lead to the unsatisfactory energy storage performance. Carbon based materials such as graphene and porous carbon combining with transition metals to generate transition metal@carbon hybrids have been exploited as a promising method to give rise to the excellent ORR and OER performances as well as good chemical stability.[101] Moreover, in order to expose more active reaction sites on the surface of electrocatalysts, various porous structures and morphologies are therefore designed. 3DOM structure possessing abundantly interconnected pores and large surface area is seemed as an ideal candidate to increase the zinc-air batteries performance. On accounting of the above facts, Hu et al. fabricated a thick film air electrode composed of adequately uncovered CoNx and Co nanoparticles and 3DOM carbon material.[102] As depicted in **Fig 5d**, a piece of carbon paper was firstly loaded into SiO_2 nanospheres ethanol solution and the self-assembling of SiO_2 nanospheres was occurred. Secondly, the MOFs precursor solution including Co^{2+}, $Zn^{2+,}$ and 2-Melm species was used to immerse the cavities of SiO_2 nanospheres array. Next the composite of MOFs with SiO_2 nanospheres array was carbonized to acquire Co@N-C. Finally, the 3DOM Co@N-C catalyst was obtained by removing SiO_2 template by HF. The as-synthesized 3DOM Co@N-C catalyst displays uniformly interconnected macropores with size about 250 nm. The unique 3DOM nitrogen-doped carbon structure gives rise to high specific surface area for abundant exposing active sites and the interconnected channels are profitable for mass diffusion and transfer.

More importantly, Co particles and CoNx species loaded on 3DOM carbon material as active sites can effectively improve the reaction rates of ORR and OER (**Fig. 5e, f**). The intrinsically good conductivity of carbon matrix also favors charge transfer. Based on the aforementioned results, a rechargeable zinc-air battery involving 3DOM Co@N-C as the cathode brings out large power density, large specific energy density and excellent long-term cycling stability. Qiao's group prepared a series of 3DOM g-C_3N_4/C electrocatalysts for improving ORR activity. Silica spheres with different sizes as templates were firstly prepared.[103] The carbon shell was coated via the carbonization of sucrose infiltration. Melted cyanamide was then immersed into the voids of C@SiO_2, subsequent by calcinating in N_2 to generate g-C_3N_4/C@SiO_2. The silica template was finally eliminated with HF solution (**Fig. 6a**). By tuning the size of silica spheres, a variety of g-C_3N_4/C@SiO_2 with different macropores sizes are obtained (**Fig. 6b-d**). Accordingly, the synthesized g-C_3N_4/C@SiO_2 with macropores size of 150 nm displays the comparable ORR catalytic performance with commercial Pt/C. More importantly, the 3DOM g-C_3N_4/C electrocatalyst endows the long-term stability in alkaline solution. The outstanding ORR performance of 3DOM g-C_3N_4/C can be ascribed to the synergy between the accelerated mass diffusion and the sufficient amounts of active sites due to the large specific surface area. In summary, carbon based materials have predominantly been explored for efficient ORR. By loading a variety of active species like Co and g-C_3N_4 on 3DOM C, the fast charges transfer is achieved and the ORR ability can be further improved.

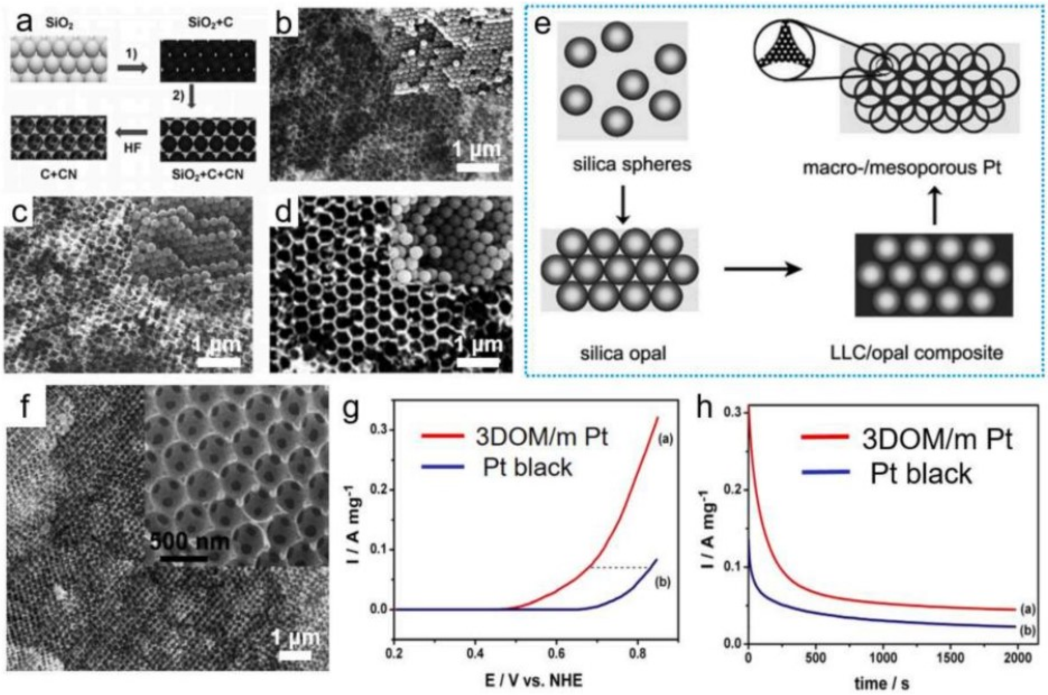

Fig. 6. (a) Schematic process for the fabrication of 3DOM g-C3N4/C electrocatalyst and (c-d) the prepared electrocatalyst with different sizes.[103] (e) Schematic preparation route for 3DOM Pt electrocatalyst, (f) SEM picture, (g) LSV of methanol oxidation reaction and (h) stability test for the 3DOM/m Pt and Pt black.[105]

1.2.2.4. Methanol oxidation reaction

In addition to the above discussed HER, OER and ORR, the improved methanol oxidation reaction can also be achieved on 3DOM materials. Typically, 3DOM Pt electrocatalyst was fabricated via a dual-templating method using silica opal and nonionic surfactant Brij 56 LLC as the macropore and mesopore templates, respectively (**Fig. 6e**).[105] The obtained 3DOM Pt displays an uniform macroporous structure with size about 290 nm (**Fig. 6f**). In addition, the abundant mesopores consisted of polycrystalline Pt nanoparticles are observed on the macroporous walls of the 3DOM Pt. Thus, the 3DOM Pt electrocatalyst gives rise to large active surface area and convenient mass diffusion and transfer channels. As presented in **Fig 6g**, the onset potential of 0.27 V for the 3DOM Pt is more negative than that of 0.44 V for the commercial Pt black catalyst, demonstrating the superior methanol oxidation reaction activity for 3DOM Pt. Moreover, the higher electrocatalytic stability performance for 3DOM/m Pt in the methanol oxidation than that of Pt black is achieved (**Fig. 6h**). 3DOM structured noble metals have been mainly developed electrocatalytic methanol oxidation. Although the efficient methanol oxidation activity is achieved, the high cost of noble metals limits their large-scale applications. Thus, exploring cheap electrocatalysts for efficient methanol oxidation are urgently required.

1.3 The aim and major research results

In the past few decades, a great number of photocatalysts including metal oxides, metal sulfides, nitride materials, bismuth materials, and perovskite structured materials have been explored. Nevertheless, these photocatalysts generally show unsatisfactory photocatalytic ability much below the expectation due to their limited light utilization, considerable electron-hole pair recombination, and inactive surface redox processes. Hence, different modification strategies have been explored for enhancing the photocatalytic ability. For example, the combination of semiconductors with other components by ion doping, heterostructure fabrication, and noble metal loading have been exploited to facilitate photocatalytic reactions. In addition, morphology/size modulation, defect engineering, and tuning of active crystal facets are also considered as reliable modification methods to achieve high photocatalytic rates. Among the various modification strategies, morphology/size modulation has attracted increasing attention due to the fact that it is a facile method, enables precise control, and has high efficiency. However, the photocatalytic potential of the semiconductors can still not be fully explored. Therefore, the hierarchically porous materials engineering with simultaneous doping, defecting or heterostructuring strategies have been often adopted for acquiring further improved photocatalytic activity. In the thesis, three kinds of hierarchically porous semiconductor materials with enhanced photocatalytic performance are reported.

1. The first work reports the fabrication of a hydrophilic bi-functional hierarchical architecture by the assembly of B-doped g-C_3N_4 nanoplatelets. The obtained hierarchically porous B-doped g-C_3N_4 material gives rise to full utilization of their highly enhanced visible light harvesting and photoinduced charges separation in aqueous medium, leading to an excellent photocatalytic H_2O_2 production rate and photoelectrochemical water splitting performance.

2. The second work reports the visible-light H_2O_2 artificial photosynthesis by digging pro-superoxide radical carbon vacancies in three-dimensional hierarchical porous g-C_3N_4 through a simple hydrolysis-freeze-drying-thermal treatment. A significant electronic structure change is revealed upon the implantation of carbon vacancies, broadening visible-light absorption and facilitating the photogenerated charge separation. The strong electron affinity of the carbon vacancies promotes superoxide radical formation, significantly boosting the H_2O_2 photocatalytic production

3. Finally, ternary 3D ordered macroporous (3DOM) heterojunction nanocomposites (platinum/bismuth molybdate/3DOM TiO_2: 3DOM-Pt/Bi_2MoO_6/TiO_2) are designed and synthesized as multifunctional platform for photocatalytic dye degradation, photoelectrocatalytic (PEC) water splitting, and thermal-catalytic toluene decomposition with high performance. A series of structural, optical, and electronic characterizations demonstrates that the remarkably improved photocatalytic degradation and PEC water splitting activities are attributed to the combined effects of enhanced light harvesting, abundant reactive sites, facile reactants transfer, and efficient charges-holes pair separation.

Reference

1. Wang. T., Yan. X., Zhao. S., Lin. B., Xue. C., Yang. G., Ding. S., Yang. B., Ma. C., Yang. G., Yang. G. A facile one-step synthesis of three-dimensionally ordered macroporous N-doped TiO_2 with ethanediamine as the nitrogen source. J. Mater. Chem. A **2**, 15611-15619 (2014).

2. Béjar. J., Espinosa-Magaña. F., Guerra-Balcázar. M., Ledesma-García. J., Álvarez-Contreras. L., Arjona. N., Arriaga. L. Three-Dimensional-Order Macroporous AB_2O_4 Spinels (A, B= Co and Mn) as Electrodes in Zn-Air Batteries. ACS Appl. Mater. Interfaces **12**, 53760-53773 (2020).

3. Yan. X., Ye. K., Zhang. T., Xue. C., Zhang. D., Ma. C., Wei. J., Yang. G. Formation of three-dimensionally ordered macroporous TiO_2@nanosheet SnS_2 heterojunctions for exceptional visible-light driven photocatalytic activity. New J Chem. **41**, 8482-8489 (2017).

4. Liu. J., Zhao. H., Wu. M., Van der Schueren. B., Li. Y., Deparis. O., Su. B-L. Slow photons for photocatalysis and photovoltaics. Adv Mater. **29**, 1605349 (2017).

5. Ding. Y., Maitra. S., Wang. C., Halder. S., Zheng. R., Barakat. T., Soy. S., Chen. L-H., Su. B-L. Vacancy defect engineering in semiconductors for solar light-driven environmental remediation and sustainable energy production. Interdiscip. Mater. **1**, 213-255 (2022).

6. Zheng. H., Shah. S., Abbas. M., Ly. I., Rivera. T., Almeida. R., Ravaine. S. Efficiency enhancement in solid state dye sensitized solar cells by including inverse opals with controlled layer thicknesses. Photonics Nanostruct. **21**, 13-18 (2016).

7. Yu. S., Liu. G., Zheng. J., Wang. Y., Ling. Y., Zhang. Y., Yu. Z., Sun. S., Fu. Y., Chen. D., Cai. W., Cui. J., Wang. G., Zhou. H. Excellent Thermostable and Mechanically Reinforced Lithium-Ion Capacitor Based on Inverse Opal Structural PVDF-HFP/MWCNT Electrolyte. ACS Appl. Energy Mater. **5**, 3876-3885 (2022).

8. Ding. Y., Maitra. S., Esteban. D., Bals. S., Vrielinck. H., Barakat. T., Roy. S., Tendeloo. G., Liu. J., Li. Y., Vlad. A., Su. B-L. Photochemical production of hydrogen peroxide by digging pro-superoxide radical carbon vacancies in porous carbon nitride. Cell Reports Phys. Sci. **3**, 100874 (2022).

9. Long. J., Fu. M., Li. C., Sun. C., He. D., Wang. Y. High-quality ZnO inverse opals and related heterostructures as photocatalysts produced by atomic layer deposition. Appl. Surf. Sci. **454**, 112-120 (2018).

10. Zhou. S., Tang. R., Li. H., Fu. L., Li. B., Yin. L. Fluorescence resonance energy transfer effect enhanced high performance of Si quantum Dots/$CsPbBr_3$ inverse opal heterostructure perovskite solar cells. J. Power Sources **439**, 227065 (2019).

11. Wen. F., Liu. W. Three-dimensional ordered macroporous materials for photocatalysis: design and applications. J. Mater. Chem. A **9**, 18129–18147 (2021).

12. Stein. A., Wilson. B.E., Rudisill. S.G. Design and functionality of colloidal-crystal-templated materials-chemical applications of inverse opals. Chem. Soc. Rev. **42**, 2763–2803 (2013).

13. Liu. Y.Z., Guo. R.T., Duan. C.P., Wu. G.L., Miao. Y.F., Gu. J.W., Pan. W.G. Removal of gaseous pollutants by using 3DOM-based catalysts: A review. Chemosphere **262**, 127886 (2021).

14.Feng. J., Zheng. D., Gao. X., Que. W., Shi. W., Liu. W., Wu. F., Cao. X. Three-dimensional ordered porous carbon for energy conversion and storage applications. Front. Energy Res. **8**, 210 (2020).

15. Liu. Z., Yuan. X., Zhang. S., Wang. J., Huang. Q., Yu. N., Zhu. Y., Fu. L., Wang. F., Chen. Y., Wu. Y. Three-dimensional ordered porous electrode materials for electrochemical energy storage. NPG Asia Mater. **11**, 1–21 (2019).

16. Zhang. C., Zhao. P., Liu. S., Yu. K. Three-dimensionally ordered macroporous perovskite materials for environmental applications. Chinese J. Catal. **40**, 1324–1338 (2019).

17. Maho. A., Lobet. M., Daem. N., Piron. P., Spronck. G., Loicq. J., Cloots. R., Colson. P., Henrist. C., Dewalque. J. Photonic Structuration of Hybrid Inverse-Opal TiO_2-Perovskite Layers for Enhanced Light Absorption in Solar Cells. ACS Appl. Energy Mater. **4**, 1108-1119 (2021) .

18. Ghosh. D., Roy. K., Maitra. S., Kumar. P. Unravelling Rashba-Dresselhaus Splitting Assisted Magneto-Photoelectrochemical Water Splitting in Asymmetric MoSSe-GaN Heterostructures. J. Phys. Chem. Lett. **13**, 1234-1240 (2022).

19. Maitra. S., Pal. S., Maitra. T., Halder. S., Roy. S. Solvothermal Etching-Assisted Phase and Morphology Tailoring in Highly Porous $CuFe_2O_4$ Nanoflake Photocathodes for Solar Water Splitting. Energy Fuels **35**, 14087-14100 (2021).

20. Ding. Y., Maitra. S., Wang. C., Zheng. R., Zhang. M., Barakat. T., Soy. S., Liu. J., Li. Y., Su. B-L. Hydrophilic bi-functional B-doped g-C_3N_4 hierarchical architecture for excellent photocatalytic H_2O_2 production and photoelectrochemical water splitting. J. Energy Chem. **70**, 236-247 (2022).

21. D. Kang, S. Kim, Y. Chae, J. Lee, J.H. Moon, Particulate inverse opal carbon electrodes for lithium-ion batteries, Langmuir 29 (2013), 1192-1198.

22. W.B. Yu, W.D. Dong, C.F. Li, N. Macadam, J.X. Yang, G.B. Zhang, Z-Y. Hu, T-C. Wu, Y. Li, T. Hasan, L-H. Chen, L-Q. Mai, B-L. Su, Interwoven scaffolded porous titanium oxide nanocubes/carbon nanotubes framework for high-performance sodium-ion battery. J. Energy Chem. 59 (2021) 38–46.

23. E. Armstrong, D. McNulty, H. Geaney, C. O'Dwyer, Electrodeposited structurally stable V_2O_5 inverse opal networks as high performance thin film lithium batteries, ACS Appl. Mater. Interfaces 7 (2015) 27006-27015.

24. H.S. Mohamed, C.F. Li, L. Wu, W.H. Shi, W.D. Dong, J. Liu, Z-Y. Hu, L-H. Chen, Y. Li, B-L. Su, Growing ordered CuO nanorods on 2D Cu/g-C_3N_4 nanosheets as stable freestanding anode for outstanding lithium storage. Chem. Eng. J. 407 (2021) 126941.

25. W. D., Dong, W.B. Yu, F.J. Xia, L.D. Chen, Y.J. Zhang, H.G. Tan, L. Wu, Z-Y. Hu, H.S. Mohamed, J. Liu, Z. Deng, Y. Li, L-H. Chen, B-L. Su, Melamine-based polymer networks enabled N, O, S Co-doped defect-rich hierarchically porous carbon nanobelts for stable and long-cycle Li-ion and Li-Se batteries. J. Colloid Interface Sci. 582 (2021) 60–69.

26. K. Ji, H. Dai, J. Deng, H. Zang, H. Arandiyan, S. Xie, H. Yang, 3DOM $BiVO_4$ supported silver bromide and noble metals: High-performance photocatalysts for the visible-light-driven degradation of 4-chlorophenol, Appl. Catal. B 168 (2015) 274–282.

27. M. Sadakane, T. Asanuma, J. Kubo, W. Ueda, Facile procedure to prepare three-dimensionally ordered macroporous (3DOM) perovskite-type mixed metal oxides by colloidal crystal templating method, Chem. Mater. 17 (2005) 3546–3551.

28. W.D. Lu, X.Q. Gao, Q.G. Wang, W.C. Li, Z.C. Zhao, D.Q. Wang, A.H. Lu, Ordered macroporous boron phosphate crystals as metal-free catalysts for the oxidative dehydrogenation of propane, Chinese J. Catal. 41 (2020) 1837–1845.

29. J. Bi, S. Zhao, J. Wu, Y. Xu, Z. Wang, Y. Han, X. Zhang, Dual cocatalysts decorated three dimensionally ordered mesoporous g-C_3N_4 with homogeneous wall thickness for enhanced photocatalytic performance, Appl. Organomet. Chem. 34 (2020), e5552.

30. R. Cao, H. Yang, X. Deng, P. Sun, S. Zhang, X. Xu, Construction of 3DOM Carbon Nitrides with Quasi-Honeycomb Structures for Efficient Photocatalytic H_2 Production. ChemCatChem 10 (2018) 5656–64.

31. L. Jiang, H. Gao, R. Cao, S. Zhang, J. Li, Construction of Novel Three Dimensionally Macroporous g-C_3N_4 for Efficient Adsorption/Photocatalytic Reduction of U (VI), J. Inorg. Mater. 35 (2020) 359.

32. W. Li, Q. Ma, X. Wang, X.S. Chu, F. Wang, X.C. Wang, C.Y. Wang, Enhanced photoresponse and fast charge transfer: three-dimensional macroporous g-C_3N_4/GO-TiO_2 nanostructure for hydrogen evolution, J. Mater. Chem. A 8 (2020) 19533–19543.

33. X. Gao, L. Li, M. An, T. Zheng, F. Ma, ZnO QDs and three-dimensional ordered macroporous structure synergistically enhance the photocatalytic degradation and hydrogen evolution performance of WO_3/TiO_2 composites. J. Phys. Chem. Solids 165, (2022). 110655.

34. X. Wang, Q. Li, Q. Lin, R. Zhang, M. Ding, CdS-sensitized 3D ordered macroporous g-C_3N_4 for enhanced visible-light photocatalytic hydrogen generation, J. Mater. Sci. Technol. 111 (2022) 204-210.

35. J. Liu, Y.H. Guo, Z.Y. Hu, H. Zhao, Z.C. Yu, L. Chen, Y. Li, G.V. Tendeloo, B-L. Su, Slow Photon Enhanced Heterojunction Accelerates Photocatalytic Hydrogen Evolution Reaction to Unprecedented Rates, CCS Chem. (2022) 1-28.

36. M. Zalfani, B. Van, Z.Y. Hu, J.C. Rooke, R. Bourguiga, M. Wu, Y. Li, G.V. Tendeloo, B-L. Su, Novel 3DOM $BiVO_4/TiO_2$ nanocomposites for highly enhanced photocatalytic activity, J. Mater. Chem. A 3 (2015) 21244-21256.

37. M., Zalfani, B. Van, M. Mahdouani, R. Bourguiga, W.B. Yu, M. Wu, O. Deparis, Y. Li, B-L. Su, ZnO quantum dots decorated 3DOM TiO_2 nanocomposites: Symbiose of quantum size effects and photonic structure for highly enhanced photocatalytic degradation of organic pollutants, Appl. Catal. B 199 (2016) 187-198.

38. H. Zhao, M. Zalfani, C.F. Li, J. Liu, Z.Y. Hu, M. Mahdouani, Y. Li, B-L. Su, Cascade electronic band structured zinc oxide/bismuth vanadate/three-dimensional ordered macroporous titanium dioxide ternary nanocomposites for enhanced visible light photocatalysis, J. Colloid Interface Sci. 539 (2019)585-597.

39. Y. Ding, L. Huang, T. Barakat, B-L. Su, A Novel 3DOM TiO_2 based multifunctional photocatalytic and catalytic platform for energy regeneration and pollutants degradation, Adv. Mater. Interfaces 8 (2021) 2001879.

40. J.F. Li, C.Y. Zhong, J.R. Huang, Y. Chen, Z. Wang, Z.Q. Liu, Carbon dots decorated three-dimensionally ordered macroporous bismuth-doped titanium dioxide with efficient charge separation for high performance photocatalysis, J. Colloid Interface Sci. 553 (2019) 758-767.

41.B. Lin, G. Yang, B. Yang, Y. Zhao, Construction of novel three dimensionally ordered macroporous carbon nitride for highly efficient photocatalytic activity, Appl. Catal. B 198 (2016) 276-285.

42. Y. Tian, L. Li, Y. Hao, X. Song, F. Ma, L. Wang, CdS@ 3DOM TiO_2-ZrO_2 composites with high efficiency photocatalytic properties prepared by template method combined with in-situ self-assembly technology, Int. J. Hydrog. Energy 44 (2019) 27363-27378.

43. D. Qi, L. Lu, Z. Xi, L. Wang, J. Zhang, Enhanced photocatalytic performance of TiO_2 based on synergistic effect of Ti^{3+} self-doping and slow light effect, Appl. Catal. B 160 (2014) 621-628.

44. Y. Tian, L. Zhou, Q. Zhu, J. Lei, L. Wang, J. Zhang, Y. Liu, Hierarchical macro-mesoporous g-C_3N_4 with an inverse opal structure and vacancies for high-efficiency solar energy conversion and environmental remediation, Nanoscale 11 (2019) 20638-20647.

45. C. Zhang, K. Yu, Y. Feng, Y. Chang, T. Yang, Y. Xuan, S. Liu, Novel 3DOM-$SrTiO_3$/Ag/Ag_3PO_4 ternary Z-scheme photocatalysts with remarkably improved activity and durability for contaminant degradation, Appl. Catal. B 210 (2017) 77-87.

46. G.Q. Ma, F.S. Liu, S. Wang, Z.C. Dang, J.W. Zhang, X.J. Fu, M.S. Hou, Preparation and characterization of Bi_2S_3/3DOM-TiO_2 for efficient photocatalytic degradation of rhodamine B, Mater. Sci. Semicond Process 100 (2019) 61-72.

47. C. Lv, X. Lan, L. Wang, X. Dai, M. Zhang, J. Cui, S. Tuan, S. Wang, J. Shi, Rapidly and highly efficient degradation of tetracycline hydrochloride in wastewater by 3D IO-TiO_2-CdS nanocomposite under visible light, Environ. Technol. 42 (2021) 377-387.

48. J. Hou, X. Lan, J. Shi, L. Xin, L. Wang, The synergistic effect of fullerene and 3D ordered macroporous structure on promoting photocatalytic performance, J. Photochem. Photobiol. A 400 (2020) 112680.

49. Y. Hao, L. Li, D. Liu, H. Yu, Q. Zhou, The synergy of SPR effect and Z-scheme of Ag on enhanced photocatalytic performance of 3DOM Ag/CeO_2-ZrO_2 composite, Mol. Catal. 447 (2018) 37-46.

50. H. Zhao, M. Wu, J. Liu, Z. Deng, Y. Li, B-L. Su, Synergistic promotion of solar-driven H_2 generation by three-dimensionally ordered macroporous structured TiO_2-Au-CdS ternary photocatalyst, Appl. Catal. B 184 (2016) 182-190.

51. H. Zhao, Z. Hu, J. Liu, Y. Li, M. Wu, G.V. Tendeloo, B-L. Su, Blue-edge slow photons promoting visible-light hydrogen production on gradient ternary 3DOM TiO_2-Au-CdS photonic crystals, Nano Energy 47 (2018) 266-274.

52. H. Zhao, C.F. Li, Z.Y. Hu, J. Liu, Y. Li, J. Hu, G.V. Tendeloo, L-H. Chen, B-L. Su, Size effect of bifunctional gold in hierarchical titanium oxide-gold-cadmium sulfide with slow photon effect for unprecedented visible-light hydrogen production, J. Colloid Interface Sci. 604 (2021) 131-140.

53. W. Liu, G. Liu, N. Shi, D. Liu, F. Wen, Carbon quantum dot-modified and chloride-doped ordered macroporous graphitic carbon nitride composites for hydrogen evolution, ACS Appl. Nano Mater. 3 (2020) 12188-12197.

54. X. Yan, M. Xia, B. Xu, J. Wei, B. Yang, G. Yang, Fabrication of novel all-solid-state Z-scheme heterojunctions of 3DOM-WO_3/Pt coated by mono-or few-layered WS_2 for efficient photocatalytic decomposition performance in Vis-NIR region, Appl. Catal. B 232 (2018) 481-491.

55. Y. Chang, Y. Xuan, H. Quan, H. Zhang, S. Liu, Z. Li, K. Yu, J. Cao, Hydrogen treated Au/3DOM-TiO_2 with promoted photocatalytic efficiency for hydrogen evolution from water splitting, Chem. Eng. J. 382 (2020) 122869.

56. K. Yu, C. Zhang, Y. Chang, Y. Feng, Z. Yang, T. Yang, L-L. Lou, S. Liu, Novel three-dimensionally ordered macroporous SrTiO3 photocatalysts with remarkably enhanced hydrogen production performance, Appl. Catal. B 200 (2017) 514-520.

57. Y. Chang, K. Yu, C. Zhang, Z. Yang, Y. Feng, H. Hao, Y. Jiang, L-L. Lou, W. Zhou, S. Liu, Ternary CdS/Au/3DOM-$SrTiO_3$ composites with synergistic enhancement for hydrogen production from visible-light photocatalytic water splitting, Appl. Catal. B 215 (2017) 74-84.

58. W. Liu, S. Chang, D. Liu, F. Wen, Three-dimensional ordered macroporous materials with g-C_3N_4 and TiO_2 as pore walls for efficient photocatalytic hydrogen evolution, Colloids Surfaces A 609 (2021) 125681.

59. X. Yan, B. Xu, X. Yang, J. Wei, B. Yang, L. Zhao, G. Yang, Through hydrogen spillover to fabricate novel 3DOM-H_xWO_3/Pt/CdS Z-scheme heterojunctions for enhanced photocatalytic hydrogen evolution, Appl. Catal. B 256 (2019) 117812.

60. Y. Chang, Y. Xuan, C. Zhang, H. Hao, K. Yu, S. Liu, Z-Scheme Pt@CdS/3DOM-$SrTiO_3$ composite with enhanced photocatalytic hydrogen evolution from water splitting, Catal. Today 327 (2019) 315-322.

61. H. Zhao, J. Liu, ,C.F. Li, X. Zhang, Y. Li, Z.Y. Hu, B. Li, Z. Chen, J. Hu, B-L. Su, Meso-Microporous Nanosheet-Constructed 3DOM Perovskites for Remarkable Photocatalytic Hydrogen Production, Adv. Funct. Mater. (2022) 2112831.

62. W. He, X. Wu, Y. Li, J. Xiong, Z.Tang, Y. Wei, Z. Zhao, X. Zhang, J. Liu, Z-scheme heterojunction of SnS_2-decorated 3DOM-$SrTiO_3$ for selectively photocatalytic CO_2 reduction into CH_4, Chin. Chem. Lett. 31 (2020) 2774-2778.

63. J. Jiao, Y. Wei, Z. Zhao, W. Zhong, J. Liu, J. Li, A. Duan, G. Jiang, Synthesis of 3D ordered macroporous TiO_2-supported Au nanoparticle photocatalysts and their photocatalytic performances for the reduction of CO2 to methane, Catal. Today 258 (2015) 319-326.

64. J. Jiao, Y. Wei, Y. Zhao, Z. Zhao, A. Duan, J. Liu, Y. Pang, J. Li, G. Jiang, Y. Wang, AuPd/3DOM-TiO_2 catalysts for photocatalytic reduction of CO_2: High efficient separation of photogenerated charge carriers, Appl. Catal. B 209 (2017) 228-239.

65. Yan, Z., Li, K., Shao, D., Shen, Q., Ding, Y., Huang, S., Zheng, X. (2022). Visible-light-responsive reduced graphene oxide/gC_3N_4/TiO_2 composite nanocoating for photoelectric stimulation of neuronal and osteoblastic differentiation. RSC advances, 12(15), 8878-8888.

66. Sun, H. X., Wang, H. N., Fu, Y. M., Meng, X., He, Y. O., Yang, R. G., Su, Z. M. (2022). A multifunctional anionic metal-organic framework for high proton conductivity and photoreduction of CO_2 induced by cation exchange. Dalton Transactions, 51(12), 4798-4805.

67. Meng, Y., Xu, Z., Shen, Z., Xia, Q., Cao, Y., Wang, Y., & Li, X. (2022). Understanding the water molecule effect in metal-free B-based electrocatalysts for electrochemical CO_2 reduction. Journal of Materials Chemistry A, 10(12), 6508-6522.

68. Gong, E., Ali, S., Hiragond, C. B., Kim, H. S., Powar, N. S., Kim, D., In, S. I. (2022). Solar fuels: research and development strategies to accelerate photocatalytic CO_2 conversion into hydrocarbon fuels. Energy & Environmental Science.

69. H. Zhao, X. Yu, C.F. Li, W. Yu, A. Wang, Z.Y. Hu, S. Larter, Y. Li, M.G. Kibria, J. Hu, Carbon quantum dots modified TiO_2 composites for hydrogen production and selective glucose photoreforming, J. Energy Chem 64 (2022) 201–208.

70. U. Nwosu, H. Zhao, M. Kibria, J. Hu, Unlocking Selective Pathways for Glucose Photoreforming by Modulating Reaction Conditions, ACS Sustain. Chem. Eng. 10 (2022) 5867–5874.

71. J. Wang, P. Kumar, H. Zhao, M. Kibria, J. Hu, Polymeric carbon nitride-based photocatalysts for photoreforming of biomass derivatives, Green Chem 23 (2021) 7435–7457.

72. J. Wang, H. Zhao, B. Zhu, S. Larter, S. Cao, J. Yu, J. Hu, Solar-Driven Glucose Isomerization into Fructose via Transient Lewis Acid-Base Active Sites, ACS Catal 11 (2021) 12170–12178.

73. N. Uwosu, A. Wang, B. Palma, H. Zhao, M. Khan, M. Kibria, J. Hu, Selective biomass photoreforming for valuable chemicals and fuels: A critical review, Renew. Sust. Energ. Rev. 148 (2021), 111266.

74. H. Zhao, P. Liu, X. Wu, A. Wang, D. Zheng, S. Wang, Z. Chen, S. Larter, Y. Li, BL. Su, M.G. Kibria, J. Hu, Plasmon enhanced glucose photoreforming for arabinose and gas fuel co-production over 3DOM TiO_2-Au, Appl. Catal. B 291 (2021), 120055.

75. H. Zhao, C.F. Li, X. Yu, N. Zhong, Z.Y. Hu, Y. Li, S. Larter, M.G. Kibria, J. Hu, Mechanistic understanding of cellulose β-1, 4-glycosidic cleavage via photocatalysis, Appl. Catal. B 302 (2022), 120872.

76. Y. Sun, L. Han, P. Strasser, A comparative perspective of electrochemical and photochemical approaches for catalytic H_2O_2 production, Chem. Soc. Rev. 49 (2020) 6605–6631.

77. J. Liu, Y. Zou, B. Jin, K. Zhang, J.H. Park, Hydrogen peroxide production from solar water oxidation, ACS Energy Lett 4 (2019) 3018–3027.

78. X. Chen, Y. Kondo, Y. Kuwahara, K. Mori, C. Louis, H. Yamashita, Metal-organic framework-based nanomaterials for photocatalytic hydrogen peroxide production, Phys. Chem. Chem. Phys. 22 (2020) 14404–14414.

79. J. Zhang, L. Zheng, F. Wang, C. Chen, H. Wu, S. Leghari, M. Long, The critical role of furfural alcohol in photocatalytic H_2O_2 production on TiO_2, Appl. Catal. B 269 (2020), 118770.

80. H. Zhao, Q. Jin, M. Khan, S. Larter, S. Siahrostami, M. Kibria, J. Hu, Rational design of carbon nitride for remarkable photocatalytic H_2O_2 production, Chem Catal (2022), https://doi.org/10.1016/j.checat.2022.04.015.

81. Y. Ding, S. Maitra, S. Halder, C. Wang, R. Zheng, T. Barakat, S. Soy, L-H. Chen, BL. Su, Emerging semiconductors and metal-organic-compounds-related photocatalysts for sustainable hydrogen peroxide production, Matter (2022), https://doi.org/10.1016/j.matt.2022.05.011.

82. S. Wu, H. Yu, S. Chen, X. Quan, Enhanced photocatalytic H_2O_2 production over carbon nitride by doping and defect engineering, ACS Catal 10 (2020) 14380–14389.

83. L. Wang, J. Zhang, Y. Zhang, H. Yu, Y. Qu, J. Yu, Inorganic Metal-Oxide Photocatalyst for H_2O_2 Production, Small 18 (2022), 2104561.

84. J. Lei, B. Chen, W. Lv, L. Zhou, L. Wang, Y. Liu, J. Zhang, Robust photocatalytic H_2O_2 production over inverse opal g-C_3N_4 with carbon vacancy under visible light, ACS Sustain. Chem. Eng. 7 (2019) 16467–16473.

85. S. Lin, N. Zhang, F. Wang, J. Lei, L. Zhou, Y. Liu, J. Zhang, Carbon vacancy mediated incorporation of Ti_3C_2 quantum dots in a 3D inverse opal g-C_3N_4 Schottky junction catalyst for photocatalytic H_2O_2 production, ACS Sustain. Chem. Eng. 9 (2020) 481–488.

86. N.T. Suen, S.F. Hung, Q. Quan, N. Zhang, Y.J. Xu, H.M. Chen, Electrocatalysis for the oxygen evolution reaction: recent development and future perspectives, Chem. Soc. Rev. 46 (2017) 337–365.

87. M. Tahir, L. Pan, F. Idrees, X. Zhang, L. Wang, J.J. Zou, Z.L. Wang, Electrocatalytic oxygen evolution reaction for energy conversion and storage: a comprehensive review, Nano Energy 37 (2017) 136–157.

88. J. Stacy, Y.N. Regmi, B. Leonard, M. Fan, The recent progress and future of oxygen reduction reaction catalysis: A review, Renew. Sust. Energ. Rev. 69 (2017) 401–414.

89. F. Safizadeh, E. Ghali, G. Houlachi, Electrocatalysis developments for hydrogen evolution reaction in alkaline solutions-a review, Int. J. Hydrog. Energy 40 (2015) 256–274.

90. H. Wang, W. Fu, X. Yang, Z. Huang, J. Li, H. Zhang, Y. Wang, Recent advancements in heterostructured interface engineering for hydrogen evolution reaction electrocatalysis, J. Mater. Chem. A 8 (2020) 6926–6956.

91. L. Tian, X. Yan, X. Chen, Electrochemical activity of iron phosphide nanoparticles in hydrogen evolution reaction, ACS Catal 6 (2016) 5441–5448.

92. J. Ai, R. Jin, Z. Liu, J. Jiang, S. Yuan, G. Huang, N. Li, X. Li, Three-dimensionally ordered macroporous FeP self-supported structure for high-efficiency hydrogen evolution reaction, Int. J. Hydrog. Energy 44 (2019) 5854–5862.

93. T. Sun, C. Zhang, J. Chen, Y. Yan, A.A. Zakhidov, R.H. Baughman, L. Xu, Threedimensionally ordered macro-/mesoporous Ni as a highly efficient electrocatalyst for the hydrogen evolution reaction, J. Mater. Chem. A 3 (2015) 11367–11375.

94. Y. Wu, F. Ning, Z. Wang, A. Saad, X. Li, D. Xia, 3D ordered macroporous copper nitride-titanium oxynitride as highly efficient electrocatalysts for universal-pH hydrogen evolution reaction, J. Mater. Chem. A 9 (2021) 14392–14399.

95. J. Wang, Y. Niu, X. Teng, S. Gong, J. Huang, M. Xu, Z. Chen, Construction of three-dimensionally ordered macroporous bimetal phosphides as bifunctional electrocatalysts for highly efficient water splitting, J. Mater. Chem. A 8 (2020) 24572–24578.

96. W. Hu, Y. Wang, X. Hu, Y. Zhou, S. Chen, Three-dimensional ordered macroporous IrO_2 as electrocatalyst for oxygen evolution reaction in acidic medium, J. Mater. Chem. 22 (2012) 6010–6016.

97. W. Hu, P. Zhou, S. Xu, S. Chen, Q. Xia, Template synthesis of 3-DOM IrO_2 powder catalysts: temperature-dependent pore structure and electrocatalytic performance, J. Mater. Sci 50 (2015) 2984–2992.

98. F. Liu, X. Sun, X. Chen, C. Li, J. Yu, H. Tang, Synthesis and Characterization of 3-DOM IrO_2 Electrocatalysts Templated by PMMA for Oxygen Evolution Reaction, Polymers 11 (2019) 629.

99. D. Yang, L. Zhang, X. Yan, X. Yao, Recent progress in oxygen electrocatalysts for zinc-air batteries, Small Methods 1 (2017), 1700209.

100. M.I. Jamesh, P. Moni, A.S. Prakash, M. Harb, ORR/OER activity and zinc-air battery performance of various kinds of graphene-based air catalysts, Mater. Sci. Energy Technol. 4 (2021) 1–22

101. S. Ren, X. Duan, S. Liang, M. Zhang, H. Zheng, Bifunctional electrocatalysts for Zn–air batteries: recent developments and future perspectives, J. Mater. Chem. A 8 (2020) 6144–6182.

102. Z. Cai, S. Lin, J. Xiao, T. Muhmood, X. Hu, 3D Ordered Co@ N-C Skeleton for Bifunctional Oxygen Reduction and Oxygen Evolution Reaction Electrocatalysts, Adv. Mater. Interfaces 8 (2021), 2001922.

103. J. Liang, Y. Zheng, J. Chen, J. Liu, D. Hulicova-Jurcakova, M. Jaroniec, S.Z. Qiao, Facile oxygen reduction on a three-dimensionally ordered macroporous graphitic C_3N_4/carbon composite electrocatalyst, Angew. Chem. Int. Ed. 51 (2012) 3892–3896.

104. H. Lin, S. Wang, Z. Zhang, Z. Dai, S. Tan, D. Chen, A highly efficient electrocatalyst for oxygen reduction reaction: three-dimensionally ordered macroporous perovskite $LaMnO_3$, J. Power Sources 412 (2019) 701–709.

105. C. Zhang, H. Yang, T. Sun, N. Shan, C. Hen, L. Xu, Y. Yan, Synthesis of threedimensionally ordered macro-/mesoporous Pt with high electrocatalytic activity by a dual-templating approach, J. Power Sources 245 (2014) 579–582.

Chapter 2

B-doped g-C_3N_4 hierarchical architecture for photo/electrocatalytic reactions

A series of hydrophilic bi-functional B-doped g-C_3N_4 hierarchical nanoplatelets were manufactured for highly efficient photocatalytic H_2O_2 production and photoelectrochemical water splitting. In this chapter, the detailed mechanisms of the increased photocatalytic performance were thoroughly investigated. Specifically, my contribution for the work is that the develop of the oxidation exfoliation method to prepare the new hydrophilic 2D C_3N_4 structure, conducting the materials characterization and the analysis of the experimental results.

(This work has been published on **Journal of Energy Chemistry 2022, 70, 236-247** by Yang Ding et al.)

Hydrophilic bi-functional B-doped g-C_3N_4 hierarchical architecture for excellent photocatalytic H_2O_2 production and photoelectrochemical water splitting

Yang Ding [a,b,], Soumyajit Maitra [c], Chunhua Wang [d], Runtian Zheng [a,b], Meiyu Zhang [e], Tarek Barakat [a,b], Subhasis Roy [c], Jing Liu [f], Yu Li [f,*], Tawfique Hasan [g], Bao-Lian Su [a,b,f,h],*

[a] Laboratory of Inorganic Materials Chemistry (CMI), University of Namur, 61 rue de Bruxelles, B-5000 Namur, Belgium

[b] Namur Institute of Structured Matter (NISM), University of Namur, 61 rue de Bruxelles, B-5000 Namur, Belgium

[c] Department of Chemical Engineering, University of Calcutta, 92 APC Road, West Bengal, Kolkata 700009, India

[d] Department of Chemistry, KU Leuven, Celestijnenlaan 200F, B-3001 Leuven, Belgium

[e] State Key Laboratory of Applied Organic Chemistry, Key Laboratory of Nonferrous Metals Chemistry and Resources Utilization of Gansu Province, College of Chemistry and

Chemical Engineering, Lanzhou University, Lanzhou 730000, Gansu, China

[f] State Key Laboratory of Advanced Technology for Materials Synthesis and Processing, Wuhan University of Technology, Wuhan 430070, Hubei, China

[g] Cambridge Graphene Centre, University of Cambridge, Cambridge, CB3 0DS, UK

[h] Clare Hall, University of Cambridge, United Kingdom, CB2 1EW, UK

Abstract

Graphitic carbon nitride (g-C_3N_4) has attracted great interest in photocatalysis and photoelectrocatalysis. However, their poor hydrophilicity poses a great challenge for their applications in aqueous environment. Here, we demonstrate synthesis of a hydrophilic bi-functional hierarchical architecture by the assembly of B-doped g-C_3N_4 nanoplatelets. Such hierarchical B-doped g-C_3N_4 material enables full utilization of their highly enhanced visible light absorption and photogenerated carrier separation in aqueous medium, leading to an excellent photocatalytic H_2O_2 production rate of 4240.3 $\mu M\ g^{-1}\ h^{-1}$, 2.84, 2.64 and 2.13 times higher than that of the bulk g-C_3N_4, g-C_3N_4 nanoplatelets and bulk B doped g-C_3N_4, respectively. Photoanodes based on these hierarchical architectures can generate an unprecedented photocurrent density of 1.72 mA cm^{-2} at 1.23 V under AM 1.5 G illumination for photoelectrochemical water splitting. This work makes a fundamental improvement towards large-scale exploitation of highly active, hydrophilic and stable metal-free g-C_3N_4 photocatalysts for various practical applications.

Keywords:

Boron doping; Hydrophilicity; Hierarchically assembled architectures; Photocatalytic H_2O_2 production; Photoelectrocatalytic water splitting

1. Introduction

As a metal-free photocatalyst, graphitic carbon nitride (g-C_3N_4) has recently attracted an increasing interest for various photocatalytic applications. Moreover, its typical n-type semiconductor properties endow the majority of carriers in g-C_3N_4 are electrons and thus are quite suitable for photoreduction reactions like photocatalytic H_2O_2 production by ORR reaction, photocatalytic CO_2 reduction and photocatalytic H_2 production.**[1-9]** However, g-C_3N_4 offers limited photocatalytic activity because of its inefficient visible light absorption, low specific surface area, high recombination rate of photogenerated carriers and, in particular, poor dispersion in aqueous reaction medium.**[10-13]** Improvement in these areas remains a great challenge towards their practical applications.

Nonmetal ion doping of carbon nitride has been shown to be an efficient way not only to improve the visible light absorption by narrowing the band gap of g-C_3N_4, but also to promote the photogenerated carrier separation due to the formation of midgap state.**[14–19]** Oxygen self-doped g-C_3N_4 exhibits 4 times higher hydrogen evolution rate than that of pristine g-C_3N_4 due to improved visible light absorption.**[15]** P doped g-C_3N_4 demonstrates 2.9 times higher hydrogen evolution rate than that of pure g-C_3N_4 through suppression of photogenerated carrier recombination.**[17]** Zhang *et al*. reported a carbon doped g-C_3N_4 by one-step pyrolysis of the mixture of kapok fiber and melamine, exhibiting higher photocatalytic H_2 evolution rate than that of the pristine g-C_3N_4 under visible-light.**[19]** Changes in structure and morphology are also of high importance for photocatalytic performance improvement.**[20–30]** For example, Fu's group developed a two dimensional (2D) porous carbon nitride which exhibits 26-fold higher hydrogen evolution activity than the bulk counterpart.**[28]** Zhu *et al*. designed a 3D porous g-C_3N_4 assembled by ultrathin nanosheets with excellent photocatalytic water splitting.**[29]**

Additionally, Xu's team reported 3D hierarchical g-C_3N_4 nanosheets with outstanding photocatalytic activity for hydrogen production.**[30]** Specifically, these 2D and 3D hierarchical architectures with porous structures demonstrate increased photocatalytic performance because of their interconnected and easily accessible network that provide more active sites and reactant transport channels for photocatalytic reactions. Doping with simultaneous morphology modulation of g-C_3N_4 has also been explored to improve photocatalytic activity.**[31–34]** For example, Lv's group designed a three dimensional B doped g-C_3N_4 hierarchical architecture with an interconnected network of graphene-analogue nanosheets for improved catalytic activity and stability.

The strong van der Waals attractions (π-π stacking) between *sp*^{2} carbon atoms make g-C_3N_4 poorly dispersible in aqueous solution.**[11,12]** This is unfavorable for photocatalytic and photoelectrocatalytic reactions which are generally conducted in the aqueous environment. This poor hydrophilic character of g-C_3N_4 is often neglected over other considerations in materials design, leading to photocatalytic performances far below the expected level. This is because although modified g-C_3N_4 materials show highly improved light absorption, charge separation and other desirable properties, these can not be fully exploited in aqueous medium due to their poor dispersion and easy aggregation in water, severely restricting their application in photocatalysis. Improving their surface hydrophilic character can facilitate their dispersion and also allow close contact with water, promoting photocatalytic reactions [8,35]. Yu et al. reported that g-C_3N_4 nanosheets containing different hydrophilic groups (–NH_2, –OH and –C=O) on the surface of nanosheets could give a better wettability, leading to an improved photocatalytic H_2 production.**[35]** Although mixing with hydrophilic compounds can also effectively improve the dispersion of g-C_3N_4 in aqueous medium and thus the photocatalytic activity, their performance remains largely unsatisfactory for practical applications. It is clear that significantly improving the intrinsic hydrophilicity of g-C_3N_4 is a key to full exploitation of modified g-C_3N_4 in aqueous reaction environments.**[8]**

Herein, using an innovative preparation process, we design and synthesize hydrophilic bi-functional hierarchical architectures assembled by 2D boron doped g-C_3N_4 nanoplatelets (2D-B-CN) with high porosity and surface area. Firstly, g-C_3N_4 is in-situ doped by B ions through a one pot thermal polymerization of a mixture of melamine and boron oxide to create bulk B doped g-C_3N_4 (bulk B-CN). Nanoplatelets with ~2.5 nm in thickness are then obtained from this using an effective ultrasonic oxidative exfoliation process and are self-assembled to give a hierarchically stacked architecture of nanoplatelets. Such hierarchical assembly of B doped g-C_3N_4 nanoplatelets (2D-B-CN) exhibits ~8 times higher specific surface area and complete dispersion in aqueous medium due to improved hydrophilic character compared to the bulk samples with or without B doping (bulk-CN and bulk-B-CN-4). Their excellent dispersion enables full exploitation of the advantages offered by B doping of g-C_3N_4 for photocatalysis. By controlling the doping amounts of B ions, visible light absorption, charge separation and surface charge transfer capacity of the obtained materials can be effectively controlled. Density functional theory (DFT) calculations further illustrate the electronic structure evolution of g-C_3N_4 upon B ions doping, which significantly broadens the absorption in the visible light range and efficiently promotes the photoinduced carrier separation for photoredox reaction. Our hierarchically assembled B doped g-C_3N_4 nanoplatelets with their synergistic B doping and hydrophilic nature, in addition to high surface area and hierarchical porosity, exhibit excellent performance both for photocatalytic H_2O_2 production and photoelectrochemical water splitting for H_2 production. A photocatalytic H_2O_2 production rate of 4240.3 μM g^{-1} h^{-1}, 2.84, 2.64 and 2.13 times higher than that of bulk g-C_3N_4, hierarchical g-C_3N_4 nanoplatelets and bulk B doped g-C_3N_4, respectively, is observed. Additionally, photoelectrodes based on our materials can generate an impressive photocurrent density of 1.72 mA cm^{-2} at 1.23 V versus reversible hydrogen electrode (RHE) under AM 1.5 G illumination for PEC water splitting, 2.5, 1.6 and 1.4 folds greater than that of the above material configurations. The significant change in hydrophilic character brings a fundamental benefit to the performance of our modified g-C_3N_4 based material. The strong hydrophilic character is crucial to guarantee full exploitation of the above-mentioned advanced properties in aqueous medium, significantly improving the utilization efficiency of our material. Our photocatalysts demonstrate the best performance both in photocatalytic H_2O_2 production and in photoelectrochemical water splitting for H_2 production compared to all the g-C_3N_4 based photocatalysts reported in the literature, validating our strategy towards large scale exploitation of modified g-C_3N_4 as a highly efficient photocatalyst.

2. Experimental

2.1. Materials

All chemicals used in this work were purchased from Aladdin Ltd. and used without further purification. Distilled water was used in the whole experiment process.

2.2. Preparation of 2-D hierarchical B doped g-C_3N_4 nanoplatelets

The typical 4% (molar ratio) B doped g-C_3N_4 nanoplatelets were prepared by a two-steps process: one pot thermal polymerization, followed by exfoliation. Firstly, a mixture of melamine and boron oxide was grinded and calcinated in a crucible at 550 °C for 5 h in air. After naturally cooling to room temperature, the obtained light-yellow powder (bulk-B-CN-4) was carefully collected. The obtained powder sample (2 g) was added to 50 mL of the mixed solution of concentrated HNO_3 and H_2O_2 (1:1 volume ratio), and was put into an ultrasound bath for 2 h. After that, the mixture was neutralized by 1 M KOH and centrifuged at 3000 r min^{-1} with 3 washing cycles with distilled water and ethanol. The precipitates were collected and dried in air to obtain 2D-B-CN-4. For comparison, the nanoplatelets with various B doping ratios of 0%, 2%, 6% and 8% were prepared through the same method and were denoted as 2D-B-CN-0, 2D-B-CN-2, 2D-B-CN-6, and 2D-B-CN-8, respectively. The bulk g-C_3N_4 sample (bulk-CN) was synthesized by calcinating melamine at 550 °C for 5 h in air. A summary of all the samples studied in this work is given in Table S1.

2.3. Characterizations

X-ray diffraction (XRD) patterns were obtained on a Bruker D8 system with Cu K_α radiation (λ = 0.15405 nm) with a scanning rate and range of 4° min^{-1} and 10–50°, respectively. Scanning electron microscopy (SEM) observation was carried out using an JEOL 7500 F field-emission SEM. Transmission electron microscopy (TEM) images of the samples were analyzed on polymer coated copper grids by using a TECNAI 10 at an acceleration voltage of 100 kV. Atomic force microscopy (AFM) image of the sample was studied by a Park XE70 AFM (Park Systems Corp., Korea). Nitrogen adsorption-desorption isotherms were detected using an ASAP 2420 surface area & porosity analyzer at 77 K. The specific surface area was calculated by Brunauer-Emmett-Teller (BET) method. The pore size distribution is calculated by the Barrett-Joyner-Halenda (BJH) and non local density functional theory (NLDFT) analysis methods. X-ray photoelectron spectroscopy (XPS) characterization was performed in a Thermo Fisher ESCALAB 250 Xi instrument with a monochromatic Al K_α x-ray source. The UV-visible diffused reflectance spectra were collected by a UV-visible spectrophotometer (Perkin Elmer Lambda 35 UV-visible spectrometer fitted with a Integrating sphere for analysis in diffuse reflectance mode) in the wavelength range of 200–700 nm. Photoluminescence properties of the samples were investigated by a Perkin Elmer LS45 luminescence spectrophotometer at room temperature. The elemental analysis was performed using Inductively coupled plasma-atomic emission spectrometry (ICP-AES) (Perkin-Elmer Optima 8000 Spectrometry).

2.4. Photocatalytic H_2O_2 production experiments

Typically, 20 mg of photocatalyst was dissolved in the mixture of water (19 mL) and isopropanol (1 mL). The solution was bubbled with O_2 for 10 min to make the system saturated with O_2. Before the light irradiation, the solution was put in a dark box and magnetically stirred for 30 min to reach an adsorption-desorption equilibrium. The photocatalytic reaction was then performed under visible light irradiation (400–800 nm) by using 6 neon lamps of 20 W at room temperature. Finally, 2 mL of solution was removed at a given time interval and immediately centrifuged for the separation of photocatalyst for further test. The production of H_2O_2 was detected by the typical iodometry method.[18,23] Briefly, 1 mL of 0.1 mol L^{-1} ammonium molybdate tetrahydrate ($(NH_4)_6Mo_7O_{24}$) aqueous solution and 1 mL of 0.4 mol L^{-1} potassium iodide (KI) aqueous solution were added to 2 mL of filtrate, which was then kept for 1 min. The H_2O_2 molecules reacted with iodide anions (I^-) under acidic conditions to produce I^{3-} anions, which exhibits a strong optical absorption at ~350 nm. The amount of I^{3-} was analyzed by UV-visible spectroscopy from which the amount of H_2O_2 was subsequently calculated.

2.5. Photoelectrochemical measurements

The photoelectrochemical measurement was conducted in a typical three-electrode cell by using computer-controlled electrochemical workstation (CHI 660E).[14,15] Typically, 10 mg sample was added into the mixed solution of deionized water (10 μL) and Nafion (50 μL). After ultrasonic treatment for 10 min, the prepared homogeneous suspension (50 μL) was uniformly sprayed onto the surface of indium tin oxide (ITO) (1.0 × 1.0 cm) coated glass. The ITO glass with photocatalyst served as the working electrode, while a the Pt plate and saturated calomel electrode (SCE) were used as the counter electrode and the reference electrode, respectively. 0.1 M Na_2SO_4 solution was used as the electrolyte in this three-electrode cell system. The visible light was provided by a xenon arc lamp PLS-SXE-300C with a 420 nm cut-off filter. The photocurrent-time (*I-t*) curves were collected at the open-circuit potential (0.1 V). Electrochemical impedance spectroscopy (EIS) test was carried out in a 0.2 M KCl solution. For the PEC water splitting characterization, the linear sweep voltammetry with a scanning rate of 50 mV s^{-1} was carried out under AM 1.5G illumination (100 mW cm^{-2}) by using a simulated sunlight source. The collected potentials versus SCE electrode were converted to the reversible hydrogen electrode (RHE) according to the following formula: E (RHE) = 0.242 + 0.059 pH+ E(SCE).[15]

2.6. Photocurrent, charge carriers separation and charge transfer efficiency

Generally, the photocurrent density here can be described by the following equation:**[23]**

$$J(Na_2SO_4) = J_{max}\times\eta_{abs}\times\eta_{sep}\times\eta_{trans}(Na_2SO_4). \ (1)$$

Considering that the surface charge transfer is extremely fast in the presence of MV^{2+} so that the $\eta_{trans}(Na_2SO_4+MV)$ almost reaches 100%, the photocurrent density in this condition can be calculated using following equation:

$$J(Na_2SO_4 + MV) = J_{max}\times\eta_{abs}\times\eta_{sep}. \ (2)$$

As the J_{max}, η_{abs}, and η_{sep} are unchanged for the $J(Na_2SO_4)$ and $J(Na_2SO_4+MV)$, the η_{trans} can be calculated by the following equation:

$$\eta_{trans}(Na_2SO_4) = J(Na_2SO_4)/J(Na_2SO_4 + MV). \ (3)$$

2.7. Computational details

DFT calculations were performed using GGA functional with PBE exchange correlation and Ultrasoft type pseudopotentials with Koelling-Hammon relativistic treatment and Grimme parameters to account for DFT-D (vdW) correction arising from interlayer interactions. Band structure and DOS calculations were carried out using CASTEP code. Plane wave cut-off was set at 570 eV. SCF cut-off was set at 1E−6 eV. Geometry optimization was carried out using PBE+D2 functional using a linear search BFGS algorithm with energy cut-off set at 1E−7 eV with maximum force set at 0.004 eV Å^{-1} and maximum displacement set to 0.001 Å using Fixed Basis Quality cell optimization. The concentration of B dopant in 2D-B-CN for all theoretical calculation is 4.177 atomic % in this work.

3. Results and discussion

3.1. Structure, morphology and surface properties

The preparation process of the hydrophilic bi-functional hierarchically assembled g-C_3N_4 nanoplatelets is illustrated in Scheme S1. This is a one pot solid state reaction to form bulk B doped g-C_3N_4 (bulk B-CN) followed by ultrasonic oxidative exfoliation in presence of HNO_3/H_2O_2 mixture. Using this process, we prepared a series of hierarchical 2D-B-CN nanoplatelets with different B doping molar ratios (0, 2, 4, 6 and 8%), giving 2D-B-CN-*X* (*X* = 0, 2, 4, 6 and 8, respectively) samples. A bulk g-C_3N_4 (bulk-CN) as a reference sample was prepared. In addition, a bulk-B-CN-4 (i.e. with a B doping of 4%) without exfoliation was also used as a doped reference sample. The detailed preparation information and a summary of all the studied samples are given in Experimental section and in Table S1, respectively.

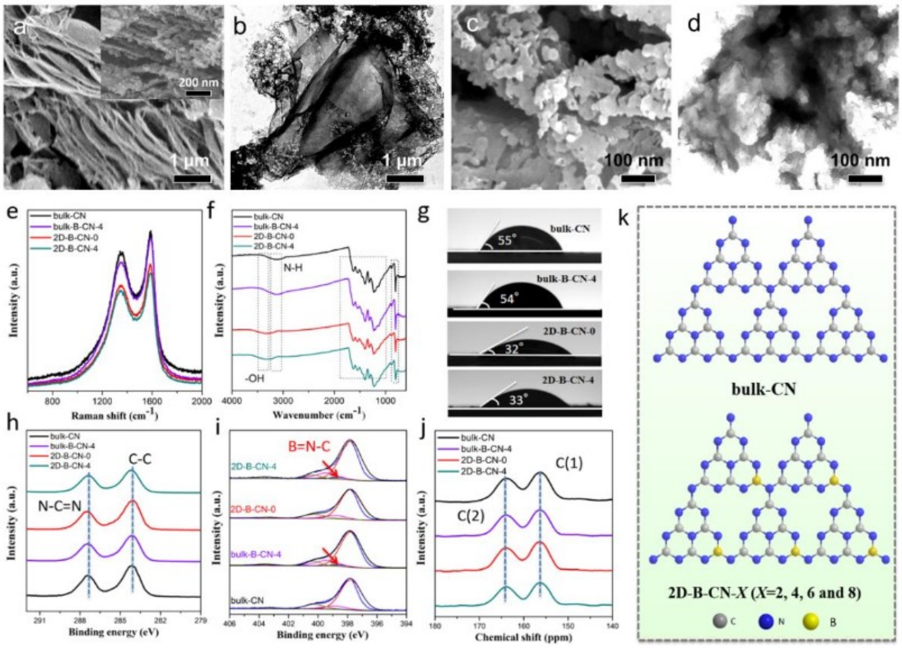

Fig. 1. (a and c) SEM and (b and d) TEM images of the as-synthesized 2D-B-CN-4 sample. (e) Raman spectra, (f) FT-IR spectra, (g) images of water droplets on the thin films, (h) high-resolution C 1*s* spectra, (i) high-resolution N 1*s* spectra and (j) solid-state ^{13}C MAS NMR spectra of the as-prepared bulk-CN, bulk-B-CN-4, 2D-B-CN-0, and 2D-B-CN-4 samples. (k) The detailed structures of bulk-CN and 2D-B-CN samples.

Both bulk-CN and bulk-B-CN-4 samples present an irregular aggregation of particles with a particle size distribution between 0.1 to 3 μm (Fig. S1a and b). TEM images in Fig. S1(c and d) shows ~ 8 nm pores (in red circles) on the edges of both bulk samples from the packing of nanoparticles. The SEM images of 2D-B-CN-4 nanoplatelets as the representative sample in Fig. 1(a) and inset show that the hierarchical architecture is assembled by stacking of large nanoplatelets. The TEM image of 2D-B-CN-4 displays an individual ultrathin nanoplatelet structure (Fig. 1b). Fig. 1(c) clearly demonstrates that each large nanoplatelet is composed of very small nanoplatelets of several tens of nanometers, giving abundant interparticular porosity. The enlarged TEM image (Fig. 1d) further suggests that a single large nanoplatelet composed of numerous small nanoplatelets presents the hierarchical porous structure due to the packing of the small nanoplatelets. The elemental mapping images in Fig.

S1(e) exhibit very homogeneous distribution of C, N and B in 2D-B-CN-4 sample. The AFM image and cross-section analysis of 2D-B-CN-4 (Fig. S1f) suggest that the layer thickness of small nanoplatelets in 2D-B-CN-4 is about 2.5 nm, corresponding to 5 layers of g-C_3N_4.[28,29] XRD patterns of the as-prepared bulk-CN, bulk B-CN-4, 2D-B-CN-0 and hierarchically assembled B doped g-C_3N_4 nanoplatelet (2D-B-CN-*X*, *X* = 2, 4, 6 and 8) samples are shown in Fig. S2(a). For bulk-CN, the strong peak at 27.65° of the typical (002) plane belongs to the inter-layer stacking of aromatic segments, whereas the weak peak at 13.05° can be attributed to the in-planar structural packing motif.[13–15] Compared with bulk-CN, the peak belonging to (002) plane of bulk-B-CN-4 and 2D-B-CN-*X* (*X* = 0, 2, 4, 6 and 8) samples shows a slight shift toward higher angles with exfoliation and increasing of B dopants (Fig. S2b), suggesting a decrease in inter-layer stacking distance of g-C_3N_4.[2,3,13,14] As we will propose later, such a change in the stacking favors photo-induced charge separation and transportation.[30,35]

Fig. 1(e) presents the Raman spectra of the as-prepared bulk-CN, bulk-B-CN-4, 2D-B-CN-0 and 2D-B-CN-4 samples. The two peaks at ~1350 and ~1570 cm^{-1} correspond to the vibration modes of heterocycles and C=N stretching vibration in g-C_3N_4, respectively. 2D-B-CN-0 and 2D-B-CN-4 display nearly identical Raman spectra, indicating that the B doping has negligible impact on its intrinsic triazine ring structure. 2D-B-CN-0 and 2D-B-CN-4 give a blue shift of about 3 cm^{-1} compared with bulk-CN and bulk-B-CN-4, which is ascribed to the phonon confinement effect of exfoliated nanoplatelets, suggesting very thin nanoplatelet structure.[13] The structures and surface groups of the four samples were studied by Fourier transform infrared (FT-IR) spectroscopy and is shown in Fig. 1(f). The characteristic peaks located at around 810 and 900–1800 cm^{-1} for all the samples are attributed to the typical bands for bending mode of heptazine rings and N-C=N/N-C_3 of the melon unit in the framework, respectively.[15,18,19] This demonstrates that the B doping just influences the ordered unit arrangement and interlayer structure but does not modify the fundamental structure of C_3N_4. Compared with bulk-CN and bulk-B-CN-4, the intensities of the N–H peak located at 3000–3300 cm^{-1} for 2D-B-CN-0 and 2D-B-CN-4 are weaker, while the OH stretching vibrations located at ~3500 cm^{-1} are stronger, indicating more abundant OH groups on the surface of these two exfoliated 2D g-C_3N_4 nanoplatelets. We propose that these additional hydrophilic OH groups originated from H_2O molecules in solution during the ultrasonic oxidative exfoliation process. The presence of large amounts of hydrophilic OH groups leads to the improved hydrophilic character of g-C_3N_4, essential for their good dispersion in aqueous reaction medium, favoring photocatalytic reaction. The adsorption of reactant molecules on the surface of photocatalysts is a key step of the photocatalytic reaction. Thus, the hydrophilic properties of the photocatalyst stemming from these OH groups are very crucial for the significant improvement of photocatalytic performance.[35] Fig. 1(g) shows water droplets on the thin films of these four samples. The bulk-CN and bulk-B-CN-4 samples present a very similar and a relatively large contact angle, indicating that B doping did not affect the hydrophilicity of g-C_3N_4. The significantly reduced contact angles for the case of 2D-B-CN-0 and 2D-B-CN-4 indicate highly improved hydrophilic character compared to the bulk-CN and bulk-B-CN-4 samples. Fig. S3(a) shows the photograph of 5 mL of bulk-CN, bulk-B-CN-4, 2D-B-CN-0 and 2D-B-CN-4 aqueous solution at 10 mg mL^{-1} concentration kept undisturbed for 3 days, demonstrating the excellent dispersion and stability of 2D-B-CN-0 and 2D-B-CN-4 compared to the bulk CN and bulk B-CN samples. Images of water droplets and measured contact angles on the 2D-B-CN-2, 2D-B-CN-6 and 2D-B-CN-8 samples are shown in Fig. S3(b). All the exfoliated samples present a significantly reduced contact angle, indicating their excellent hydrophilicity. The similar values of contact angle for all the exfoliated 2D samples (2D-B-CN-X; with $X = 0, 2, 4, 6$ and 8) confirm again that their hydrophilicity of g-C_3N_4 is originated from the exfoliation process and not from the B doping. This significantly improved hydrophilicity by oxidative ultrasonic exfoliation process guarantees full exploitation of the advanced properties of B doped g-C_3N_4 nanoplatelets in the aqueous environment.[19]

Fig. S4(a) shows the XPS spectra of bulk-CN, bulk-B-CN-4, 2D-B-CN-0 and 2D-B-CN-4 samples. Compared with bulk-CN and 2D-B-CN-0, the 2D-B-CN-4 and bulk B-CN-4 exhibits the peak of B 1*s*, indicating that the B atoms have been successfully introduced into g-C_3N_4. For the representative 2D-B-CN-4 sample, the concentration of B dopant is only 4% according to XPS analysis. To ensure the accurate B doping amount, we have also conducted the elemental analysis of the optimal 2D-B-CN-4 sample, the B concentration is about 3.95%, which is quite similar to XPS result and the theoretical value. Moreover, the higher peak intensity of O 1*s* for both 2D-B-CN-0 and 2D-B-CN-4 indicate the presence of more oxygen based species associated with the hydrophilic surface nature of the exfoliated 2D-B-CN nanoplatelets. The high-resolution C 1*s* spectra of the as-prepared samples are shown in Fig. 1(h). All the samples display two distinct peaks at 287.2 and 284.6 eV. The peak at 284.6 eV belongs to the adventitious carbon (C–C), while the former is attributed to the main carbon species of sp^2 carbon atoms bonded to nitrogen (N–C=N).[16–19] Compared with bulk-CN, the slightly reduced intensity of the peak at 287.2 eV for

2D-B-CN-4 and bulk-B-CN-4 implies substitution of carbon atoms by boron atoms. The high-resolution N 1*s* spectra of the bulk-CN and 2D-B-CN-0 in Fig. 1(i) and Fig. S4(c) is composed of four peaks at about 397.9, 398.5, 400.4 and 403.8 eV, and are attributed to sp^2 bonded N in triazine rings (C=N–C), the bridging N atoms in $N–C_3$, terminal N–H and N–O in the cyano group and heterocycles, respectively.**[9-11]** Due to the substitution of C by B atoms, the new B=N–C bonds at 398.5 eV are formed in the bulk-B-CN-4 and 2D-B-CN-4 spectra (red arrows in Fig. 1i).**[16,23]** Fig. S4(b) shows the B 1*s* spectrum of bulk-B-CN-4 and 2D-B-CN-4. The peak at 192.4 eV is attributed to the binding energy of the N–B=N group for B doped $g-C_3N_4$,**[23]** suggesting that N=B–N bonds are formed between the doped boron atoms and surrounding N atoms. These observations further indicate that B atoms are successfully introduced into the $g-C_3N_4$ framework. Fig. 1(j) presents the solid-state ^{13}C NMR spectra of bulk-CN, bulk-B-CN-4, 2D-B-CN-0 and 2D-B-CN-4 samples. All the samples show two strong peaks at 156.8 and 164.7 ppm, corresponding to the characteristic C(1) atoms of N=C–N2 and C(2) atoms of N=C–N(NHx) in the heptazine units, respectively.**[28,29]** Compared with bulk-CN and 2D-B-CN-0 samples without B doping, the peak intensity ratio between C(2) and C(1) for 2D-B-CN-4 and bulk-B-CN-4 with B doping is noticeably reduced (Table S2), indicating that the C(2) atoms are replaced by B atoms. Based on the XPS and ^{13}C NMR spectra results, we propose the detailed structures (Fig. 1k) of bulk-CN and 2D-B-CN-*X* (X = 2, 4, 6 and 8) samples.

The specific surface area and pore size distributions of all the samples were analyzed by N_2 adsorption-desorption. As shown in Fig. S5(a), all the samples present a similar shape of type II isotherm containing mesopores in the samples.**[36–39]** The bulk-CN sample shows a very low specific surface area of 12.2 $m^2\ g^{-1}$ with a narrow pore size distribution centered at 8.2 nm (Table S3). The similar specific surface area and narrow pore size distribution for bulk-B-CN-4 imply that doping has negligible influence on its micro-structure. The mesopores for both bulk samples are ascribed to the packing of nanoparticles. All the exfoliated 2D-B-CN-*X* (X = 0, 2, 4, 6 and 8) samples have much higher specific surface area (~100 $m^2\ g^{-1}$). This confirms that while the B doping has almost no impact on the surface area (Table S3), the oxidative ultrasonic exfoliation process improves it by at least 8 times. The pore size distributions depicted in Fig. S5(b) of all the exfoliated samples are centered at ~11–13 nm, further demonstrating the existence of abundant mesopores in the hierarchically assembled nanoplatelets owing to our innovative preparation process. Compared with the bulk-CN and bulk-B-CN-4, the pore size distributions of 2D-B-CN samples are broader. In addition to improved hydrophilic character, the higher specific surface area due to the exfoliation process offers more accessible active sites and hierarchical pore structure, favoring mass diffusion for enhanced photocatalytic and photoelectrochemical performance in the aqueous environment.

3.2. Band gap structure and DFT calculation

The light absorption properties of all the samples were investigated via UV-vis diffuse reflectance spectroscopy (Fig. S6a). The bulk-CN sample exhibits limited visible light absorption beyond ~465 nm. Compared with bulk-CN, the hierarchical 2D-B-CN-0 nanoplatelets without B doping show a slight red-shift, probably attributed to the surface group modification after exfoliation and contraction of the valence band edges of g-C_3N_4 [8, 35]. When the B ions are introduced, the 2D-B-CN-*X* (*X* = 2, 4, 6 and 8) and bulk B-CN samples show significantly broadened response in the visible light regions and the absorption intensities are gradually increased. This demonstrates that the band gap is effectively narrowed with B doping. According to the Tauc Plots (Fig. S6b),**[40–43]** the band gap values of bulk-CN and 2D-B-CN-0 without B doping are 2.63 and 2.58 eV, respectively, indicating that the exfoliation does not noticeably change the electronic structure. Instead, we observe a gradual decrease of band gap with increasing the B doping amount. This suggests that the B doping leads to a reduction of the band gap which can improve the solar light utilization ability of the material. The specific band gap values of all the samples are shown in Table S3. The enhanced visible light absorption and tunable band structure for 2D-B-CN-*X* (*X* = 2, 4, 6 and 8) and bulk B-CN samples indicate their potential as an effective visible light photocatalyst. Furthermore, the band edges of the samples were characterized by XPS valence band (VB) spectra and presented in Fig. 2(a). The VB value of 2D-B-CN-*X* (*X* = 2, 4, 6 and 8) samples gradually increases with increasing level of B doping, indicating that this process intrinsically changes the electronic structure of g-C_3N_4. The band gap and band alignments values of all the as-prepared samples are shown in Fig. 2b.**[1,14]**

DFT calculations were carried out to establish the electronic structure evolution of g-C_3N_4 upon B doping. When B dopants were introduced into the unit of g-C_3N_4, the doping related midgap states are generated (Fig. 2f) and the bandgap energy of 2D-B-CN-*X* (*X* = 2, 4, 6 and 8) reduces from 2.45 to 1.82 eV (Fig. 2c and f), which is in line with the Tauc Plots. For bulk-CN, the band structure and density of states (DOS) calculations show that both C 2*p* and N 2*p* orbitals contribute to the CB while the VB is mainly composed of N 2*p* orbitals (Fig. 2d), consistent with previous reports [1,10,14,23]. Furthermore, the DOS of 2D-B-CN-*X* (*X* = 2, 4, 6 and 8) shows that the CB is mainly dominated by the N 2*p*, C 2*p* and small amount of B 2*p* orbits, while the VB is composed of the N 2*p* orbit and small amounts of B 2*p* and C 2*p* orbits (Fig. 2g). The magnified PDOS plot of B doped C_3N_4 has been provided in Fig. S6(c). The overlap between the B 2*p* and C 2*p* orbitals in the VB and between N 2*p* and B 2*p* in the CB is observable which are responsible for modulating the electronic structure of the photocatalyst. This reveals that the B doping is much more favorable for reducing the band gap structures of g-C_3N_4 to increase the light absorption (Fig. 2d and g).[14,16,23] Fig. 2(e and h) present the highest occupied molecular orbital (HOMO)

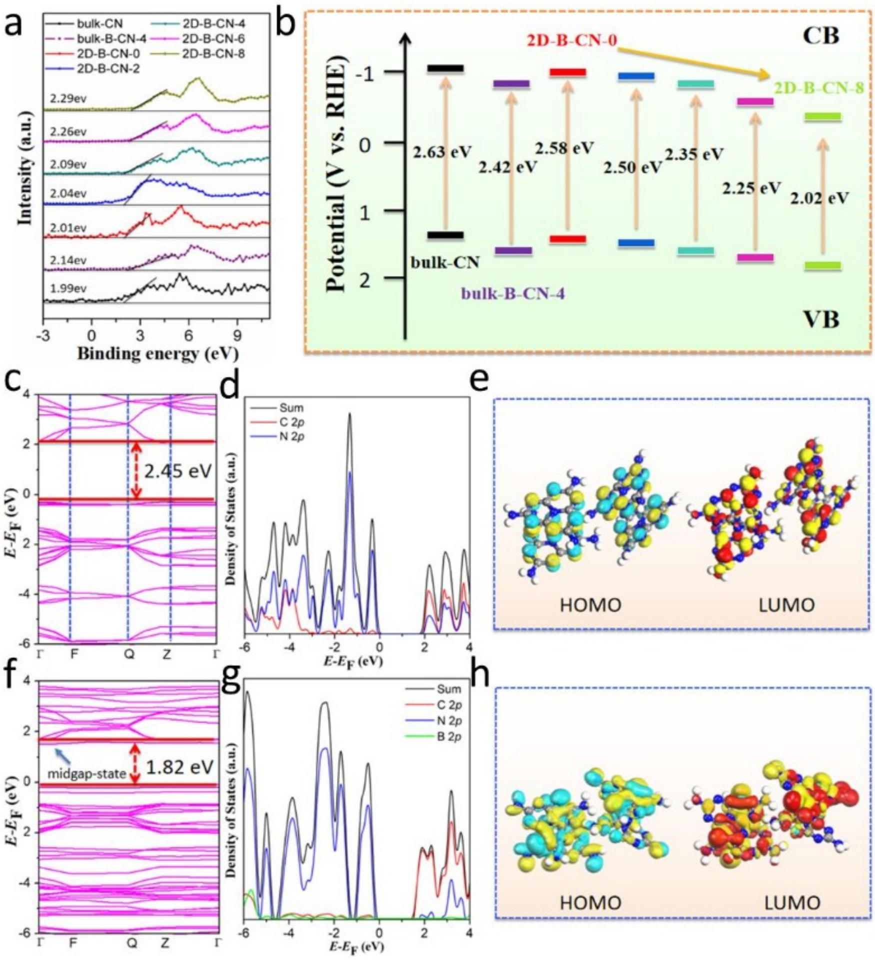

Fig. 2. (a) XPS valence band spectra and (b) schematic energy level diagrams of the as-prepared samples. (c) Calculated band structure and (d) corresponding density of state (DOS) of bulk-CN. (f) calculated band structure and (g) corresponding density of state (DOS)

of 2D-B-CN, respectively. HOMO and LUMO distributions of bulk-CN (e) and 2D-B-CN (h) samples.

and lowest unoccupied molecular orbital (LUMO) locations of bulk-CN and 2D-B-CN-X (X = 2, 4, 6 and 8). Compared with the uniformly delocalized HOMO and LUMO of bulk-CN, the charge density is redistributed with certain electron-rich area in 2D-B-CN-X (X = 2, 4, 6 and 8) (Fig. 2h). Such localized charge accumulation leads to the change of VB and CB positions, which generates dopant- related midgap states in carbon nitride, restricting the recombination

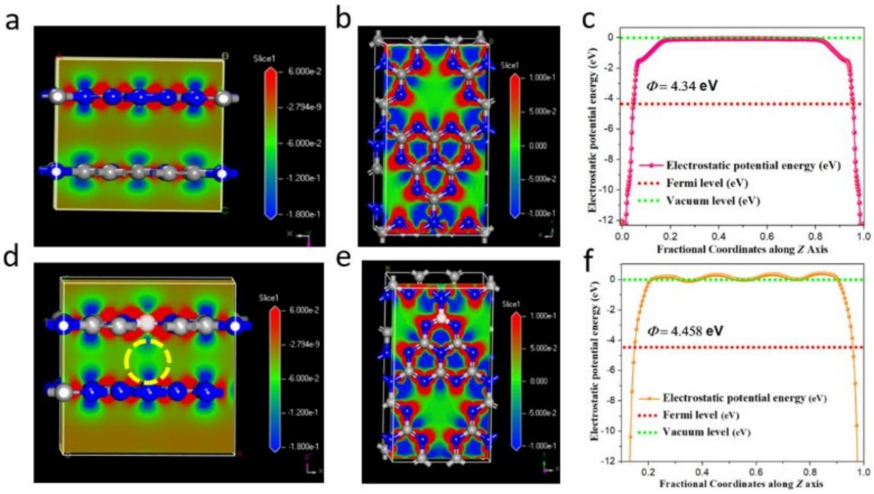

Fig. 3. (a and b) Electron density difference (EDD) plots and (c) work function of bulk-CN; (d and e) EDD plots and (f) Work function of 2D-B-CN (C, N and B atoms are labelled in gray, blue and white, respectively).

of charge carriers and favoring photocatalytic activity.[15,16]

In the above discussion, DFT calculations were carried out to establish the electronic structure evolution of g-C_3N_4 upon B doping. Moreover, Electron density difference (EDD) plots are implemented to understand the distribution of electron density in the system upon B doping,[44-46] which can provide further information to explain how B doping influences the photocatalytic process. Here, the shift towards red indicates electron density enrichment and the shift towards blue implies electron density depletion. Compared with EDD plots of bulk-CN (Fig. 3a and b), it is obvious that an enrichment of electron density has occurred at the B site of 2D-B-CN-X (X = 2, 4, 6 and 8) due to the high polarization by B in +3 state and enhanced hybridization with the N atoms (Fig. 3d and e). B doping also leads to a reduction in the interlayer distance in g-C_3N_4 as observed by XRD (Fig. S2a and b). This is due to a considerable interaction between the B atoms in the top layer and N atoms in the bottom layer (Fig. 3d, yellow circle), which act as a charge transfer pathway by increased overall hybridization and thus accelerate the overall photocatalytic process. Work function for 2D-B-CN-X ($X = 2$, 4, 6 and 8) (Fig. 3f) was found to be higher than that of the bulk-CN (Fig. 3c). This indicates a higher degree of band bending at the photocatalyst interface, resulting in increased charge injection to the reactant for 2D-B-CN and accelerating photocatalytic reaction.[47] The EDD and Work function results suggest that B doping leads to the fast electrons transfer in the layers of g-C_3N_4 and promotes charge injection to the reactants, which are profitable for the enhanced photocatalytic ability.

3.3. Photocurrent, charge carrier separation and charge transfer efficiency

Transient photocurrent test (*i-t* curves) was carried out to confirm the transfer efficiency of photo-induced carriers in the photocatalysts.[48-52] In Fig. 4(a), stable photocurrent for prolonged period indicates the outstanding photoresponse and chemical stability of all the samples. The low photocurrents for 2D-B-CN-0 and bulk-CN without B doping can be attributed to very limited visible light absorption of g-C_3N_4. When B atoms are introduced, the transient photocurrents are significantly enhanced due to the dramatically improved visible light absorption and the effective charge separation and transfer in 2D-B-CN-X ($X = 2$, 4, 6 and 8) nanoplatelets.[39,40] Although the photocurrent of bulk-B-CN-4 is higher than that of bulk-CN and 2D-CN-0 owing to the B doping, it is significantly lower than those of the exfoliated 2D-B-CN-X ($X = 2$, 4, 6 and 8) samples. We found that 2D-B-CN-4 gives the highest photocurrent response. PL spectra of the samples in Fig. 4(b) exhibit a peak at ~460 nm, consistent with the intrinsic band gap absorption of g-C_3N_4. The bulk-CN exhibits the strongest PL emission, indicating its high photo-induced electron and hole recombination rate. The reduction in the emission peak intensity for 2D-B-CN-0 nanoplatelets compared with bulk-CN suggests that the photoinduced carrier recombination is relatively restricted due to the hierarchical 2D nanoplatelet structure. With increasing B doping amount, the emission intensity significantly decreases. The weakest PL intensity observed for 2D-B-CN-4 indicates that it is the best among the studied samples for photoinduced carrier separation. We propose that the increase in emission intensity for 2D-B-CN-8 is due to excessive B doping and large number of active sites, which unfortunately favors carrier recombination. The control of B doping amount is thus essential to achieve an optimized photoinduced carrier separation efficiency. In addition, the photogenerated charge-carrier lifetimes of the samples were obtained from the time-resolved PL spectra (Fig. S7). The average emission lifetimes of

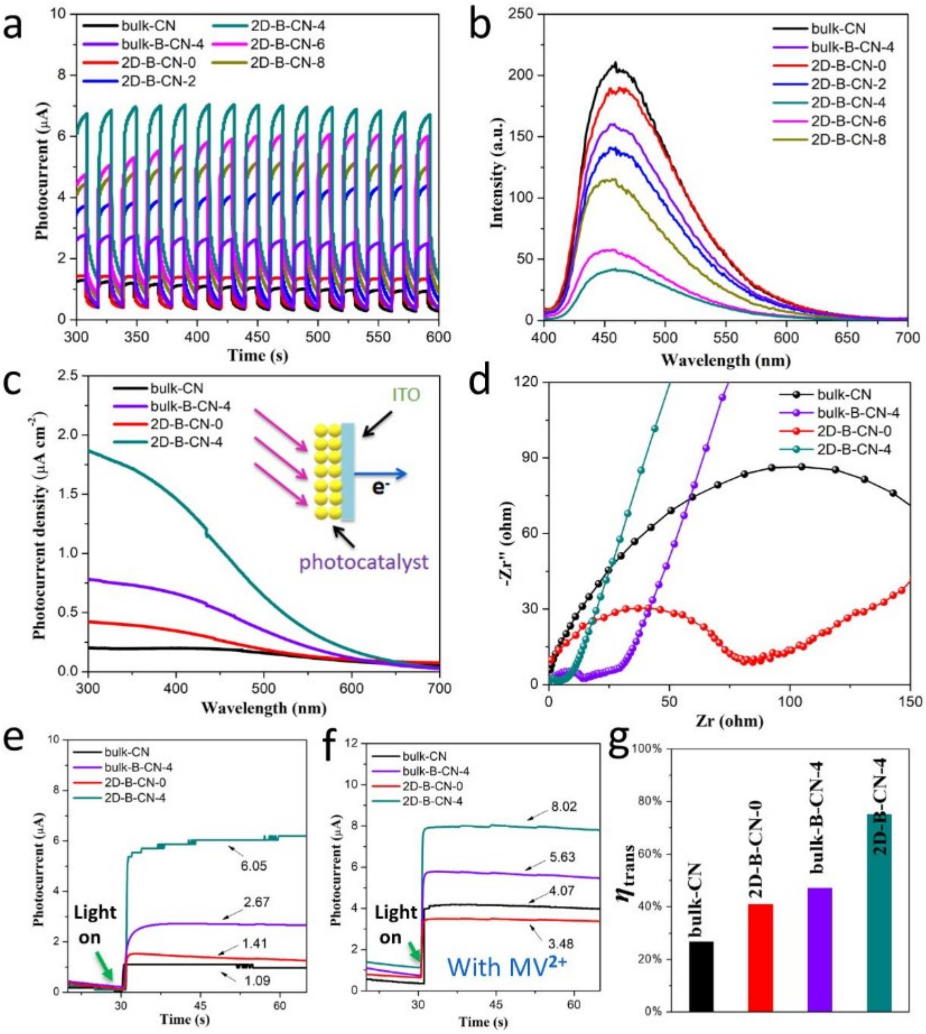

Fig. 4. (a) Transient photocurrent response curves and (b) photoluminescence spectra of the as-prepared samples. (c) Photocurrent response versus different monochromatic light and (d) electrochemical impedance spectroscopy (EIS) spectra (Nyquist plots) of bulk-CN, bulk-B-CN-4, 2D-B-CN-0 and 2D-B-CN-4. Photocurrent density of bulk-CN bulk-B-CN-4, 2D-B-CN-0 and 2D-B-CN-4 under visible light irradiation (e) without and (f) with $MVCl_2$. (g) The η_{trans} of the four samples.

bulk-CN, 2D-B-CN-0, bulk-B-CN-4 and 2D-B-CN-4 were 2.8, 3.1, 4.7 and 5.5 ns, respectively, further suggesting superior charge carrier separation in 2D-B-CN-4 [9,19,30]. The photocurrent response of bulk-CN, bulk-B-CN-4, 2D-B-CN-0 and 2D-B-CN-4 under different monochromatic light was also characterized (Fig. 4c). The 2D-B-CN-4 sample shows significantly increased current in both visible and UV ranges, suggesting that the B doping promotes photocurrent intensity and broadens photo-response ranges of g-C_3N_4. The diameters of the Nyquist circle of 2D-B-CN-4 from the EIS measurement tests (Fig. 4d) are much smaller than that of bulk-CN and bulk-B-CN-4, demonstrating that the resistance of charge transfer in 2D-B-CN nanoplatelets are significantly reduced, favoring enhanced photocatalytic efficiency [14,28]. Among the samples, 2D-B-CN-4 exhibits the lowest resistance, indicating its optimal charge transfer ability. The Nyquist circle diameter of bulk-B-CN-4 is smaller than that of bulk-CN and 2D-B-CN-0, suggesting the positive effects of B doping. These results are consistent with the UV-vis diffuse reflectance spectroscopy, DFT calculations, photocurrents and PL observations.

The photocatalytic rate is determined by the combined effect of optical absorption (η_{abs}), charge carrier separation (η_{sep}) and surface charge transfer efficiency (η_{trans}).[23,46] For a photocatalyst, η_{trans} is the most important factor. Herein, with methylviologen dichloride ($MVCl_2$) as a fast electron scavenger, we study the η_{trans} of the as-prepared samples through an elaborately designed photocurrent response test (See Experimental section). As shown in Fig. 4(e), the 2D-B-CN-4 exhibits a photocurrent density of 6.05 μA in Na_2SO_4 electrolyte, being 5.6, 4.3 and 2.3 times higher than that of bulk-CN (1.09), 2D-B-CN-0 (1.41) and bulk-B-CN-4 (2.67), respectively. Fig. 4(f) shows that the photocurrent density promotes to 8.02 μA in the presence of MV^{2+} for 2D-B-CN-4, being 2.0, 2.3 and 1.4 times higher than that of bulk-CN (4.07 μA), 2D-B-CN-0 (3.48) and bulk-B-CN-4 (5.63). From the above, the η_{trans} of 2D-B-CN-4 in Na_2SO_4 electrolyte was thus determined to be 75.4% (Fig. 4g). This is 2.81, 1.86 and 1.59 times higher than that of bulk-CN (26.8%), 2D-B-CN-0 (40.5%) and bulk-B-CN-4 (47.4%). The 2D-B-CN-4 thus possesses a much faster injection efficiency of photoinduced charge carriers into the photo-reaction system and a much higher photocurrent density.

It is clear that B doping can significantly improve the visible light absorption, promote the photogenerated charge carrier separation and charge transfer and injection efficiency of the photoinduced charge carriers. The highly improved hydrophilic character owing to our innovative ultrasonic oxidative exfoliation process can guarantee the full exploitation of all these advanced properties in an aqueous reaction medium. The synergistic effect of B doping and hydrophilic character, in addition to the increased specific surface area and improved hierarchical porous systems endow our B doped g-C_3N_4 nanoplatelets excellent performance in photocatalytic and photoelectrochemical applications.

3.4. Photocatalytic H_2O_2 production and PEC water splitting

The photocatalytic production of H_2O_2 by the as-prepared samples was studied in water under visible light with a saturated O_2 atmosphere (Fig. 5a).[10,23] The bulk-CN sample shows a low H_2O_2 production rate of 1500 μM g^{-1} h^{-1} due to the limited visible light absorption, low specific surface area and poor dispersion in water. The slightly enhanced H_2O_2 production rate for 2D-B-CN-0 sample is attributed to the increased specific surface area, the abundant pore structure and the better dispersion in water. Similarly, the improved photocatalytic H_2O_2 production over 2D-B-CN-4 in comparison to bulk-B-CN-4 can also verify this conclusion. When B atom was introduced into the lattice of g-C_3N_4 nanoplatelets, the H_2O_2 production rate was significantly increased, suggesting the positive role of B doping for photocatalytic reaction. Although the bulk-B-CN-4 has a H_2O_2 photocatalytic production rate higher than that of bulk-CN, 2D-B-CN-0, it is still lower than that of 2D-B-CN-4 due to its poor dispersion in water. Hydrophilicity is thus essential for the improved photocatalytic activity The H_2O_2 photocatalytic production activity of 2D-B-CN-X ($X = 2$, 4, 6 and 8) was largely enhanced, suggesting that all the above-mentioned benefits owing to B doping can be fully exploited in aqueous environment for photocatalytic process. For the ideal 2D-B-CN-4 sample involving the merits of optimal B doping concentration and hydrophilic character, the highest H_2O_2 production rate of 4240.3 μM g^{-1} h^{-1} is achieved on this photocatalyst. This is 2.84, 2.64 and 2.13 times higher than that of bulk-CN, 2D-B-CN-0 and bulk-B-CN-4 samples, respectively (Fig. 5b), further highlighting the importance of the synergy between B doping and hydrophilic character for enhanced photocatalytic activity. When B doping ratio is, however, more than 4%,

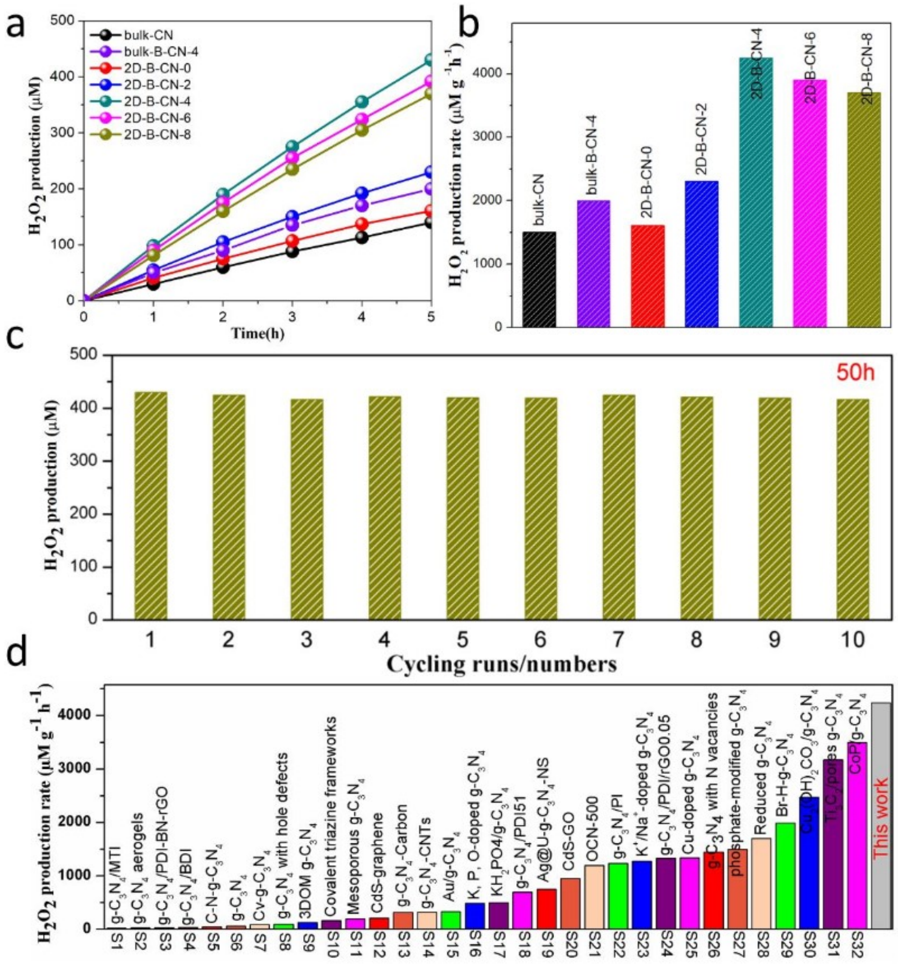

Fig. 5. (a) The photocatalytic generation of H_2O_2 under visible light irradiation (b) H_2O_2 production rates of the as-prepared photocatalysts. (c) The cycle photocatalytic H_2O_2 production test by 2D-B-CN-4 sample (d) H_2O_2 production rate for 2D-B-CN-4 in comparison with other C_3N_4-based photocatalysts.

the H_2O_2 production rate is reduced. This is ascribed to higher photogenerated carrier recombination (Fig. 4b), indicating again that too high B doping may induce too large number of active sites, which ultimately favors carrier combination. The modulation of B doping amount therefore is essential. The cyclic photocatalytic H_2O_2 production experiment over 2D-B-CN-4 shows no change in 10 consecutive cycles for over 50 h (Fig. 5c), indicating its excellent long term stability and potential for practical applications. H_2O_2 production rate normalized vs. mass or surface area for 2D-B-CN-4 in comparison with other C_3N_4-based photocatalysts is presented in Fig. 5(d) and Table S4. It is shown that our 2D-B-CN-4

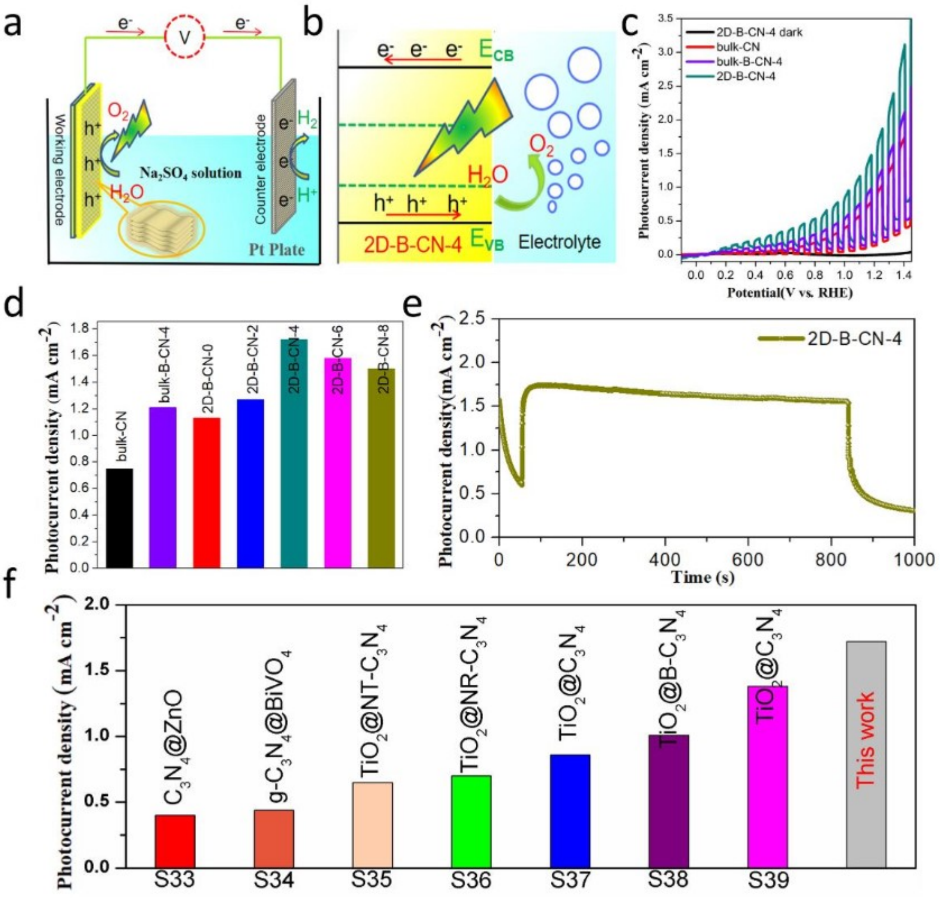

Fig. 6. (a) Schematic diagram illustrating the working mechanism of 2D-B-CN-4 photoelectrode based PEC water splitting. (b) Energy diagrams for the photoinduced charge transfer based on the 2D-B-CN-4 photoanode. (c) Current-voltage (*I-V*) curves of bulk-CN, bulk-B-CN-4 and 2D-B-CN-4 photoelectrodes under chopped AM 1.5G light in 0.1 M Na_2SO_4 solution. (d) The photocurrent densities of all the prepared sample at 1.23 V versus RHE under AM 1.5G illumination. (e) Time-dependence photocurrent density of 2D-B-CN-4 film. (f) Comparisons of PEC water splitting performance between 2D-B-CN-4 and other C_3N_4-based photoanodes.

photocatalyst gives the best H_2O_2 production performance (normalized vs. mass) compared to all the g-C_3N_4 based photocatalysts reported in the literature, underscoring its great potential for practical industrial photocatalytic H_2O_2 production.

The PEC process has been extensively investigated in renewable energy and environmental fields [8,21,41,49]. Fig. 6(a) depicts the working mechanism of 2D-B-CN-4 based photoelectrode for PEC water splitting. The photogenerated electrons are transferred to a Pt counter electrode for water reduction. Fig. 6(b) shows the energy diagram for the photoinduced charge transfer based on the 2D-B-CN-4 photoanode where O_2 can be generated on photoanode due to the oxidation of H_2O. The unique nanostructure, adjusted electronic band structure and hydrophilic character of 2D-B-CN-4 not only enhances the accessible surface area, but also effectively accelerates the hole transfer to the semiconductor-electrolyte interface, leading to better water oxidation kinetics. The PEC water splitting performances of bulk-CN and 2D-B-CN-4 were studied by the linear sweep current-voltage (LSV) method under alternating ON and OFF conditions for AM 1.5G illumination. This is widely used to study the photocurrent response ability of materials. As shown in Fig. 6(c), the photocurrents of bulk-CN and 2D-B-CN-4 films all swiftly rise when the light is ON and drop when the light is OFF over a potential range between -0.1 and 1.5 V vs. RHE. The 2D-B-CN-4 film exhibits a negligible current intensity under dark, indicating that the photocurrent is generated under visible light irradiation only. The photocurrent of the 2D-B-CN-4 is promoted in the present potential range, demonstrating that the 2D-B-CN-4 is an n-type semiconductor [8].

The photocurrent density of all the prepared samples at 1.23 V versus RHE under AM 1.5G illumination are presented in Fig. 6(d). The photocurrent density of bulk-CN is about 0.75 mA cm^{-2} while 2D-B-CN-4 film shows a significantly increased photocurrent density of 1.72 mA cm^{-2}. This is 2.3, 1.6 and 1.4 folds greater than that of bulk-CN, 2D-B-CN-0 and bulk-B-CN-4 photoanodes, respectively. The comparatively small currents of bulk-CN film are attributed to its slow electron transfer ability, limited visible light absorption and specifically poor dispersion in water.[35,49] Notably, the 2D-B-CN-4 exhibits relatively low currents at the initial low bias voltage range (0–0.8 V vs. RHE), which dramatically increases at higher anodic potentials (>0.8 V vs. RHE). This reveals that sufficient potentials (>0.8 V vs. RHE) are conducive to accelerating the charge transfer on the 2D-B-CN-4 surface and that strong charge recombination still takes place at <0.8 V vs. RHE. Fig. 6(e) presents the stability of the 2D-B-CN-4 catalyst in the PEC process. It shows that the photocurrent density of 2D-B-CN-4 has no obvious change until 800 s and remained at an ideal value of 1.63 mA cm^{-2}, indicating an excellent stability of the photoelectrodes. From above results that it is clearly seen that these hierarchically assembled 2D nanoplatelets show higher current densities than that of bulk-CN, implying that B doping and improved hydrophilic character have significantly positive influence on its PEC performance. The PEC activity follows the same order as photocatalytic H_2O_2 production rate. Among these B doped g-C_3N_4 nanoplatelets, 2D-B-CN-4 exhibits the best PEC activity due to its highest photogenerated electron-hole separation. Compared with the previously reported C_3N_4-based photoanodes in the literature, all the B doped 2D-B-CN samples show better PEC activity and our 2D-B-CN-4 photoanode presents the best performance (Fig. 6f, Table S5), indicating that 2D-B-CN-4 is an excellent candidate for large scale PEC water splitting.

A mechanism for the enhanced photocatalytic performance of 2D-B-CN photocatalysts is proposed (Scheme S2). This present work clearly shows that without excellent hydrophilic character, the advanced properties such as high surface area, hierarchical porous assembly, reduced band gap and improved charge separation efficiency of B doped C_3N_4 can not be fully exploited. The synergistic effects of B doping and hydrophilic character created by the oxidative exfoliation give rise to the best photocatalytic and PEC performance of 2D-B-CN-4 photocatalyst.

4. Conclusions

An innovative and facile method to synthesize hydrophilic bi-functional hierarchically assembled 2D B-doped g-C_3N_4 nanoplatelets was developed. Photocatalytic tests reveal that the 2D-B-CN-4 sample shows an excellent H_2O_2 photocatalytic production rate of 4240.3 μM g^{-1} h^{-1}, 2.84, 2.64 and 2.13 times higher than that of the pristine bulk g-C_3N_4, 2D-B-CN-0 and bulk-B-CN-4, respectively. The B doped nanoplatelets by oxidative exfoliation process generate a significant photocurrent density of 1.72 mA cm^{-1} at 1.23 V versus RHE under AM 1.5 G illumination for PEC water splitting, being about 2.5, 1.6 and 1.4 folds greater than that of pristine bulk-CN, 2D-B-CN-0 and bulk-B-CN-4 photoanodes, respectively. The unprecedented photocatalytic and PEC performance of hierarchically assembled 2D B-doped g-C_3N_4 nanoplatelets is attributed to the synergistic effects of B doping and hydrophilic character, leading to their excellent dispersion in water, effective photoinduced charge transfer, enhanced visible-light absorption, large surface area, easy mass transportation and appropriate positions of CB and VB. The 2D-B-CN-4 photocatalyst presented here gives the best performance in photocatalytic H_2O_2 production and in photoelectrochemical water splitting for H_2 production compared to all the g-C_3N_4 based photocatalysts reported in the literature. Our results provide a new technology to create a stable, metal-free g-C_3N_4 based photocatalyst for highly improved, large-scale photosynthetic production of H_2O_2 and photoelectrocatalyst for green hydrogen production by water splitting.

Acknowledgements

Y. Ding thanks the China Scholarship Council for an oversea Doctorate scholarship (201808310127). This project was financially supported by the National Natural Science Foundation of China (U1663225), the Changjiang Scholar Program of Chinese Ministry of Education (IRT_15R52), the program of Introducing Talents of Discipline to Universities-Plan 111 (B20002) of Ministry of Science and Technology and the Ministry of Education of China and the project "DepollutAir" of Interreg V France-Wallonie-Vlaanderen.

References

1. H. Yu, R. Shi, Y. Zhao, T. Bian, Y. Zhao, C. Zhou, G. Waterhouse, L-Z. Wu, C-H. Tung, T. Zhang, Adv. Mater. 29 (2017) 1605148.

2. G. Liu, P. Niu, C. Sun, S. Smith, Z. Chen, G. Lu, H-M. Cheng, J. Am. Chem. Soc. 132 (2010) 11642–1648.

3. S. Guo, Z. Deng, M. Li, B. Jiang, C. Tian, Q. Pan, H. Fu, Angew. Chem. Int. Ed. 55 (2016) 1830–1834.

4. Y. Kofuji, Y. Isobe, Y. Shiraishi, H. Sakamoto, S. Tanaka, S. Ichikawa, T. Hirai, J. Am. Chem. Soc. 138 (2016) 10019–10025.

5. Y. Shiraishi, S. Kanazawa, Y. Kofuji, H. Sakamoto, S. Ichikawa, S. Tanaka, T. Hirai, Angew. Chem. Int. Ed. 53 (2014) 13454–13459.

6. K. Xiao, P. Giusto, F. Chen, R. Chen, T. Heil, S. Cao, L. Chen, F. Fan, L. Jiang, Natl. Sci. Rev. 8 (2020) nwaa231.

7. D. Su, Natl. Sci. Rev. 2 (2015) 138–139.

8. Y. Yang, S. Wang, Y. Jiao, Z. Wang, M. Xiao, A. Du, Y. Li, J. Wang, L. Wang, Adv. Funct. Mater. 28 (2018) 1805698.

9. P. Yang, H. Zhuzhang, R. Wang, W. Lin, X. Wang, Angew. Chem. Int. Ed. 58 (2019) 1134–1137.

10. L. Shi, L. Yang, W. Zhou, Y. Liu, L. Yin, X. Hai, H. Song, J. Ye, Small 14 (2018) 1703142.

11. D. Liu, D. Chen, N. Li, Q. Xu, H. Li, J. He, J. Lu, Angew. Chem. Int. Ed. 59 (2020) 4519-24.

12. L. Villalobos, M. T. Vahdat, M. Dakhchoune, Z. Nadizadeh, M. Mensi, E. Oveisi, K. V. Agrawal, Sci. Adv. 6 (2020) eaay9851.

13. S. Tonda, S. Kumar, S. Kandulab, V. Shanker, J. Mater. Chem. A 2 (2014) 6772–6780.

14. D. Zhao, C-L. Dong, B. Wang, C. Chen, Y-C. Huang, Z. Diao, S. Li, L. Guo, S. Shen, Adv. Mater. 31(2019) 1903545.

15. F. Wei, Y. Liu, H. Zhao, X. Ren, J. Liu, T. Hasan, L. Chen, Y. Li, B-L. Su, Nanoscale 10 (2018) 4515–4522.

16. N. Sagara, S. Kamimura, T. Tsubota, T. Ohno, Appl. Catal. B 192 (2016) 193–198.

17. Y. Zhou, L. Zhang, J. Liu, X. Fan, B. Wang, M.Wang, W. Ren, J. Wang, M. Lia, J. Shi, J. Mater. Chem. A 3 (2015) 3862–3687.

18. Z. Wei, M. Liu, Z. Zhang, W. Yao, H. Tan, Y. Zhu, Energy Environ Sci 11 (2018) 2581–2589.

19. L. Zhang, Z. Jin, S. Huang, X. Huang, B. Xu, L. Hu, H. Cui, S. Ruan, Y-J. Zeng, Appl. Catal. B 246 (2019) 61–71.

20. Y. Wei, J. Wan, N. Yang, Y. Yang, Y. Ma, S. Wang, J. Wang, R. Yu, L. Gu, L. Wang, L. Wang, W. Huang, D. Wang, Natl. Sci. Rev. 7 (2020) 1638–1646.

21. T. Butburee, Y. Bai, H. Wang, H. Chen, Z. Wang, G. Liu, J. Zou, P. Khemthong, G. Lu, L. Wang, Adv. Mater. 30 (2018) 1705666.

22. M-H. Sun, J. Zhou, Z-Y. Hu, L-H. Chen, L-Y, Li, Y-D. Wang, Z-K. Xie, S. Turner, G. Tendeloo, T. Hasan, B-L. Su, Matter 3 (2020) 1226–1245.

23. C. Feng, L. Tang, Y. Deng, J. Wang, J. Luo, Y. Liu, X. Ouyang, H. Yang, J. Yu, J. Wang, Adv. Funct. Mater. 30 (2020) 2001922.

24. L. Feng, K-Y. Wang, X-L. Lv, T-H. Yan, H-C. Zhou, Natl. Sci. Rev. 7 (2020) 1743–1758.

25. L. Wu, Y. Li, Z. Fu, B-L. Su, Natl. Sci. Rev. 7 (2020) 1667–1701.

26. B. Lin, G. Yang, L. Wang, Angew. Chem. Int. Ed. 58 (2019) 4587–4591.

27. W. Zhang, Y. Tian, H. He, L. Xu, W. Li, D. Zhao, Natl. Sci. Rev. 7 (2020) 1702–1725.

28. Y. Xiao, G. Tian, W. Li, Y. Xie, B. Jiang, C. Tian, D. Zhao, H. Fu, J. Am. Chem. Soc. 141 (2019) 2508–2515.

29. X. Chen, R. Shi, Q. Chen,Z. Zhang, W. Jiang, Y. Zhu, T. Zhang, Nano Energy 59 (2019) 644–650.

30. H. Gao, R. Cao, S. Zhang, H. Yang, X. Xu, ACS Appl. Mater. Inter. 11 (2018) 2050–2059.

31. S. Zhang, L. Gao, D. Fan, X. Lv, Y. Li, Z. Yan, Chem. Phys. Lett. 672 (2017) 26–30.

32. S. Thaweesak, S. Wang, M. Lyu, M. Xiao, P. Peerakiatkhajohn, L. Wang, Dalton Trans. 46 (2017) 10714–10720.

33. C. Lu, R. Chen, X. Wu, M. Fan, Y. Liu, Z. Le, S. Jiang, S. Song, Appl. Surf. Sci. 360 (2016) 1016–1022.

34. J. Zou, Y. Yu, W. Yan, J. Meng, S. Zhang, J. Wang, J. Mater. Sci. 54 (2019) 6867–6881.

35. X. Wu, X. Wang, F. Wang, H. Yu, Appl. Catal. B 247 (2019) 70–77.

36. Ruolan Zhang, Chao Wang, Hao Chen, Heng Zhao, Jing Liu, Y Li, B-L. Su, Acta. Phys. Chim. Sin. 36 (2020) 1803014.

37. L-H. Chen, Y. Li, B-L. Su, Natl. Sci. Rev. 7 (2020) 1626–1630.

38. H. Ou, X. Chen, L. Lin, Y. Fang, X. Wang, Angew. Chem. Int. Ed. 57 (2018) 8729–8733.

39. J. Ran, T. Ma, G. Gao, X-W Du, S Qiao, Energy Environ. Sci. 8 (2015) 3708–3717.

40. W. Jiang, Q. Ruan, J. Xie, X. Chen, Y. Zhu, J. Tang, Appl. Catal. B 236 (2018) 428–435.

41. Z. Pan, G. Zhang, X. Wang, Angew. Chem. Int. Ed. 58 (2019) 7102–7106.

42. P. Niu, L-C. Yin, Y-Q. Yang, G. Liu,H-M. Cheng, Adv. Mater. 26 (2014) 8046–8052.

43. S. Wu, H-J. Zhao, C-F. Li, J. Liu, W. Dong, H. Zhao, C. Wang, Y. Liu, Z-Y. Hu, L. Chen, Y. Li, B-L. Su, J. Colloid. Interface Sci. 538 (2019) 99–107.

44. X. Dang, R. Yang, Z. Wang, S. Wu, H. Zhao, J. Mater. Chem. A 8 (2020) 22720–22727.

45. E. Medina, B. Pinter, J. Phys. Chem. C 124 (2020) 4223–4234.

46. C. Feng, L. Tang, Y. Deng, J. Wang, Y. Liu, X. Ouyang, J. Yu, J. Wang, Appl. Catal. B 281 (2021) 119539.

47. P. Xia, B. Zhu, B. Cheng, J. Yu, and J. Xu, ACS Sustain. Chem. Eng. 6 (2018) 965–973.

48. X. Zheng, G. Shen, C. Wang, Y. Li, D. Dunphy, T. Hasan, C. Brinker, B-L. Su, Bio-inspired Murray materials for mass transfer and activity, Nat. Commun. 8 (2017) 14921.

49. S. Wang, P. Chen, J-H. Yun, Y. Hu, L. Wang, Angew. Chem. Int. Ed. 56 (2017) 8500–8504.

50. Y. Ding, L. Huang, T. Barakat, B-L. Su, Adv. Mater. Interfaces 8 (2021) 2001879.

51. J-X. Yang, W-B. Yu, C-F. Li, W-D. Dong, L-Q. Jiang, Z-P. Zhuang, J. Liu, Z-Y. Hu, H. Zhao, Y. Li, L. Chen, J. Hu, B-L. Su, Chem. Eng. J. 420 (2021) 129695.

52. H. Zhao, C-F. Li, L-Y. Liu, B. Palma, Z-Y. Hu, S. Renneckar, S. Larter, Y. Li, M. Kibria, Ji. Hu, B-L. Su, J. Colloid. Interface Sci. 585 (2021) 694–704.

Graphical Abstract

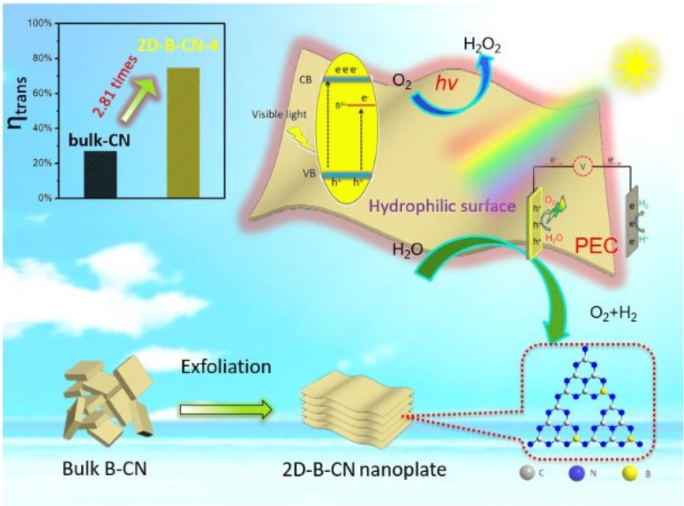

Outstanding performance in photocatalytic H_2O_2 production and PEC water splitting were achieved on the as-prepared two dimensional hydrophilic bi-functional B-doped g-C_3N_4 photocatalyst.

Supplementary Information

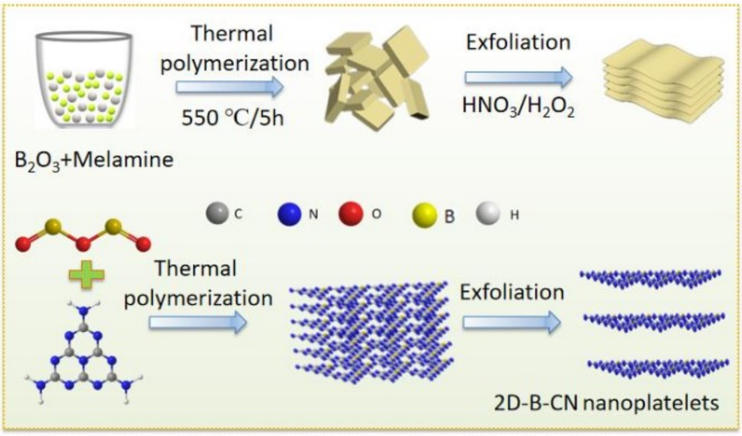

Scheme S1. Schematic synthesis process of the hydrophilic hierarchical B doped g-C_3N_4 nanoplatelets.

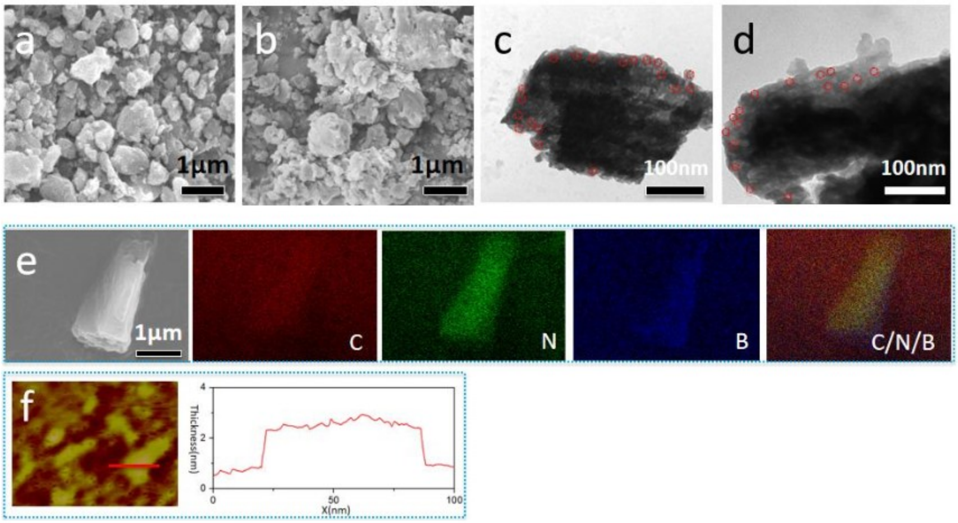

Fig. S1. SEM images of the as-synthesized bulk-CN (a) and bulk-B-CN-4 (b). TEM images of the as-synthesized bulk-CN (c) and bulk-B-CN-4 (d). (e) The elements mapping patterns of 2D-B-CN-4 nanoplatelets. (f) AFM image and cross-section analysis of 2D-B-CN-4 nanoplatelets.

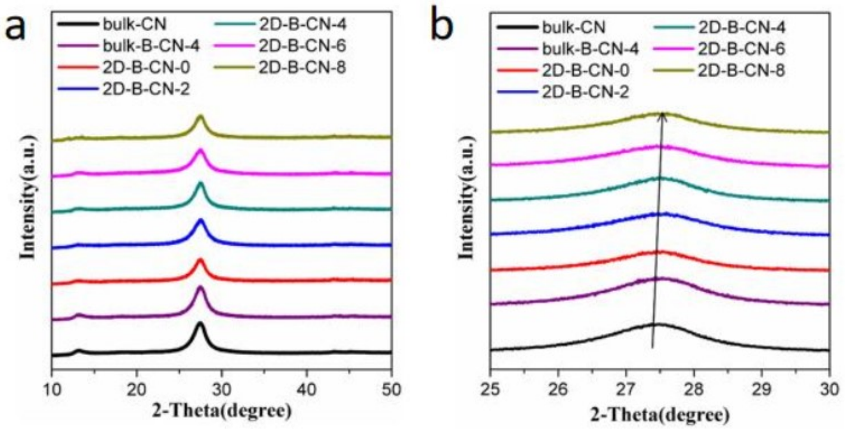

Fig. S2. (a) X-ray diffraction patterns of the as-synthesized samples and (b) the enlarged area of XRD patterns from 25 to 30°.

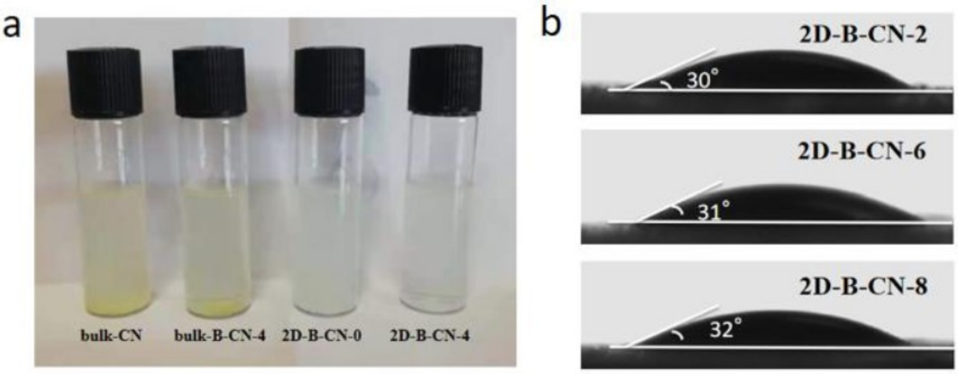

Fig. S3. (a) Photograph for the aqueous dispersion of as-prepared samples left undisturbed for 3 days. (b) Images of water droplets on the 2D-B-CN-2, 2D-B-CN-6 and 2D-B-CN-8 thin films.

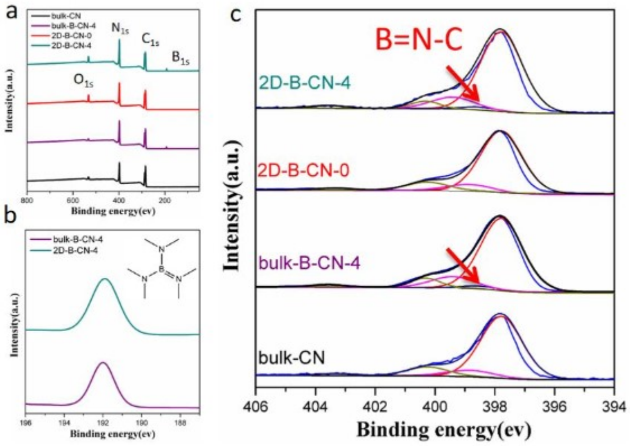

Fig. S4. (a) XPS spectra of bulk-CN, bulk-B-CN-4, 2D-B-CN-0 and 2D-B-CN-4 samples. (b) High-resolution B 1s spectra of bulk-B-CN-4 and 2D-B-CN-4. (c) The enlarged picture of Fig. 1i.

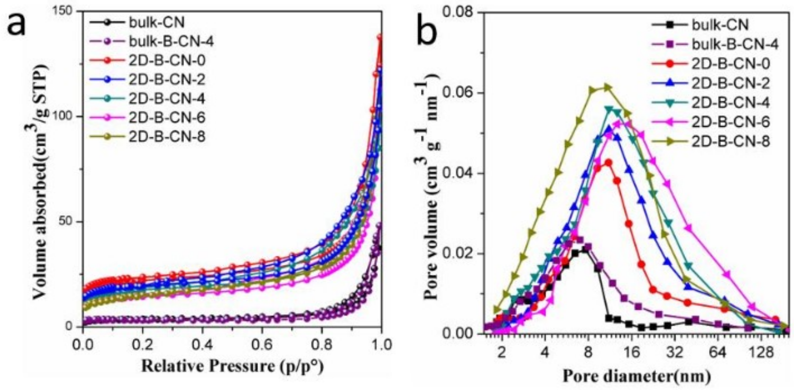

Fig. S5. (a) N_2 adsorption–desorption isotherms and (b) pore size distributions of the as-synthesized samples.

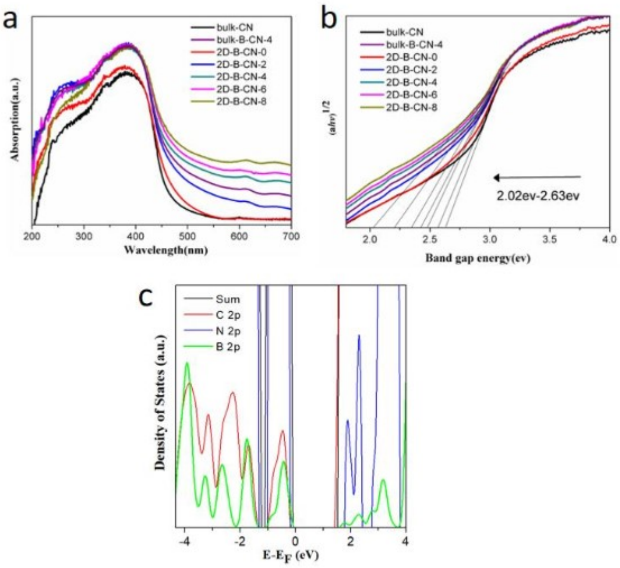

Fig. S6. (a) UV-vis diffuse reflectance spectra and (b) Tauc Plots of the as-prepared samples. (c) The magnified DOS plot of B doped C_3N_4.

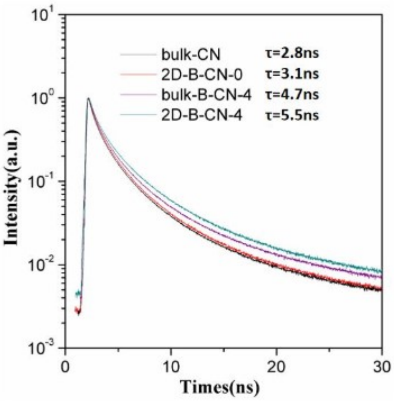

Fig. S7. Time-resolved PL spectra of bulk-CN, bulk-B-CN-4, 2D-B-CN-0 and 2D-B-CN-4 samples (λex = 405 nm).

The time-resolved PL decay curves were fitted with the following eq 1:[9,19,30]

$$\mathrm{fit} = A + B1\exp[-t/\tau 1] + B2\exp[-t/\tau 2]\ (1)$$

where A, B1, and B2 are constants obtained after fitting the corresponding PL decay curve. From this equation, a fast (τ1) and a slow (τ2) decay component was obtained. These data were then fed into eq 2 to calculate the intensity average lifetime (τ) for overall comparison of the lifetimes[30].

$$\tau = [B1\tau 1^2 + B2\tau 2^2]/[B1\tau 1 + B2\tau 1]\ \ (2)$$

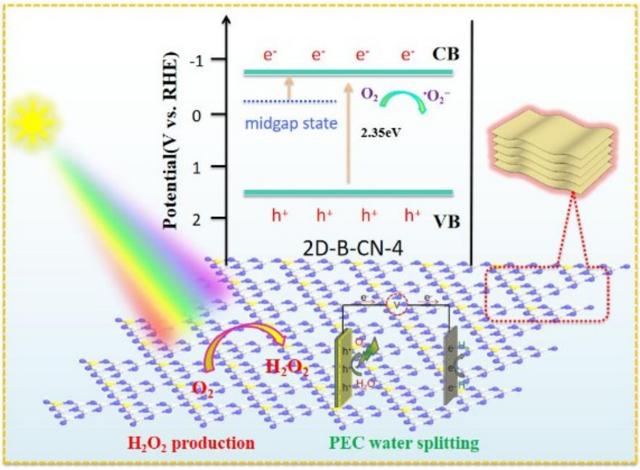

Scheme S2. The mechanism of the enhanced photocatalytic performance for 2D-B-CN-4 photocatalyst under visible light irradiation.

Mechanism for improved photocatalytic and PEC performances

We propose a plausible mechanism for the enhanced photocatalytic performance of 2D-B-CN-4 photocatalyst. As shown in **Scheme S2**, given the synergistic effects of boron doping and hydrophilic surface properties, the remarkable enhancement in photocatalytic H_2O_2 production activity and PEC water splitting performance of 2D-B-CN-4 can be interpreted as follows: (1) The hydrophilic surface of nanoplatelets favors the complete contact of photocatalyst with water and its full dispersion in aqueous solution promotes water adsorption and proton reduction reaction for PEC water splitting process; (2) hierarchical assembly, the very high surface area and abundant pores made by ultrathin nanoplatelets can provide more exposed active catalytic sites for surface reactions and facilitate mass transportation, respectively, accelerating the reaction rate; (3) tunable band structure of g-C_3N_4 induced by B doping allows extension of its visible light absorption range and provides the sufficient driving force for photoredox reaction; (4) ultrathin nanoplatelets can reduce the charge migration route, leading to fast photoinduced carrier separation. The synergistic effects give rise to the best photocatalytic and PEC performance of 2D-B-CN-4 photocatalyst.

Table S1. Description of studied samples

Sample name	**Abbreviation**	**Sample Type**	**Preparation method**	**B % (molar ratio)**
Bulky g-C_3N_4	bulk-CN	reference	solid state reaction	0
Bulky B doped g-C_3N_4	bulk-B-CN-4	reference	solid state reaction	4
Hierarchically assembled g-C_3N_4 nanoplatelets	2D-B-CN-0	reference	solid state reaction + exfoliation	0
Hierarchically assembled B doped g-C_3N_4 nanoplatelets	2D-B-CN-2	targeted sample	solid state reaction + exfoliation	2
	2D-B-CN-4	targeted sample	solid state reaction	4

		+ exfoliation	
2D-B-CN-6	targeted sample	solid state reaction + exfoliation	6
2D-B-CN-8	targeted sample	solid state reaction + exfoliation	8

Table S2. The peaks intensity ratio between C(2) and C(1) for the as-prepared samples.

Sample	**Peak C (1)**	**Peak C (2)**	**C (2)/C (1)**
bulk-CN	190.7	162.2	0.85
bulk-B-CN-4	187.8	154.3	0.82
2D-B-CN-0	192.3	163.3	0.85
2D-B-CN-4	188.9	153.1	0.81

Table S3. The BET surface area, average pore diameter, pore volume of and band gap of the prepared photocatalysts.

Samples	**S_{BET} m^2 g^{-1}**	**Pore size/nm**	**Pore volume cm^3 g^{-1}**	**Band gap/eV**
bulk-CN	12.2	8.2	0.073	2.63
bulk-B-CN-	13.3	7.5	0.086	2.42
2D-B-CN-0	105.7	11.3	0.463	2.58
2D-B-CN-2	104.3	11.7	0.451	2.50
2D-B-CN-4	103.6	12.1	0.447	2.35
2D-B-CN-6	99.5	12.8	0.435	2.25

2D-B-CN-8	98.8	11.5	0.432	2.02

Table S4. H_2O_2 production rate for 2D-B-CN-4 in comparison with other C_3N_4-based photocatalysts.

Photocatalysts	**Conditions**	**H_2O_2 production(vs mass)**	**H_2O_2 production(vs surface area)**	**Ref.**
2D-B-CN-4	Isopropanol+water, O_2, 20 mg, λ≥400 nm, 120 W	4240.3 μM g^{-1} h^{-1}	40.9 μM m^{-2} h^{-1}	This work
g-C_3N_4/MTI	Water, O_2, λ>420 nm	22.9 μM g^{-1} h^{-1}	N/A	S1
g-C_3N_4 aerogels	Water, O_2, λ>420 nm, 300 W	28.8 μM g^{-1} h^{-1}	0.22 μM m^{-2} h^{-1}	S2
g-C_3N_4/PDI-BN-rGO	water, O_2, λ>420 nm, 2000 W	30.8 μM g^{-1} h^{-1}	N/A	S3
g-C_3N_4/BDI	Water, O_2, λ>420 nm	34.2 μM g^{-1} h^{-1}	N/A	S4
C-N-g-C_3N_4	Water, O_2, λ>420 nm	50.5 μM g^{-1} h^{-1}	0.65 μM m^{-2} h^{-1}	S5
g-C_3N_4	Alcohol+water, O_2, λ>420 nm, 2000 W	62.5 μM g^{-1} h^{-1}	N/A	S6
Cv-g-C_3N_4	O_2, λ≥420nm 300W	90 μM μM g^{-1} h^{-1}	9.6 μM m^{-2} h^{-1}	S7
g-C_3N_4 with hole defects	2-propanol+water, λ>420 nm	96.8 μM g^{-1} h^{-1}	2.32 μM m^{-2} h^{-1}	S8
3DOM g-C_3N_4	Pure water, O_2, λ≥320nm 300W	130 μM g^{-1} h^{-1}	1.71 μM m^{-2} h^{-1}	S9

Covalent triazine frameworks	Pure water, O_2, $\lambda \geq 420$ nm, 44.5 mW cm^{-2}	166.7 $\mu M\ g^{-1}\ h^{-1}$	4.89 $\mu M\ m^{-2}\ h^{-1}$	S10
Mesoporous $g\text{-}C_3N_4$	Ethanol+water, O_2, λ = 420-500nm 26.9 W	200 $\mu M\ g^{-1}\ h^{-1}$	0.88 $\mu M\ m^{-2}\ h^{-1}$	S11
CdS-graphene	Methanol+water, O_2, 50 mg, AM1.5G	213.3 $\mu M\ g^{-1}\ h^{-1}$	N/A	S12
$g\text{-}C_3N_4$-Carbon	Isopropanol+water, O_2, 50 mg, UV-vis	317.75 $\mu M\ g^{-1}\ h^{-1}$	N/A	S13
$g\text{-}C_3N_4$-CNTs	Formic acid+water, O_2, 100 mg, $\lambda \geq 400$nm, 300 W	326 $\mu M\ g^{-1}\ h^{-1}$	5.37 $\mu M\ m^{-2}\ h^{-1}$	S14
Au/$g\text{-}C_3N_4$	Ethanol+water, O_2, 30 mg, $\lambda \geq 420$nm, 300 W	330 $\mu M\ g^{-1}\ h^{-1}$	N/A	S15
K, P, O-doped $g\text{-}C_3N_4$	Ethanol+ water, $\lambda \geq 420$nm	485.7 $\mu M\ g^{-1}\ h^{-1}$	N/A	S16
KH_2PO_4/$g\text{-}C_3N_4$	Ethanol+water, O_2, 50 mg, $\lambda \geq 420$nm, 300 W	500 $\mu M\ g^{-1}\ h^{-1}$	N/A	S17
$g\text{-}C_3N_4$/PDI51	Pure water, O_2, 50 mg, $\lambda \geq 420$ nm, 100w	700 $\mu M\ g^{-1}\ h^{-1}$	14.2 $\mu M\ m^{-2}\ h^{-1}$	S18
Ag@U-$g\text{-}C_3N_4$-NS	HClO+water, 100 mg 300W Xe lamp	750 $\mu M\ g^{-1}\ h^{-1}$	N/A	S19
CdS-GO	Methanol+water, O_2, 0.5 g/L, λ = 635 nm, 23 mW/cm^2	950 $\mu M\ g^{-1}\ h^{-1}$	N/A	S20
OCN-500	Isopropanol+water, O_2, 50 mg, $\lambda \geq 420$	1200 $\mu M\ g^{-1}\ h^{-1}$	38.8 $\mu M\ m^{-2}\ h^{-1}$	S21

	nm,100w			
g-C_3N_4/PI	Water, O_2, 300 W λ>420 nm, 0.560 W/cm^2	1240 μM g^{-1} h^{-1}	N/A	S22
K+/Na+-doped g-C_3N_4	Water, O_2, λ>400 nm, 250 W	1277.8 μM g^{-1} h^{-1}	N/A	S23
g-C_3N_4/PDI/rGO 0.05	2-propanol+water, O_2, 50 mg, 420−500 nm, 43.3 W	1333.3 μM g^{-1} h^{-1}	N/A	S24
Cu-doped g-C_3N_4	Water, O_2, λ>400 nm, 250 W	1340.3 μM g^{-1} h^{-1}	14.6 μM m^{-2} h^{-1}	S25
g-C_3N_4 with N vacancies	Ethanol+water, O_2, λ>400 nm, 250 W	1444.4 μM g^{-1} h^{-1}	136.3 μM m^{-2} h^{-1}	S26
phosphate-modified g-C_3N_4	EDTA+water, O_2, λ>400 nm, 250 W	1500 μM g^{-1} h^{-1}	141.5 μM m^{-2} h^{-1}	S27
Reduced g-C_3N_4	Pure water, O_2, 400 mg, $\lambda \geq$420nm, 300 W	1700 μM g^{-1} h^{-1}	N/A	S28
Br-H-g-C_3N_4	EDTA+water, O_2, λ>400 nm	1990 μM g^{-1} h^{-1}	82.2 μM m^{-2} h^{-1}	S29
$Cu_2(OH)_2CO_3$/g-C_3N_4	Water, O_2, λ>400 nm, 300 W	2472 μM g^{-1} h^{-1}	199.4 μM m^{-2} h^{-1}	S30
Ti_3C_2/pores g-C_3N_4	Isopropanol+water, O_2, 100 mg, $\lambda \geq$420nm, 300 W	3170 μM g^{-1} h^{-1}	53.4 μM m^{-2} h^{-1}	S30
CoP/g-C_3N_4	Ethanol+water, O_2, 20 mg, $\lambda \geq$400nm	3500 μM g^{-1} h^{-1}	N/A	S32

[S1] Y. Kofuji, S. Ohkita, Y. Shiraishi, H. Sakamoto, S. Ichikawa, S. Tanaka, T. Hirai, ACS Sustainable Chem. Eng. 2017, 5, 6478-6485.

[S2]H. Ou, P. Yang, L. Lin, M. Anpo, X. Wang, Angew. Chem. Int. Ed. 2017, 56, 10905-10910

[S3] Y. Kofuji, Y. Isobe, Y. Shiraishi, H. Sakamoto, S. Ichikawa, S. Tanaka, T. Hirai, ChemCatChem 2018, 10, 2070-2077.

[S4]Y. Kofuji, S. Ohkita, Y. Shiraishi, H. Sakamoto, S. Tanaka, S. Ichikawa, T. Hirai, ACS Catal. 2016, 6, 7021-7029.

[S5] Y. Fu, C. a. Liu, M. Zhang, C. Zhu, H. Li, H. Wang, Y. Song, H. Huang, Y. Liu, Z. Kang, Adv. Energy Mater. 2018, 8, 1802525

[S6] Y. Shiraishi, S. Kanazawa, Y. Sugano, D. Tsukamoto, H. Sakamoto, S. Ichikawa, T. Hirai, ACS Catal. 2014, 4, 774-780.

[S7] S. Li, G. Dong, R. Hailili, L. Yang, Y. Li, F. Wang, Y. Zeng, C. Wang, *Appl. Catal. B: Environ.* **2016**, 190, 26.

[S8] L. Shi, L. Yang, W. Zhou, Y. Liu, L. Yin, X. Hai, H. Song, J. Ye, Small 2018, 14, 1703142.

[S9] S. Zhao, X. Zhao, H. Zhang, J. Li and Y. Zhu, *Nano Energy.* **2017**, 35, 405-414.

[S10] L. Chen, L. Wang, Y. Wan, Y. Zhang, Z. Qi, X. Wu, H. Xu, *Adv. Mater.* **2019**, *32*, 1904433.

[S11] Y. Shiraishi, Y. Kofuji, H. Sakamoto, S. Tanaka, S. Ichikawa, T. Hirai, *ACS Catal.* **2015**, 5, 3058-3066.

[S12] S. Thakur, T. Kshetri, N. H. Kim, J. H. Lee, *J. Catal.* **2017**, 345, 78.

[S13] R. Wang, X. Zhang, F. Li, D. Cao, M. Pu, D. Han, J. Yang, X. Xiang, *J. Energy Chem.* **2018**, 27, 343.

[S14] S. Zhao, T. Guo, X. Li, T. Xu, B. Yang, X. Zhao, *Appl. Catal. B: Environ.* **2018**, 224, 725.

[S15] X. Chang, J. Yang, D. Han, B. Zhang, X. Xiang, J. He, *Catalysts* **2018**, 8, 147.

[S16] G.-h. Moon, M. Fujitsuka, S. Kim, T. Majima, X. Wang, W. Choi, *ACS Catal*. **2017**, 7, 2886.

[S17] J. Tian, T. Wu, D. Wang, Y. Pei, M. Qiao, B. Zong, *Catal. Today* **2019**, 330, 171.

[S18] Y. Shiraishi, S. Kanazawa, Y. Kofuji, H. Sakamoto, S. Ichikawa, S. Tanaka, T. Hirai, *Angew. Chem. Int. Ed*. **2014**, 53, 13454-13459.

[S19] J. Cai, J. Huang, S. Wang, J. Iocozzia, Z. Sun, J. Sun, Y. Yang, Y. Lai, Z. Lin, *Adv. Mater*. **2019**, 31, 1806314.

[S20] H. Kim, O. S. Kwon, S. Kim, W. Choi, J. Kim, *Energ. Environ. Sci*. **2016**, 9, 1063-1073.

[S21] Z. Wei, M. Liu, Z. Zhang, W. Yao, H. Tan, Y. Zhu, *Energ. Environ. Sci*. **2018**, 11, 2581-2589.

[S22]L. Yang, G. Dong, D. L. Jacobs, Y. Wang, L. Zang, C. Wang, J. Catal. **2017**, 352, 274-281.

[S23] X. Qu, S. Hu, J. Bai, P. Li, G. Lu, X. Kang, J. Mater. Sci. Technol. **2018**, 34, 1932-1938.

[S24] Y. Kofuji, Y. Isobe, Y. Shiraishi, H. Sakamoto, S. Tanaka, S. Ichikawa and T. Hirai, J. Am. Chem. Soc. **2016**, 138, 10019-10025

[S25] S. Hu, X. Qu, P. Li, F. Wang, Q. Li, L. Song, Y. Zhao, X. Kang, Chem. Eng. J. **2018**, 334, 410-418.

[S26] X. Qu, S. Hu, P. Li, Z. Li, H. Wang, H. Ma, W. Li, Diamond Relat. Mater. **2018**, 86, 159-166.

[S27]J. Bai, Y. Sun, M. Li, L. Yang, J. Li, Diamond Relat. Mater. **2018**, 87, 19.

[S28] Z. Zhu, H. Pan, M. Murugananthan, J. Gong, Y. Zhang, *Appl. Catal. B: Environ*. **2018**, 232, 19.

[S29] C. Zhang, J. Bai, L. Ma, Y. Lv, F. Wang, X. Zhang, X. Yuan, S. Hu, Diamond Relat. Mater. 2018, 87, 215-222.

[S30] Z. Li, N. Xiong, G. Gu, Dalton Trans. 2019, 48, 182-189.

[S31] Y. Yang, Z. Zeng, G. Zeng, D. Huang, R. Xiao, C. Zhang, C. Zhou, W. Xiong, W. Wang, M. Cheng, *Appl. Catal. B: Environ*. **2019**, 258, 117956.

[S32] Y. Peng, L. Wang, Y. Liu, H. Chen, J. Lei and J. Zhang, Eur. *J. Inorg. Chem*. **2017**, 17, 4797- 4802.

Chapter 3

3D hierarchical porous carbon nitride for photocatalytic H_2O_2 generation

In this chapter, we report the visible-light H_2O_2 artificial photosynthesis by digging pro-superoxide radical carbon vacancies in three-dimensional hierarchical porous g-C_3N_4 through a simple hydrolysis-freeze-drying-thermal treatment (HFDT). Owing to the synergy of the optimized structure and electronic characters, the efficient photocatalytic H_2O_2 formation is achieved. Specifically, my contribution for the work is that developing an innovative HFDT strategy to fabricate 3D porous structure with surface atom defects, finishing the materials characterization (XRD, NMR, FT-IR, SEM, TEM, PEC and UV-vis et al.) and the discussion of the experimental results. Moreover, the major achievement for the work is the new HFDT strategy, which is expected to prepare other 3D deficient photocatalyst with high performance.

(This work has been published on **Cell Reports Physical Science 2022, 3, 100874** by Yang Ding et al.)

Achieving unprecedented visible light artificial photosynthesis of H_2O_2 by digging pro-superoxide radical carbon vacancies in 3D hierarchical porous carbon nitride

Yang Ding[1,2], Soumyajit Maitra[3], Daniel Arenas Esteban[4], Sara Bals[4], Henk Vrielinck[5], Tarek Barakat[1,2], Subhasis Roy[3], Gustaaf Van Tendeloo[4], Jing Liu[6], Yu Li[6]*, Alexandru Vlad[7] and Bao-Lian Su[1,2,8,9]*

[1] Laboratory of Inorganic Materials Chemistry (CMI), University of Namur, 61 rue de Bruxelles, B-5000, Namur, Belgium.

[2] Namur Institute of Structured Matter (NISM), University of Namur, 61 rue de Bruxelles, B-5000, Namur, Belgium.

[3] Department of Chemical Engineering, University of Calcutta, 92, APC Road, West Bengal, Kolkata-700009, India.

[4] Electron Microscopy for Materials Science (EMAT), University of Antwerp, Antwerp B-2020, Belgium.

[5] Department of Solid State Sciences, Ghent University, Krijgslaan 281-S1, 9000 Gent, Belgium.

[6] State Key Laboratory of Advanced Technology for Materials Synthesis and Processing, Wuhan University of Technology, 122, Luoshi Road, 430070 Wuhan, Hubei, China.

[7] Institute of Condensed Matter and Nanosciences, Université Catholique de Louvain, Place Louis Pasteur 1/L4.01.02, B-1348 Louvain-la-Neuve, Belgium

[8] Clare Hall, University of Cambridge, United Kingdom, CB2 1EW, UK.

[9] Lead contact

*Correspondence: *yu.li@whut.edu.cn* (Y.L.), *bao-lian.su@unamur.be* (B.-L.S.)

Abstract

Artificial photosynthesis of H_2O_2, an environmentally friendly oxidant and a clean fuel, holds great promises. However, improving its efficiency and stability for industrial implementation remains highly challenging. Here, we report the unprecedented visible light H_2O_2 artificial photosynthesis with extraordinary stability by digging pro-superoxide radical carbon vacancies in three-dimensional hierarchical porous g-C_3N_4 through a simple hydrolysis-freeze-drying-thermal treatment. A significant electronic structure change is revealed upon the implantation of carbon vacancies, broadening visible light absorption and facilitating the photogenerated charge separation. The strong electron affinity of the carbon vacancies promotes superoxide radical ($^{\bullet}O_2^-$) formation, significantly boosting the H_2O_2 photocatalytic production. The developed photocatalyst shows an unprecedented H_2O_2 evolution rate of 6287.5 μM g^{-1} h^{-1} under visible light irradiation with an outstanding long cycling stability, being the best-performing photocatalyst among all reported g-C_3N_4 based systems. Our work provides fundamental insight on highly active and stable photocatalysts with great potential for safe industrial H_2O_2 production.

KEYWORDS

H_2O_2 production, hierarchical porous carbon nitride, freeze-drying, carbon vacancies,
artificial photosynthesis

1. Introduction

As an important chemical reagent, H_2O_2 is widely used for chemical synthesis and environmental remediation. Moreover, H_2O_2 is also considered as a potential clean energy alternative to substitute conventional hydrogen energy due to its comparable energy density.[1-6] Various strategies including electrochemical synthesis, alcohol oxidation and anthraquinone oxidation (AO) process have been developed so far to prepare H_2O_2.[7-10] The most used commercial route is the AO process.[9] However, the high cost, tedious operation, and virulent by-products emission of the AO process leads to important efforts in finding efficient, safe and environmentally friendly alternatives for large scale production of H_2O_2. The electrocatalytic oxygen reduction reaction (ORR) is recognized as a strong candidate, however the vast energy consumption and high risk of explosion due to the mixture of H_2 and O_2 hinder its industrial implementation.[10]

Artificial photosynthesis has been regarded as one of the most promising technologies to overcome the energy and environmental challenges.[11-15] It has been reported that upon solar light irradiation, the photocatalysts can generate photoinduced electrons able to reduce the molecular oxygen, and leading to the formation of hydrogen peroxide.[9] Compared with the electrochemical synthesis and the AO process, the artificial photosynthesis of H_2O_2 exhibits multiple advantages such as low energy consumption and a considerably reduced environmental impact.[16-18] Yamashita's group reported hydrophobic MOFs to promote the H_2O_2 production in a two phase benzyl alcohol/water system,[14] whereas Xu et al. proposed a new two-electron water oxidation pathway using acethylene and diacethylene functional covalent triazine frameworks.[1] Graphitic carbon nitride (g-C_3N_4) has attracted increasing attention in solar energy conversion and shows very promising performances for photocatalytic H_2O_2 production.[19-28] Choi's group reported a heteroatom doping of polymeric carbon nitride for H_2O_2 production enhancement,[7] whereas holey nitrogen defective g-C_3N_4 with abundant exposed active sites presented a higher H_2O_2 production activity as compared to bulk g-C_3N_4.[24] Oxygen-enriched g-C_3N_4,[15] g-C_3N_4/aromatic diimide/graphene nanohybrids[3] and leaf-vein-like g-C_3N_4[27] have been also found to improve the efficiency of the H_2O_2 production by promoting the photoinduced charge carrier separation. A significant enhancement in photocatalytic H_2O_2 output using atomic Sb particles loaded g-C_3N_4 was achieved by promoting two-electron oxygen reduction.[28] Additionally, g-C_3N_4 based photonic crystals have also shown to accelerate the photocatalytic H_2O_2 production by enhancing visible light absorption.[16] However, the efficiency of these H_2O_2 photosynthesis processes and stability of the photocatalysts are still far away from industrial requirements, severely impeding their practical applications and its improvement remains a great scientific and practical challenge.[9]

Here we report the implantation of carbon vacancies in 3D hierarchical porous carbon nitride scaffolds through an innovative hydrolysis-freeze drying-thermal treatment (HFDT) method. The introduction of well-modulated carbon vacancies in the 3D hierarchical porous carbon nitride scaffold leads to an unprecedentedly high H_2O_2 evolution rate of 6287.5 $\mu M\ g^{-1}\ h^{-1}$ under visible light irradiation. This is the highest value attained so far when compared to literature reports, and 4.2 and 1.6 times higher than that of the bulk g-C_3N_4 and g-C_3N_4 nanosheets, respectively. The cycling study of our photocatalysts with a very long cycle of 10 hours shows an outstanding stability up to 100 hours, the best stability and the longest cycle duration compared to the state-of-the-art reports. Fukui Function (FF) and electrostatic potential plots reveal the essential role of carbon vacancies as reaction active sites, with a strong electron affinity and $^{\bullet}O_2^-$ radicals generating ability, all being favorable for the enhanced photocatalytic H_2O_2 generation. The significantly improved photosynthetic H_2O_2

production activity is thus attributed to the generation of a mid-gap electronic level upon the introduction of carbon vacancies, which extends the absorption in the visible-light range, facilitates the photo-induced charge separation,[25-27] and promotes the $^{\bullet}O_2^-$ radicals formation. Moreover, the highly exposed surface of the 3D hierarchical porous structure offers abundant reactive sites and developed porous channels for the fast mass transfer of the reactants and products.[29-35] This innovative freeze-drying process inducing carbon vacancies can be extended for the preparation of highly active carbon defective materials for other photocatalytic applications. Our carbon deficient hierarchical porous g-C_3N_4 consolidates its potential as an highly efficient photocatalyst for the large scale and safe industrial production of H_2O_2.

2. Experimental

2.1 Chemicals

Potassium iodide, potassium chloride, sodium sulfate and Nafion were purchased from Merck and melamine from Aladdin Ltd and used without further purification. Distilled water was used in the whole experiment process.

2.2 Synthesis of 3D-CN-C, bulk g-C_3N_4 and C_3N_4 nanosheets

For the synthesis of an innovative carbon deficient 3D porous g-C_3N_4, a novel hydration-freeze drying-thermal treatment (HFDT) of melamine was developed. In a typical synthesis, 2g of melamine was dissolved in 50 mL of deionized water with stirring for 2 h at 70°C. The obtained solution was filtered to remove the solid residues and the filtrate was naturally let to cool down at room temperature. A white flocculent solid of hydrated melamine was obtained. The liquid nitrogen was used to freeze-dry the flocculent solid. Finally, the freeze-dried product was heated at 520 °C for 4 h in an Ar atmosphere to obtain 3D-CN-C1 sample; whereas 3D-CN-C2 sample was prepared by calcinating the freeze-dried precursor at 550 °C for 4 h in an Ar atmosphere. The schematic preparation process of the 3D-CN-C sample is illustrated in Scheme 1. Bulk g-C_3N_4 (B-CN) was synthesized by direct calcination of melamine powder in a muffle furnace at 550°C for 4h. C_3N_4 nanosheets (NS-CN) were prepared according to the literature.[30]

2.3 Characterizations

X-ray diffraction (XRD) patterns were obtained on a Bruker D8 system with Cu Ka radiation (λ = 0.15405 nm) with a scanning rate of 4°/min and range within 10-50°. The ^{13}C and ^{1}H solid-state MAS NMR measurements were conducted on a Bruker Avance 500 MHz (7 T) spectrometer using 4 mm zirconia rotors as sample holders with a spinning rate of 10 kHz. Elemental analysis (C, H, N) was performed on a Vario EL microanalyzer. Scanning electron microscopy (SEM) observation was carried out using JEOL 7500 F field-emission SEM. Transmission electron microscopy (TEM) images were acquired on polymer coated copper grids by using a TECNAI 10 apparatus. Atomic force microscopy (AFM) imaging was performed on a Park XE70 AFM (Park Systems Corp., Korea). Nitrogen adsorption-desorption isotherms were recorded using an ASAP 2420 surface area & porosity analyzer at 77 K. The specific surface area was calculated by the Brunauer-Emmett-Teller (BET) method. The pore size distribution was calculated by the Barrett-Joyner-Halenda (BJH) method and non-local density functional theory (NLDFT) analysis method. X-ray photoelectron spectroscopy (XPS) analysis was performed on a Thermo Fisher ESCALAB 250 Xi instrument with a monochromatic Al Kα x-ray source (1486.6 eV). The EPR spectra on dry powders were recorded on a Varian E-line spectrometer with a standard rectangular cavity (TE102 mode), a HP 5342A microwave frequency counter, and a Bruker NMR ER 035 M Gaussmeter, using diphenyl picrylhydrazyl (DPPH; g = 2.0036) for field calibration. The static magnetic field was modulated at 10kHz with an amplitude of 1.6 Gauss. To avoid saturation, spectra had to be recorded at low microwave power (60 μW). The electron spin resonance (ESR) signals of free radicals were examined by using 5,5-dimethyl-L-pyrroline N-oxide (DMPO) as a probe on a Bruker ER200-SRC spectrometer under visible light irradiation. The UV-vis absorption spectra were collected by a UV-vis spectrophotometer (Perkin Elmer Lambda 35 UV-visible spectrometer) in the wavelength range of 200-800 nm. Photoluminescence properties of the samples were investigated by Perkin Elmer LS45 luminescence spectrophotometer.

2.4 Photocatalytic H_2O_2 production experiments.

In a typical process, 20 mg of catalyst was dispersed in a mixture of water (19 mL) and isopropanol (1 mL). The solution was bubbled with O_2 for 10 min to saturation. Before the light irradiation, the solution was put in a dark box and magnetically stirred for 30min to reach an adsorption-desorption equilibrium. Afterward, the photocatalytic reaction was carried out under visible light irradiation (400-800 nm) by using 6 neon lamps of 20 W at room temperature for 2h. Finally, 2 mL of solution was taken from the beaker and immediately centrifuged for the separation of photocatalyst for analyses. For the comparative experiments, the solution was bubbled with Ar instead of O_2 for 10 min before measurement. The amount of H_2O_2 was analyzed by conventional iodometry method as reported in literature.**[16]** In brief, 1 mL of 0.1 $mol{\cdot}L^{-1}$ ammonium molybdate tetrahydrate aqueous solution and 1 mL of 0.4 $mol{\cdot}L^{-1}$ potassium iodide (KI) aqueous solution were added to the obtained 2 mL of filtrate, which was then kept for 1 min. The H_2O_2 molecules reacted with iodide anions (I^-) under acidic conditions to produce I_3^- anions, which possess a strong absorption at around 350 nm. The amount of I_3^- was analyzed by the UV-visible spectroscopy test and the amount of H_2O_2 was consequently calculated. The photocatalytic H_2O_2 generation under various monochromatic light illumination were conducted by setting the input of specific wavelength on the computer-controlled electrochemical workstation (CHI 660E) with a xenon arc lamp.**[34,35]**

2.5 Photoelectrochemical measurements

The photoelectrochemical measurements were conducted in a typical three-electrode cell by using computer-controlled electrochemical workstation (CHI 660E).**[34,35]** Typically, 20 mg of catalyst sample was added into a mixed solution of deionized water (100 μL) and Nafion (50 μL). After ultrasonic treatment for 10 min, the prepared homogeneous suspension (50 μL) was uniformly sprayed onto the surface of indium tin oxide (ITO) (1.0×1.0 cm). The ITO glass with photocatalyst served as the working electrode, whereas a Pt plate and a saturated calomel electrode (SCE) were used as the counter and the reference electrode, respectively. 0.1 M Na_2SO_4 solution was used as the electrolyte, and the visible light was supplied by a xenon arc lamp PLS-SXE-300C with a 420 nm cut-off filter. The photocurrent-time (I-t) curves were collected at the open-circuit potential. Electrochemical impedance spectroscopy (EIS) test was carried out in a 0.2 M KCl solution. The collected potentials versus SCE electrode were converted to the reversible hydrogen electrode (RHE) according to the following formula: $E\ (RHE) = 0.242 + 0.059\ pH + E(SCE)$.**[35]**

2.6 Computational details

DFT calculations have been performed using GGA functional with PBE exchange correlation and Ultrasoft type pseudopotentials with Koelling-Hammon relativistic treatment and Gimme parameters to account for DFT-D (vdW) correction. Band structure and DOS calculations were carried out using CASTEP code using a (2x2x2) supercell (Supplementary **Fig**. S16). A Mokhorst Pack Scheme (5 x 5 x 1) K point mesh was taken. Plane wave cut-off was set at 570 eV. SCF cutoff was set at 1E-6 eV. Geometry optimization was carried out prior to DFT calculations with energy cut-off set at 1E^{-7} eV with maximum force set at 0.01 eV /Å. HOMO, LUMO, EDD and Fukui Function calculations were performed using Dmol3 code using a H-terminated nonperiodic C_3N_4 superstructure using B3LYP functional with DND basis set and basis file 3.5. SCF tolerance was set at 1E^{-6} eV and geometry optimization was carried out prior to calculations with energy cut-off set at 1E^{-7} eV with maximum force set at 0.004 eV /Å. Adsorption calculations were carried out using Monte Carlo simulations with Edwald electrostatic attractions using Metropolis method and Atom Based vdW interactions with COMPASS II forcefield in SORPTION Code.

3. Results and Discussion

3.1 Structure, morphology and texture properties

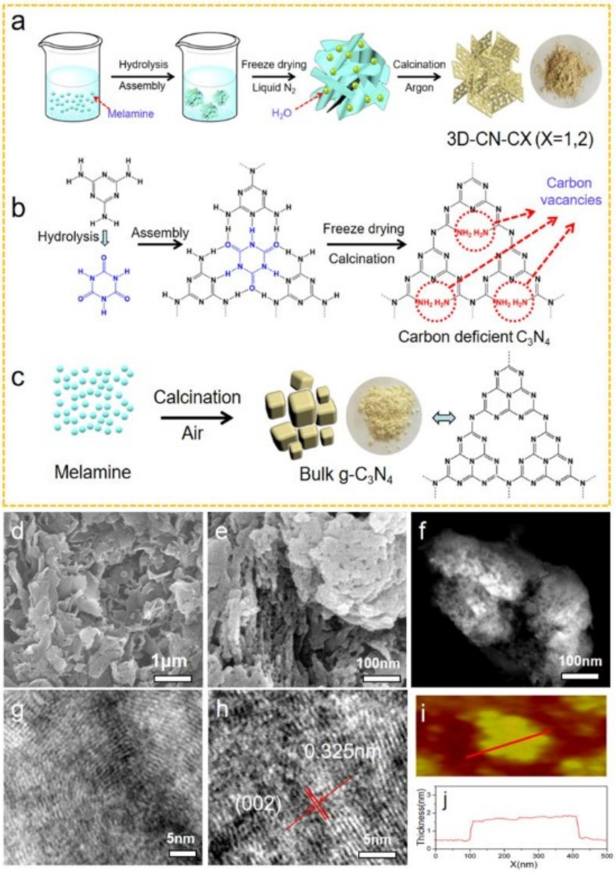

Figure 1. **Schematic preparation process and morphology characterization**

(a, b) Schematic preparation process of the 3D hierarchical porous carbon-deficient C_3N_4 architecture (3D-CN-C), as compared to (c) bulk C_3N_4 (B-CN) synthesis route. (d, e) SEM images and (f) HAADF-TEM image of the 3D-CN-C1 sample, (g) iDPC-STEM image showing a stacked corrugated graphene-like structure, (h) magnified iDPC image showing an interplanar separation similar to the (002) spacing of the layers in the C_3N_4 graphene-like structure (P-6m2). AFM image (i) and cross-section analysis (j) of the 3D-CN-C1 sample.

Figures 1a and 1b depict the fabrication process of the carbon-deficient 3D hierarchical porous C_3N_4 scaffold through an innovative hydrolysis-freeze drying-thermal treatment (HFDT) of melamine. Compared with the traditional preparation route (**Figure** 1c), the innovative HFDT method can simultaneously induce carbon vacancies and create a 3D hierarchical porous structure. For the synthesis, first the melamine powder (**Figure** S1a) was dissolved in water at 70°C, leading to the formation of cyanuric acid upon hydrolysis. Subsequently, cyanuric acid-melamine supramolecular networks are generated through the hydrogen bonding interactions between melamine and cyanuric acid (**Figure** 1b). The resultant white supramolecular polymer precipitate (**Figure** S1b) was freeze-dried in liquid nitrogen to obtain a fluffy flaky material (**Figure** S1c) and then calcined. A three-dimensional hierarchical architecture made of assembled porous g-C_3N_4 nanoplatelets with abundant carbon vacancies is obtained (**Figure** 1a and b). The elimination of residual water molecules attached on the freeze-dried precursor generates carbon vacancies and mesoporosity into the framework of the g-C_3N_4 nanoplatelets upon calcination. Two carbon-deficient 3D hierarchical porous g-C_3N_4 samples (3D-CN-CX, wherein X=1, 2 assigns the calcination temperature, of 520°C and 550°C, respectively) were prepared. Bulk g-C_3N_4 (B-CN) was prepared as reference sample by direct calcination of melamine under air atmosphere (**Figure** 1c, refer to supporting information file for more details).

SEM analysis of the 3D-CN-C1 sample reveals a 3D porous framework which is hierarchically assembled from ultrathin g-C_3N_4 nanoplatelets (**Figure** 1d). The nanoplatelets exhibit a curly shape with characteristic sizes below 1 μm and abundant mesopores in the 5-20 nm range (**Figure** 1e). The 3D-CN-C2 sample presents a similar structure (**Figure** S1d). In contrast, bulk g-C_3N_4 (B-CN) is made of irregular agglomerates of 0.2-2 μm in size (**Figure** S1e, and S1f). The g-C_3N_4 nanosheets (NS-CN) prepared as a reference[30] show a smooth surface, and an average particle size of 1-3 μm (**Figures** S1g and S1h). The HAADF-TEM images of 3D-CN-C1 (**Figures** 1f and S2) confirm the porous nature of the nanoplatelets as observed by SEM. Such 3D hierarchical porous structure is expected to provide more surface reactive sites and facile mass transfer for the surface reaction.**[29,31,34]** Integrated differential phase contrast (iDPC-STEM) enables to obtain images using a very low electron dose (below 600 e/A^2 in this case), ideal for imaging beam sensitive materials such as ultrathin C_3N_4 nanoplatelets at high resolution.**[36]** iDPC-STEM images (**Figures** 1g and 1h) evidence the layered and corrugated structure of carbon defective C_3N_4 nanoplatelets, with a measured d-spacing of 0.325 nm, alike the (002) interplanar distance in pure phase C_3N_4. The atomic force microscopy (AFM) image (**Figure** 1i) indicates a nanoplatelet thickness of about 1.8 nm (**Figure** 1j), corresponding to about 4 g-C_3N_4 layers.**[29]** The XRD patterns of the as-prepared samples are shown in **Figure** S3a. All materials display the characteristic diffraction peaks of g-C_3N_4. For bulk g-C_3N_4 (B-CN), the weak peak at 13.05° and the strong intense peak at 27.62° are attributed to the (100) in-plane structural packing motif and (002) interlayer stacking of aromatic segments, respectively.**[22-24]** The g-C_3N_4 nanosheets (NS-CN) show a very similar XRD pattern to bulk g-C_3N_4 (B-CN). Compared with bulk g-C_3N_4 (B-CN), the (002) diffraction peak in 3D-CN-C1 is shifted from 27.62° to 27.70°, indicating a reduced interlayer distance. The significantly lower peak intensity is attributed to higher disorder (formation of carbon vacancies and mesoporosity) of the nanoplatelets assembled architecture of 3D-CN-C1. The further reduced peak intensity in 3D-CN-C2 is ascribed to the presence of higher amount of carbon vacancies. Solid-state ^{13}C and ^{1}H MAS NMR analyses provide further structural information about 3D-CN-C samples. As shown in **Figure** 2a, the ^{13}C NMR spectra of bulk g-C_3N_4 (B-CN), 3D-CN-C1 and 3D-CN-C2 samples exhibit two strong peaks at 156.2 and 164.3 ppm corresponding to the chemical shifts of C_{3N} (signal 1) and $C_{2N\text{-}NHx}$ (signal 2) in the heptazine units.**[19,21]**

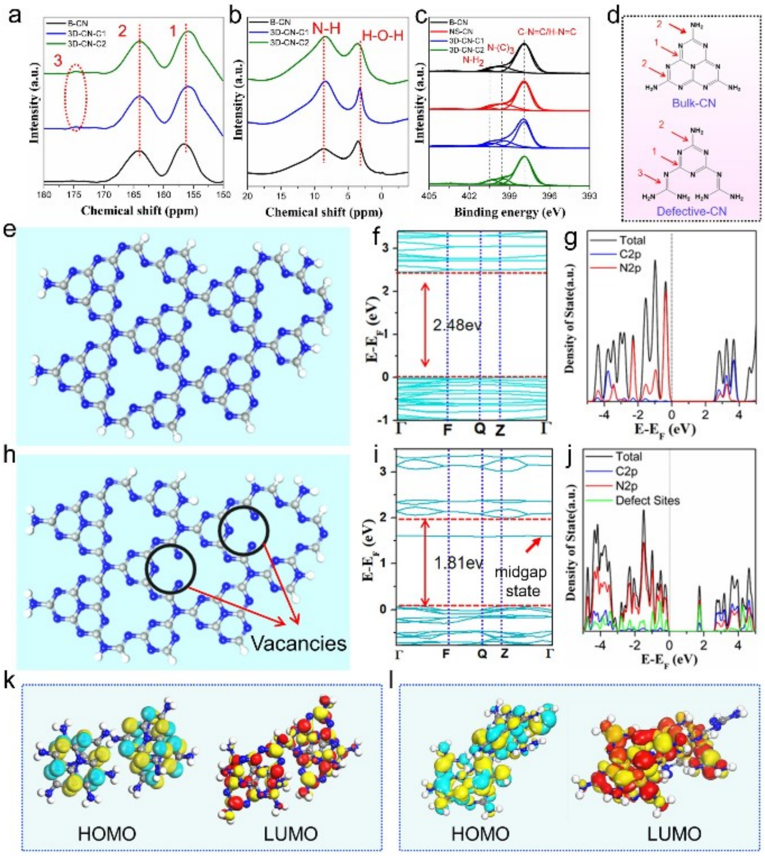

Figure 2 Structural characterizations and DFT calculations

(a) Solid-state ^{13}C and (b) ^{1}H MAS (magic angle spinning) NMR spectra of bulk g-C_3N_4 and 3D-CN-C samples. (c) High-resolution XPS spectra of N1s of the as-prepared samples. (d) Proposed structures of bulk g-C_3N_4 and carbon defective C_3N_4 building units. Detailed structures of (e) bulk-C_3N_4 (B-CN) and (h) carbon defective C_3N_4 (3D-CN-C) frameworks as used for band structure calculations (C and N atoms are labelled in gray and blue, respectively), with the corresponding band gap and PDOS for B-CN (f, g) and 3D-CN-C1 (i, j), respectively. HOMO and LUMO spatial map of B-CN (k) and 3D-CN-C (l) samples.

The new peak at 175.1 ppm for both 3D-CN-C1 and 3D-CN-C2 samples, is attributed to the carbon atoms (signal 3) in the defective heptazine units.[26] The ^{1}H NMR spectra (**Figure** 2b) show two peaks at 3.4 and 8.5 ppm, which correspond to the chemical shifts of adsorbed water and NH_x in the heptazine units, respectively.[19] Compared with bulk g-C_3N_4 (B-CN), the stronger peaks at 8.5 ppm from both 3D-CN-C1 and 3D-CN-C2 indicate the presence of more NH_x groups in these two samples. To further clarify the origin of H atoms of the NH_x group in the defective heptazine units, a ^2H (D) isotope labeling experiment was conducted. The synthesis process was similar to the preparation of 3D-CN-C1 except that H_2O was replaced by D_2O. The obtained sample, labeled as D-3D-CN-C1, was also analyzed by solid-state ^1H MAS NMR spectroscopy. The highly similar ^1H MAS NMR spectra between 3D-CN-C1 and D-3D-CN-C1 (**Figure** S4) indicate that H atoms comprising the carbon defective heptazine units originate from the melamine precursor rather than from D_2O. The Fourier transform infrared (FT-IR) spectra are shown in **Figure** S3b. For all the samples, the broad peaks between 3000 and 3400 cm^{-1} belong to the N-H stretching vibration and the O-H band. The peaks in the 1100-1700 cm^{-1} region are attributed to sp^2 C=N stretching vibration modes and the aromatic sp^3 C-N bonds while the intense peak at 810 cm^{-1} corresponds to the signature of the formation of tri-s-triazine.[15,20] The N-H stretching vibration in 3D-CN-C is much stronger than that of bulk g-C_3N_4 (B-CN) and g-C_3N_4 nanosheets (NS-CN), suggesting that the formation of carbon vacancies breaks the N-C=N/H-C=N groups and more N-H bonds are generated.[24] These results are in good agreement with the NMR observations.

The C/N ratio and chemical bonding nature were further analyzed with XPS and elemental analysis (**Figure** 2c, **Figure** S5, and **Table** S1). The surface C/N atomic ratio decreases from 0.76-0.78 for bulk g-C_3N_4 (B-CN) and g-C_3N_4 nanosheets (NS-CN) to 0.70 and 0.65 for 3D-CN-C1 and 3D-CN-C2, respectively. This further confirms that the carbon vacancies are generated in the 3D-CN-C samples and that a higher calcination temperature leads to more carbon vacancies. From the elemental analysis (**Table** S1), the carbon vacancy percentage for 3D-CN-C1 and 3D-CN-C2 is calculated to be around 10 and 15%, respectively. To further verify the formation of carbon vacancies in the samples, high-resolution XPS spectra of C 1s and N 1s of all the samples were acquired and analyzed. As shown in **Figure** S5b, the peaks at 284.1 and 287.5 eV are attributed to C-C bonds and C-N_3 bonds, respectively,[15,16] whereas the peaks at 397.9, 399.6 and 400.4 eV in the high-resolution N 1s spectra (**Figure** 2c) belong to C-N=C/H-N=C, N-$(C)_3$, and C-NH_2, respectively.[23-25] **Table** S1 summarizes the relative ratios of C-N=C/H-N=C, N-$(C)_3$ and C-NH_2 calculated from the N 1s spectra. Compared with bulk g-C_3N_4 (B-CN), the peak area ratios of N-$(C)_3$ in 3D-CN-C1 and 3D-CN-C2 samples obviously reduced, suggesting that the loss of carbon has its origins from the N-$(C)_3$ sites. The enhanced peak area ratio of N-H_2 in both deficient samples illustrates that the N-$(C)_3$ has been selectively converted into N-H_2 groups. The removal of tertiary carbon leads to the formation of N-H bonds, this mechanism being in good agreement with the NMR, FT-IR and XPS analysis. Based on this physico-chemical rationale, a structure for bulk g-C_3N_4 (B-CN) and carbon defective 3D hierarchical porous g-C_3N_4 (3D-CN-C) is proposed (**Figure** 2d). Electron paramagnetic resonance (EPR) measurements in dark of all the samples (**Figure** S6) show a single narrow line (~ 5 Gauss) at $g \approx 2.003$. Such signal has been estimated to the paramagnetic centers related to electrons delocalized in the conduction band[26] or carbon-centered radicals.[24] The concentration of paramagnetic centers in these samples is calculated to be very low in the ppm range.

The textural properties are assessed by N_2 adsorption-desorption analysis. As shown in **Figure** S7a, all the samples exhibit a type IV isotherm with a hysteresis at high relative pressure p/p_o.[29,31,34] Benefiting from the 3D hierarchical porous framework assembled by numerous nanoplatelets, 3D-CN-C1 exhibits a quite large specific surface area of 78.8 $m^2\ g^{-1}$, which is approximately 6.2 times higher than that of bulk g-C_3N_4 (B-CN) (12.8 $m^2\ g^{-1}$). The further increased specific surface area (86.9 $m^2\ g^{-1}$) of 3D-CN-C2 can be attributed to the formation of more mesopores in the nanoplatelets by a higher calcination temperature. The g-C_3N_4 nanosheet (NS-CN) sample has a surface area of 99.7 $m^2\ g^{-1}$ (**Table** S1). Compared with bulk g-C_3N_4 (B-CN) and g-C_3N_4 nanosheets (NS-CN), the much wider pore size distributions (2-30 nm) for 3D-CN-C1 and 3D-CN-C2 (**Figure** 7Sb) indicate that the novel HFDT method is beneficial for the formation of supplementary mesopores, thus improving the mass transportation.[31,34] The sharp N_2 adsorption uptake at high p/p_o of isotherms suggests the presence of interparticular macroporosity, confirming hierarchical porosity in g-C_3N_4 nanosheets and 3D-CN-CX samples.

The photographs of as-prepared samples are shown in **Figure** S8a. Two 3D-CN-C samples exhibit much deeper color than bulk g-C_3N_4 (B-CN) and g-C_3N_4 nanosheets (NS-CN), demonstrating their improved solar light harvesting upon the introduction of carbon vacancies.[24] UV/Visible absorption spectra (**Figure** S8b) demonstrate that the absorption edge of two 3D-CN-C samples shifts to longer wavelength in the visible region, being consistent with its brown-colored appearance. Noteworthy, these two samples show an obvious tail absorption (about 660 nm) in the visible range, which is induced by the additional electronic states located within the intrinsic band gap of the semiconductor. The additional electronic states are also well known as mid-gap states generally derived from lattice vacancies or dopants.[20,21] A Tauc plot of 3D-CN-C1 is shown in **Figure** S8c. The midgap state induced energy gap is calculated to be 1.77 eV, which is much narrower than the band gaps (Eg = 2.52 and 2.5 eV) of bulk g-C_3N_4 (B-CN) and g-C_3N_4 nanosheets (NS-CN), respectively. Due to the energy difference between the mid-gap state and the intrinsic gap state, the photoinduced carriers in 3D-CN-C1 can spontaneously transfer between these two band gaps under visible light irradiation, which can significantly enhance the separation efficiency of photoinduced carriers and subsequently promote the photocatalytic activity of 3D-CN-C1.[22] Compared with 3D-CN-C1, the dark brown 3D-CN-C2 exhibits an even higher absorption in the visible region due to the generation of more carbon vacancies.[12,13]

Density-functional theory (DFT) calculations of the band structure and partial density of states (PDOS) for bulk g-C_3N_4 (B-CN) and carbon defective 3D porous g-C_3N_4 (3D-CN-C) were conducted to establish the intrinsic relationship between carbon vacancies and the decreased bandgap values. For 3D-CN-C1/2 samples, the carbon vacancy percentages are set on the basis of elemental analysis results to 10 and 15%, respectively. The extended model structures of bulk g-C_3N_4 (B-CN) and 3D-CN-C are shown in **Figure** 2e and h, respectively. With the introduction of carbon vacancies into the heptazine units of carbon nitride, the bandgap value of 3D-CN-C1 is significantly reduced from 2.48 eV (bulk g-C_3N_4) to 1.81 eV (**Figures** 2f and 2i), being in good agreement with the Tauc plots (**Figure** S8c) and the tail absorption around 660 nm in **Figure** S8b. For bulk g-C_3N_4 (B-CN), both C 2p and N 2p orbitals contribute to the conduction band (CB), while the valence band (VB) mainly consists of N 2p orbitals (**Figure** 2g).[35] The band structure of g-C_3N_4 nanosheets (NS-CN) is similar to that of bulk g-C_3N_4 (B-CN) as there are no carbon vacancies in both samples. The DOS of 3D-CN-C1 shows that the CB is mainly dominated by the C2p and N2p orbitals, and the VB is composed of the N 2p orbitals and to a lesser extent of C2p and defect site orbitals (**Figure** 2j).[26] Importantly, a defect induced mid-gap energy level appears approximately 1.48 eV above the valance band (**Figure** 2i), thus promoting photoinduced carriers separation in 3D-CN-C1 sample.[22,27] These results demonstrate that the significantly reduced bandgap of 3D-CN-C1 as compared with that of bulk g-C_3N_4 (B-CN) and g-C_3N_4 nanosheets (NS-CN) is due to the existence of carbon vacancies in the heptazine units.[24] The calculated band structure and corresponding PDOS for 3D-CN-C2 sample are illustrated in **Figures** S9a and S9b, showing that a further decrease in the band gap is achieved and a defect energy level at 0.9 eV is generated given the higher amount of carbon vacancies. **Figure** 2k confirms that the highest occupied molecular orbital (HOMO) and lowest unoccupied molecular orbital (LUMO) locations of g-C_3N_4 (B-CN) are uniformly delocalized over the heptazine rings given of the high symmetry of the planar structure in the g-C_3N_4 framework.[26,27] Conversely, the charge density is redistributed with electron-rich areas in 3D-CN-C1 (**Figure** 2l). Such localized charge accumulation is ascribed to the defect-related mid-gap states in carbon nitride, which prohibits the recombination of charge carriers and favors an enhanced photocatalytic activity.[21,24] Furthermore, EDD plots (**Figures** S9c and 9d) show the enrichment of electron density at the uncoordinated N atom sites, hence favoring for photoreduction.

3.2 Photoelectric characterization

The photocurrent response is a direct indication of the photoinduced carriers separation rate in a material.[37,38] 3D-CN-C1 sample presents a much higher photocurrent response than the bulk g-C_3N_4 (B-CN) and g-C_3N_4 nanosheets (NS-CN) reference sample, indicating that the introduction of carbon vacancies significantly favors the electron-hole pair separation (**Figure** 3a). For the 3D-CN-C2 sample, the photocurrent response is also higher than that of reference samples, with however an attenuated photocurrent response as compared to 3D-CN-C1 attributed to a reduced charge carrier mobility at higher vacancy density. With higher vacancy concentration, the average distance between the trapping sites becomes small, increasing the recombination probability of electron-hole pairs[39] indicating the importance of well controlled carbon vacancy concentration. The excitonic states were also analyzed by photoluminescence (PL) measurements and as shown in **Figure** 3b. Generally, the radiative transition and non-radiative transition are existed during the excited electrons transfer from the high energy level to low energy level.[40,41] For the radiative transition, the photoluminescence is presented because of the electrons transition from the excited state to the ground state. Differently, no photoluminescence is formed due to the vibrational relaxation process of electrons in the non-radiative transition process. In our case, the 3D-CN-C1 and 3D-CN-C2 exhibit drastically lower PL emission intensities in comparision to bulk g-C_3N_4 (B-CN) and g-C_3N_4 nanosheets (NS-CN). This demonstrates that the non-radiative recombination of electrons and holes is the main decay process in the two deficient samples and the radiative recombination is the main decay process in B-CN and NS-CN. The photocurrent response versus different monochromatic light illuminations (**Figure** 3c) shows again that 3D-CN-C1 exhibits a greatly enhanced current in both the visible and UV range, demonstrating augmented photocurrent and broadened photo-response range. Additionally, the electrochemical impedance spectra (EIS) (**Figure** S10) illustrate the much smaller arc radius of the 3D-CN-C1 electrode, indicative of much faster electron transfer kinetics and surface reaction rate in the 3D-CN-C1 sample.[29]

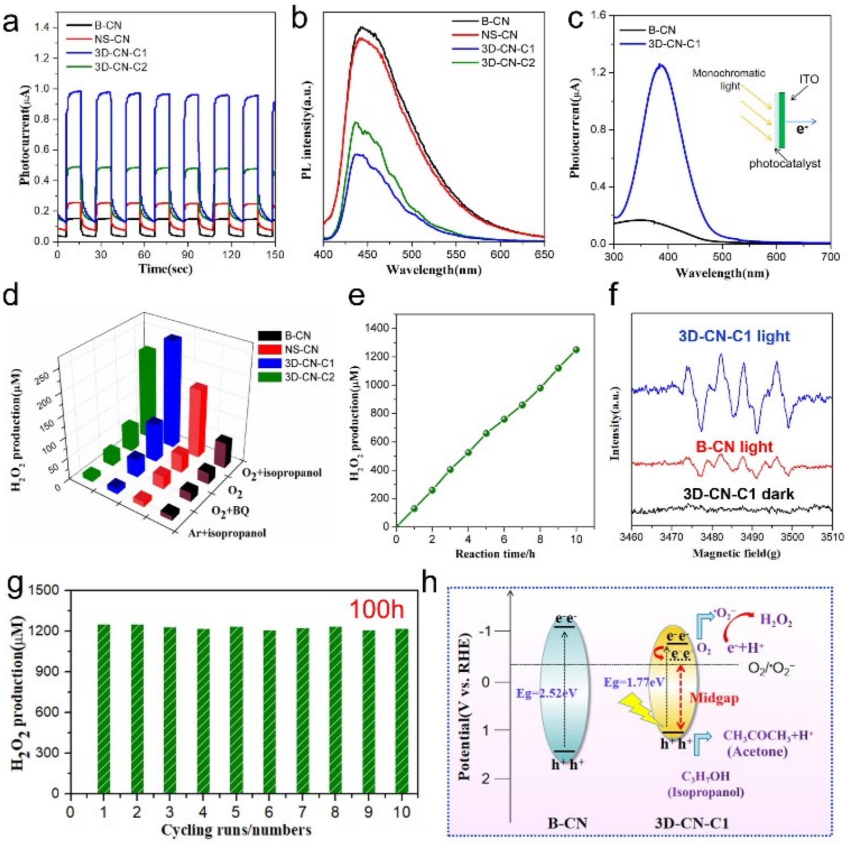

Figure 3. **Photoelectrochemical characterization and photocatalytic H_2O_2 production**

(a) Transient photocurrent intensity and (b) PL spectra of the as-prepared samples. (c) Photocurrent response of B-CN and 3D-CN-C1 samples under various monochromatic light illuminations. (d) Photocatalytic production rate of H_2O_2 with different additive agents under visible light irradiation for 2h for the as-prepared photocatalysts (photocatalyst loading of 20 mg in each reaction system). (e) Time-dependent photocatalytic production of H_2O_2 by the 3D-CN-C1 sample in the "O_2+isopropanol" system. (f) ESR signals of DMPO-$^{\bullet}O_2^-$ for B-CN and 3D-CN-C1 under visible light irradiation and dark condition. (g) Cycling tests of the 3D-CN-C1 sample for H_2O_2 production. (h) The proposed mechanism for photosynthetic H_2O_2 production in B-CN and 3D-CN-C1 samples in the "O_2+isopropanol" reaction system.

3.3 Photocatalytic performance

The photocatalytic H_2O_2 production efficiency was studied with different reactants under visible light irradiation (**Figure** 3d). Clearly, the 3D-CN-C1 sample presents the highest photocatalytic activity for H_2O_2 production whatever the reaction system was employed. In the "O_2+isopropanol" system, the 3D-CN-C1 shows an unprecedentedly high H_2O_2 output of 251.5 μM (H_2O_2 evolution rate of 6287.5 μM g^{-1} h^{-1}), being considerably higher than that of bulk g-C_3N_4 and g-C_3N_4 nanosheets (4.2 and 1.6 times, respectively). Although the surface area of the NS-CN (99.7 m^2 g^{-1}) is larger than that of the 3D-CN-C1 (78.8 m^2 g^{-1}), the photocatalytic H_2O_2 production activity of the later is significantly higher, which is related to the enhanced separation of the photoinduced carriers, the increased visible light harvesting and utilization owing to carbon vacancies.**[21,27]** The 3D-CN-C1 sample exhibits a better performance than 3D-CN-C2 owing to its better controlled carbon vacancy concentration, offering an excellent electron-hole separation rate. Contrast experiments were also carried out to explore the mechanism of the photocatalytic H_2O_2 production (**Figure** 3d). When the O_2 was replaced by Argon, all the samples exhibit negligible H_2O_2 production, revealing the vital role of O_2 in the H_2O_2 production. Compared with the "O_2+isopropanol" system, eliminating the isopropanol leads to a lower photocatalytic H_2O_2 production. Although the 3D-CN-C1 sample still has the highest H_2O_2 production rate of 158 μM in a pure O_2 system, it is lower than that in the "O_2+isopropanol" system, indicating that isopropanol acts as a sacrificial agent, which preferentially combines with the photogenerated holes and facilitates the formation of a proton (H^+). Hence, the lower H_2O_2 production for all the as-prepared photocatalysts in the O_2 system (without isopropanol) is possibly originated from the combination of $^{\bullet}O_2^-$ and H^+ from water. The generation of $^{\bullet}O_2^-$ intermediate species during photocatalytic H_2O_2 production is revealed by the use of ESR (electron spin resonance) technique (**Figure** 3f).**[9]** Again, the 3D-CN-C1 photocatalyst is found to give the higher intensity for DMPO-$^{\bullet}O_2^-$ signal, suggesting enhanced $^{\bullet}O_2^-$ formation capability of 3D-CN-C1.**[27]** No DMPO-$^{\bullet}O_2^-$ signal was found for 3D-CN-C1 photocatalyst under dark condition, indicating the significant role of light for photoelectrons formation. To further understand the influence of $^{\bullet}O_2^-$ on the H_2O_2 production, BQ was used as radical scavenger. All samples show a reduced H_2O_2 production in the "O_2+BQ" system, which demonstrates the essential role of $^{\bullet}O_2^-$ intermediate in the H_2O_2 production process.**[12,15]** Ten consecutive photocatalytic H_2O_2 production runs with a total reaction time of 100 hours (**Figure** 3g) were carried out. It is worth noting that each cycle extends to a very long reaction duration of 10 hours, the longest cycle duration compared to the literature. Generally, the photocatalytic H_2O_2 production over C_3N_4 based materials suffers from unsatisfactory stability after long-term cycling due to the intrinsically decreased crystallinity and self-decomposition of H_2O_2 on the surface of photocatalysts. Inspiringly, the H_2O_2 production of our 3D-CN-C1 photocatalyst remains almost unchanged after a long term cycling operation of 100h, which is superior than that of C_3N_4 based photocatalysts reported in previous publications (**Table** S2). Combined with the fact that the H_2O_2 production of 3D-CN-C1 increases linearly as function of reaction time (**Figure** 3e), this indicates a stable and robust photocatalytic process and materials. The high efficiency and extraordinary stability for H_2O_2 production endow our 3D-CN-C1 photocatalyst a great potential in practical production and application. The XRD pattern and TEM image of the 3D-CN-C1 sample after use (**Figure** S11) additionally proves its excellent stability.[15] The H_2O_2 production rate of 6287.5 $\mu M\ g^{-1}\ h^{-1}$ by the 3D-CN-C1 sample under visible light is the best value and much higher than the values reported in literature (**Table** S2). Moreover, the consecutive cycling tests of the B-CN and NS-CN samples for H_2O_2 production were also conducted for ten cycles and presented in **Figure** S12. The stable input of H_2O_2 further indicates the merits of g-C_3N_4 based materials in photocatalytic H_2O_2 formations and more studies should focus on this promising field in the future.[19-21] The photocatalytic H_2O_2 experiments over 3D-CN-1 photocatalyst under various monochromatic light illumination were conducted. As shown in **Figure** S13, there is almost no H_2O_2 formation when the wavelength of monochromatic light over 550 nm. Meanwhile, the wavelength-dependent H_2O_2 evolution matches well with photocurrent response curves (**Figure** 3c) rather than UV-vis absorption spectrum (**Figure** S8b), indicating the crucial role of photoinduced charges separation in photocatalytic H_2O_2 evolution.[27,28] Although the 3D-CN-1 photocatalyst displays the stronger absorption over 550 nm, the photoinduced charge separation is still unsatisfactory as verified by the photocurrent response curves, thus leading to the poor H_2O_2 evolution. The above results suggest that in addition to the enhanced light absorption, the formation and separation of photoinduced carriers are also essential for the photocatalytic process.[33,38]

3.4 Photoelectric mechanism

Based on the structural and catalytic analyses, a mechanism for the photosynthetic H_2O_2 production is proposed (**Figure** 3h). The reduced band gap, as determined from XPS valence band spectra (**Figure** S14) and Tauc plots (**Figure** S8c),[31,26] combined with the 3D hierarchical porous architecture of 3D-CN-C, is favorable for visible light absorption. Moreover, the formed mid-gap states in 3D-CN-C facilitate the electron-hole transfer and separation under visible light illumination.[19,24] The holes are trapped by isopropanol to generate acetone and protons (H^+). Besides, the accumulated electrons in the 3D-CN-C conduction band are easily captured by O_2, generating $^{\bullet}O_2^-$ given that the energy level of the conduction band in 3D-CN-C is lower than that of $O_2/^{\bullet}O_2^-$ redox couple (-0.33 eV vs RHE). H_2O_2 is finally produced due to the further reduction of $^{\bullet}O_2^-$. The detailed route of the photosynthetic H_2O_2 production process is presented and discussed from **Equations** S1-4 (Supporting Information).

Fukui function (FF) simulations were additionally carried out to reveal the role of carbon vacancies in the photocatalytic H_2O_2 production process.[42] The Fukui charge values of various N sites are displayed in **Figure** S15. Compared with the FF plot of bulk g-C_3N_4 (**Figure** 4a), the 3D-CN-C sample shows a very high degree of active sites favoring radical attack (**Figure** 4b). The N atoms in the carbon defective triazine ring present a very large degree of affinity towards a radical attack which is essential towards high yield of H_2O_2 production. Adsorption simulations[43] show that 3D-CN-C1 (**Figure** 4d) demonstrates a very high extent of $^{\bullet}O_2^-$ radical loading compared with bulk g-C_3N_4, wherein the adsorption of $^{\bullet}O_2^-$ radicals is through a weak H bonding with H atoms linked with the C and N atoms in the triazine ring (**Figure** 4c). The affinity for the $^{\bullet}O_2^-$ radicals significantly increases in case of 3D-CN-C1 as a

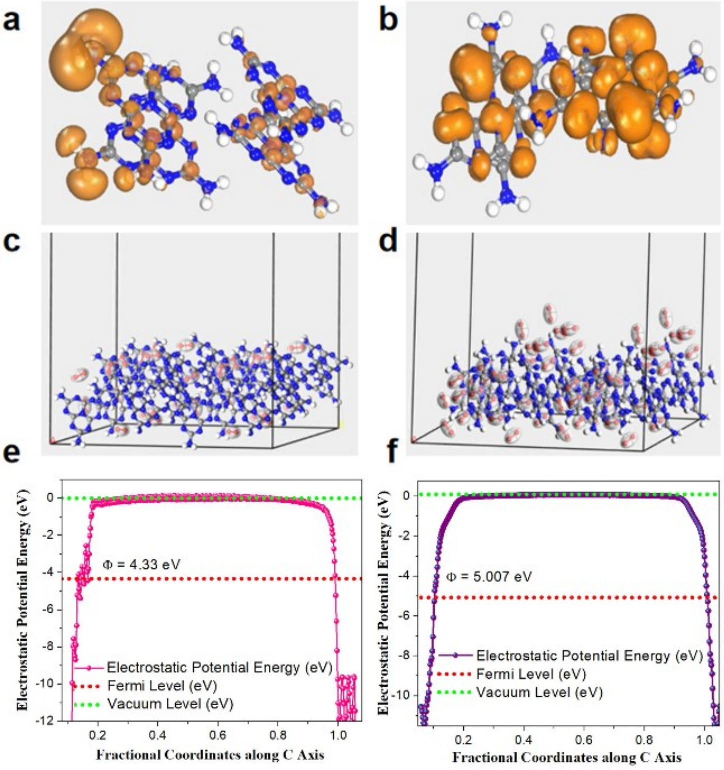

Figure 4. **Fukui Function (FF) plots and Electrostatic potential plots**

Fukui Function (FF) plots for favored radical attack site for (a) B-CN and (b) 3D-CN-C. $^{\bullet}O_2^-$ adsorption simulations for (c) B-CN and (d) 3D-CN-C. Electrostatic potential plots for (e) B-CN and (f) 3D-CN-C.

significant accumulation of $^{\bullet}O_2^-$ species is observed around the carbon vacancies from the HOMO-LUMO and FF simulations, which is favorable for H_2O_2 production. Electrostatic potential energy plots are shown in **Figures** 4e and 4f for bulk g-C_3N_4 and 3D-CN-C1, respectively. The work function value of 3D-CN-C1 is 5.007 eV, considerably larger than 4.33 eV of bulk g-C_3N_4. The higher work function of 3D-CN-C1 suggests its stronger electron affinity in favor of $^{\bullet}O_2^-$ radicals formation.[44,45] The Fermi level value in 3D-CN-C samples also shifts to more negative values compared to bulk g-C_3N_4, indicating the formation of higher band bending and charge injection for 3D-CN-C1 and provides a high driving force for photoreduction.[46] All these results demonstrate that carbon vacancies have strong electrons affinity and promote the generation of $^{\bullet}O_2^-$ radicals, that are responsible for the unprecedented photocatalytic H_2O_2 production performance and a better modulation of their concentration is essential.

4. Conclusions

A significantly enhanced photocatalytic H_2O_2 production with an extraordinary stability is achieved by a novel carbon deficient 3D hierarchical porous g-C_3N_4 scaffold prepared by an innovative hydrolysis-freeze drying-thermal treatment (HFDT) process. The carbon vacancies in the C_3N_4 lattice are found to decrease the band gap and generate mid-gap electronic levels, broadening the visible-light absorption and facilitating the photo-induced carrier separation. The ESR spin-trap experiments confirm the essential role of intermediate $^{\bullet}O_2^-$ radical species during photocatalytic H_2O_2 production. The carbon vacancies show a very strong affinity for electrons and $^{\bullet}O_2^-$ radicals and their accumulation in close proximity of the active sites favors the $^{\bullet}O_2^-$ reduction, boosting H_2O_2 production. On the other hand, the unique 3D hierarchical porous g-C_3N_4 structure with a larger specific surface area and abundant pores provides numerous reactive centers and convenient pathway for the transport of reactants and products. Our photocatalyst with a well-controlled carbon vacancy concentration demonstrates a H_2O_2 output of 6287.5 μM g^{-1} h^{-1} under visible light irradiation with an outstanding long cycling stability, being the best value achieved to date when compared to other similar reported photocatalysts in literature. This work offers highly efficient photocatalysts suitable for a safe and environmentally friendly large scale industrial production of H_2O_2.

Acknowledgement

Y. Ding thanks the financial support from the China Scholarship Council (201808310127). This work is financially supported by National Natural Science Foundation of China (U1663225), Program for Changjiang Scholars and Innovative Research Team in University (IRT_15R52) of the Chinese Ministry of Education, Program of Introducing Talents of Discipline to Universities-Plan 111 (Grant No. B20002) from the Ministry of Science and Technology and the Ministry of Education of China and the National Key R&D Program of China (2016YFA0202602). This research was also supported by the European Commission Interreg V France-Wallonie-Vlaanderen project "DepollutAir".

References

1. Chen, L., Wang, L., Wan, Y., Zhang, Y., Qi, Z., Wu, X., and Xu, H. (2020). Acetylene and Diacetylene Functionalized Covalent Triazine Frameworks as Metal-Free Photocatalysts for Hydrogen Peroxide Production: A New Two-Electron Water Oxidation Pathway. Adv. Mater. 32, 1904433.

2. Hirakawa, H., Shiota, S., Shiraishi, Y., Sakamoto, H., Ichikawa, S., and Hirai, T. (2016). Au Nanoparticles Supported on $BiVO_4$: Effective Inorganic Photocatalysts for H_2O_2 Production from Water and O_2 under Visible Light. ACS Catal. 6, 4976-4982.

3. Kofuji, Y., Isobe, Y., Shiraishi, Y., Sakamoto, H., Tanaka, S., Ichikawa, S., and Hirai, T. (2016). Carbon Nitride–Aromatic Diimide–Graphene Nanohybrids: Metal-Free Photocatalysts for Solar-to-Hydrogen Peroxide Energy Conversion with 0.2% Efficiency. J. Am. Chem. Soc. 138, 10019-10025.

4. Cai, J., Huang, J., Wang, S., Iocozzia, J., Sun, Z., Sun, J., Yang, Y., Lai, Y., and Lin, Z. (2019). Crafting Mussel-Inspired Metal Nanoparticle-Decorated Ultrathin Graphitic Carbon Nitride for the Degradation of Chemical Pollutants and Production of Chemical Resources. Adv. Mater. 31, 1806314.

5. Shiraishi, Y., Kofuji, Y., Sakamoto, H., Tanaka, S., Ichikawa, S., and Hirai, T. (2015). Effects of Surface Defects on Photocatalytic H_2O_2 Production by Mesoporous Graphitic Carbon Nitride under Visible Light Irradiation. ACS Catal. 5, 3058-3066.

6. Teranishi, M., Hoshino, R., Naya, S. I., and Tada, H. (2016). Gold-Nanoparticle-Loaded Carbonate-Modified Titanium (IV) Oxide Surface: Visible-Light-Driven Formation of Hydrogen Peroxide from Oxygen. Angew. Chem. Int. Ed. 55, 12773-12777.

7. Zhang, P., Tong, Y., Liu, Y., Vequizo, J. J. M., Sun, H., Yang, C., Yamakata, A., Fan, F., Lin, W., Wang, X., and Choi, W. (2020). Heteroatom Dopants Promote Two-Electron O_2 Reduction for Photocatalytic Production of H_2O_2 on Polymeric Carbon Nitride. Angew. Chem. Int. Ed. 59, 16209-16217.

8. Tsukamoto, D., Shiro, A., Shiraishi, Y., Sugano, Y., Ichikawa, S., Tanaka, S., and Hirai, T. (2012). Photocatalytic H_2O_2 Production from Ethanol/O_2 System Using TiO_2 Loaded with Au-Ag Bimetallic Alloy Nanoparticles. ACS Catal. 2, 599-603.

9. Hou, H., Zeng, X., and Zhang, X. (2020). Production of Hydrogen Peroxide by Photocatalytic Processes. Angew. Chem. Int. Ed. 59, 17356-17376.

10. Shiraishi, Y., Kanazawa, S., Kofuji, Y., Sakamoto, H., Ichikawa, S., Tanaka, S., and Hirai, T. (2014). Sunlight-Driven Hydrogen Peroxide Production from Water and Molecular Oxygen by Metal-Free Photocatalysts. Angew. Chem. Int. Ed. 53, 13454-13459.

11. Yang, L., Chen, H., Xu, Y., Qian, R., Chen, Q., and Fang, Y. (2022). Synergetic effects by Co^{2+} and PO_4^{3-} on Mo-doped $BiVO_4$ for an improved photoanodic H_2O_2 evolution. Chem. Eng. Sci. 251, 117435.

12. Fang, Y., Hou, Y., Fu, X., and Wang, X. (2022). Semiconducting Polymers for Oxygen Evolution Reaction under Light Illumination. Chem. Rev. 122, 3, 4204–4256.

13. Peng, Y., Zhou, L., Wang, L., Lei, J., Liu, Y., Daniele, S., and Zhang, J. (2019). Preparation of NiCoP-decorated g-C_3N_4 as an efficient photocatalyst for H_2O_2 production. Res. Chem. Intermediat. 45, 5907-5917.

14. Isaka, Y., Kawase, Y., Kuwahara, Y., Mori, K., and Yamashita, H. (2019). Two-Phase System Utilizing Hydrophobic Metal–Organic Frameworks (MOFs) for Photocatalytic Synthesis of Hydrogen Peroxide. Angew. Chem. Int. Ed. 58, 5402-5406.

15. Wei, Z., Liu, M., Zhang, Z., Yao, W., Tan, H., and Zhu, Y. (2018). Efficient visible-light-driven selective oxygen reduction to hydrogen peroxide by oxygen-enriched graphitic carbon nitride polymers. Energ. Environ. Sci. 11, 2581-2589.

16. Lei, J., Chen, B., Lv, W., Zhou, L., Wang, L., Liu, Y., and Zhang, J. (2019). Robust Photocatalytic H_2O_2 Production over Inverse Opal g-C_3N_4 with Carbon Vacancy under Visible Light. ACS Sustain. Chem. Eng. 7, 16467-16473.

17. Kim, H. I., Kwon, O. S., Kim, S., Choi, W., and Kim, J. H. (2016). Harnessing low energy photons (635 nm) for the production of H_2O_2 using upconversion nanohybrid photocatalysts. Energ. Environ. Sci. 9, 1063-1073.

18. Moon, G. H., Kim, W., Bokare, A. D., Sung, N. E., and Choi, W. (2014). Solar production of H_2O_2 on reduced graphene oxide-TiO_2 hybrid photocatalysts consisting of earth-abundant elements only. Energ. Environ. Sci. 7, 4023-4028.

19. Zhao, Q., Fu, L., Jiang, D., Xi, Y., and Yang, H. (2018). A nanoclay-induced defective g-C_3N_4 photocatalyst for highly efficient catalytic reactions. Chem. Commun. 54, 8249-8252.

20. Lau, V. W. H., Yu, V. W. Z., Ehrat, F., Botari, T., Moudrakovski, I., Simon, T., Duppel, V., Medina, E., Stolarczyk, J., Feldmann, J., and Lotsch, B. V. (2017). Urea-Modified Carbon Nitrides: Enhancing Photocatalytic Hydrogen Evolution by Rational Defect Engineering. Adv. Energy Mater. 7, 1602251.

21. Yu, H., Shi, R., Zhao, Y., Bian, T., Zhao, Y., Zhou, C., Waterhouse, G., Wu, L-Z., Tung, C-H., and Zhang, T. (2017). Alkali-Assisted Synthesis of Nitrogen Deficient Graphitic Carbon Nitride with Tunable Band Structures for Efficient Visible-Light-Driven Hydrogen Evolution. Adv. Mater. 29, 1605148.

22. Yang, P., Zhuzhang, H., Wang, R., Lin, W., and Wang, X. (2019). Carbon Vacancies in a Melon Polymeric Matrix Promote Photocatalytic Carbon Dioxide Conversion. Angew. Chem. Int. Ed. 58, 1134-1137.

23. Wang, W., Zhang, H., Zhang, S., Liu, Y., Wang, G., Sun, C., and Zhao, H. (2019). Potassium-Ion-Assisted Regeneration of Active Cyano Groups in Carbon Nitride Nanoribbons: Visible-Light-Driven Photocatalytic Nitrogen Reduction. Angew. Chem. Int. Ed. 58, 16644-16650.

24. Shi, L., Yang, L., Zhou, W., Liu, Y., Yin, L., Hai, X., Song, H., and Ye, J. (2018). Photoassisted Construction of Holey Defective g-C_3N_4 Photocatalysts for Efficient Visible-Light-Driven H_2O_2 Production. Small. 14, 1703142.

25. Liu, D., Chen, D., Li, N., Xu, Q., Li, H., He, J., and Lu, J. (2020). Surface Engineering of g-C_3N_4 by Stacked BiOBr Sheets Rich in Oxygen Vacancies for Boosting Photocatalytic Performance. Angew. Chem. Int. Ed. 59, 4519-4524.

26. Zhao, D., Dong, C. L., Wang, B., Chen, C., Huang, Y. C., Diao, Z., Li, S., Guo, L., and Shen, S. (2019). Synergy of Dopants and Defects in Graphitic Carbon Nitride with Exceptionally Modulated Band Structures for Efficient Photocatalytic Oxygen Evolution. Adv. Mater. 31, 1903545.

27. Feng, C., Tang, L., Deng, Y., Wang, J., Luo, J., Liu, Y., Ouyang, X., Yang, H., Yu, J., and Wang, J. (2020). Synthesis of Leaf-Vein-Like g-C_3N_4 with Tunable Band Structures and Charge Transfer Properties for Selective Photocatalytic H_2O_2 Evolution. Adv. Funct. Mater. 30, 2001922.

28. Teng, Z., Zhang, Q., Yang, H., Kato, K., Yang, W., Lu, Y. R., Liu, S., Wang, C., Yamakata, A., Su, C., Liu, B., and Ohno, T. (2021). Atomically dispersed antimony on carbon nitride for the artificial photosynthesis of hydrogen peroxide. Nat. Catal. 4, 374-384.

29. Chen, X., Shi, R., Chen, Q., Zhang, Z., Jiang, W., Zhu, Y., and Zhang, T. (2019). Three-dimensional porous g-C_3N_4 for highly efficient photocatalytic overall water splitting. Nano Energy. 59, 644-650.

30. Thaweesak, S., Wang, S., Lyu, M., Xiao, M., Peerakiatkhajohn, P., and Wang, L. (2017). Boron-doped graphitic carbon nitride nanosheets for enhanced visible light photocatalytic water splitting. Dalton Tran. 46, 10714-10720.

31. Zhao, H., Liu, J., Li, C. F., Zhang, X., Li, Y., Hu, Z-Y., Li, B., Chen, Z., Hu, J., and Su, B-L. (2022). Meso-Microporous Nanosheet-Constructed 3DOM Perovskites for Remarkable Photocatalytic Hydrogen Production. Adv. Funct. Mater. 2112831, 1-8.

32. Zhao, H., Li, C. F., Hu, Z. Y., Liu, J., Li, Y., Hu, J., Tendeloo, J., Chen, L-H., and Su, B-L. (2021). Size effect of bifunctional gold in hierarchical titanium oxide-gold-cadmium sulfide with slow photon effect for unprecedented visible-light hydrogen production. J. Colloid. Interface Sci. 604, 131-140.

33. Zeng, Y., Liu, X., Liu, C., Wang, L., Xia, Y., Zhang, S., Luo, S., and Pei, Y. (2018). Scalable one-step production of porous oxygen-doped g-C_3N_4 nanorods with effective electron separation for excellent visible-light photocatalytic activity. Appl. Catal. B. 224, 1-9.

34. Zhao, H., Liu, P., Wu, X., Wang, A., Zheng, D., Wang, S., Chen, Z., Larter, S., Li, Y., Su, B-L., Kibria, M., and & Hu, J. (2021). Plasmon enhanced glucose photoreforming for arabinose and gas fuel co-production over 3DOM TiO_2-Au. Appl. Catal. B. 291, 120055.

35. Wei, FY., Liu, Y., Zhao, H., Ren, X., Liu, J., Hasan, T., Chen, L., Li, Y., and Su, B-L. (2018). Oxygen self-doped g-C_3N_4 with tunable electronic band structure for unprecedentedly enhanced photocatalytic performance. Nanoscale. 10, 4515-4522.

36. Yücelen, E., Lazić, I., and Bosch, E. G. (2018). Phase contrast scanning transmission electron microscopy imaging of light and heavy atoms at the limit of contrast and resolution. Sci Rep. 8, 2676.

37. Zhang, W., Tian, Y., He, H., Xu, L., Li, W., and Zhao, D. (2020). Recent advances in the synthesis of hierarchically mesoporous TiO_2 materials for energy and environmental applications. Natl. Sci. Rev. 7, 1702-1725.

38. Zhao, H., Hu, Z., Liu, J., Li, Y., Wu, M., Van Tendeloo, G., and Su, B-L. (2018). Blue-edge slow photons promoting visible-light hydrogen production on gradient ternary 3DOM TiO_2-Au-CdS photonic crystals. Nano Energy. 47, 266-274.

39. Ding, Y., Maitra, S., Wang, C., Zheng, R., Zhang, M., Barakat, T., Roy, S., Liu, J., Li, Y., Hasan, T., and Su, B-L. (2022). Hydrophilic bi-functional B-doped g-C_3N_4 hierarchical architecture for excellent photocatalytic H_2O_2 production and photoelectrochemical water splitting. J. Energy Chem. 70, 236-247.

40. Li, Q., Anpo, M., and Wang, X. (2020). Application of photoluminescence spectroscopy to elucidate photocatalytic reactions at the molecular level. Res. Chem. Intermediat. 46, 4325-4344.

41. Anpo, M., and Che, M. (1999). Applications of photoluminescence techniques to the characterization of solid surfaces in relation to adsorption, catalysis, and photocatalysis. Adv. Catal. 44, 119-257.

42. Thanikaivelan, P., Padmanabhan, J., Subramanian, V., and Ramasami, T. (2002). Chemical reactivity and selectivity using Fukui functions: basis set and population scheme dependence in the framework of B3LYP theory. Theor Chem Acc. 107, 326-335.

43. Parr, R. G. (1990). On the genesis of a theory. Int J Quantum Chem. 37, 327-347.

44. Zhang, B., Liao, S., Wu, W., Li, H., and Ren, T. (2018). Work function: a determining factor of the photodegradation rate of methyl orange via hollow octadecahedron Cu_2O crystals. Phys. Chem. Chem. Phys. 20, 20117-20123.

45. Xia, P., Zhu, B., Cheng, B., Yu, J., and Xu, J. (2018). 2D/2D g-C_3N_4/MnO_2 Nanocomposite as a Direct Z-Scheme Photocatalyst for Enhanced Photocatalytic Activity. ACS Sustain. Chem. Eng. 6, 965-973.

46. Lohaus, C., Klein, A., and Jaegermann, W. (2018). Limitation of Fermi level shifts by polaron defect states in hematite photoelectrodes. Nat. Commun. 9, 1-7.

Graphical abstract

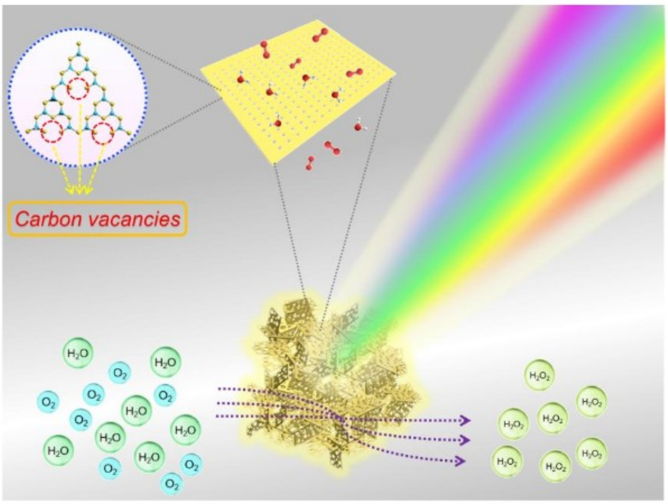

Supporting information

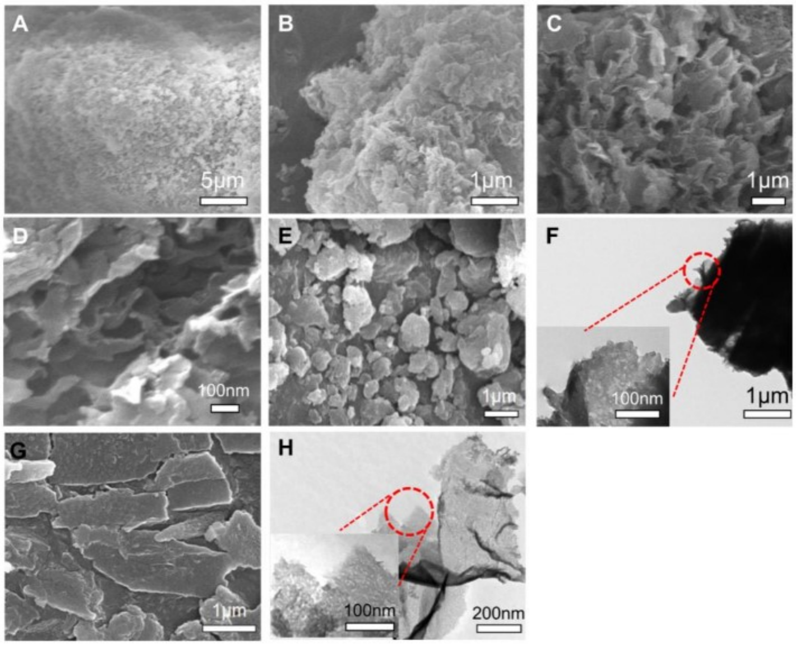

Figure S1. Electron microscope images of the as-prepared samples.

SEM images of (A) melamine, (B) cyanuric acid-melamine supramolecular polymers and (C) the supramolecular precursor after liquid N2 treatment. (D) SEM image of the as-prepared 3D-CN-C2 sample. SEM (E) and TEM (F) images of bulk g-C3N4 (B-CN). SEM (G) and TEM (H) images of C_3N_4 nanosheets (NS-CN).

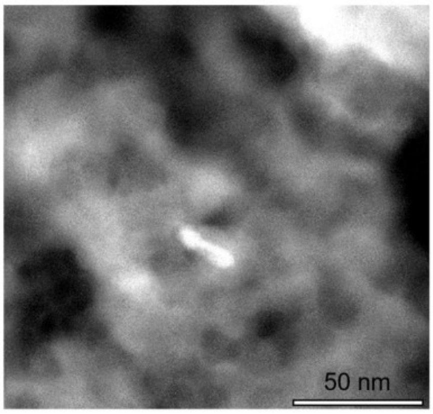

Figure S2. Enlarged HAADF-TEM image of the 3D-CN-C1 sample.

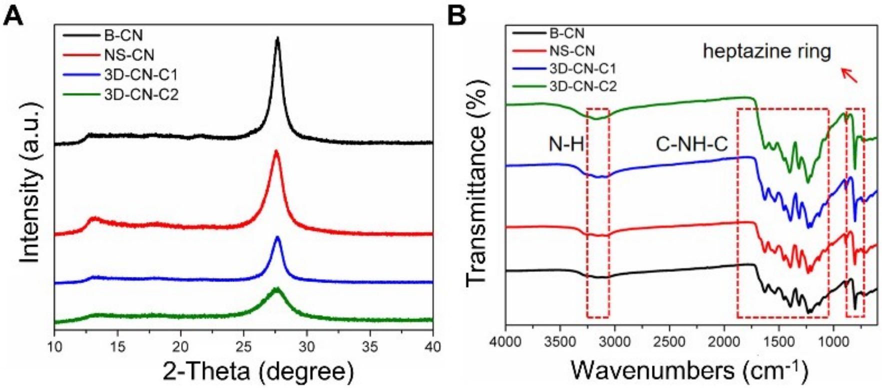

Figure S3. Structure characterizations.

(A) XRD patterns and (B) FT-IR spectra of the as-prepared B-CN, NS-CN and 3D-CN-C samples.

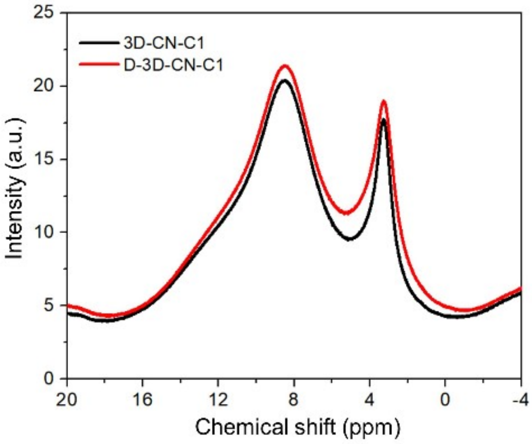

Figure S4. Solid-state 1H MAS NMR spectra of 3D-CN-C1 and D-3D-CN-C1 samples.

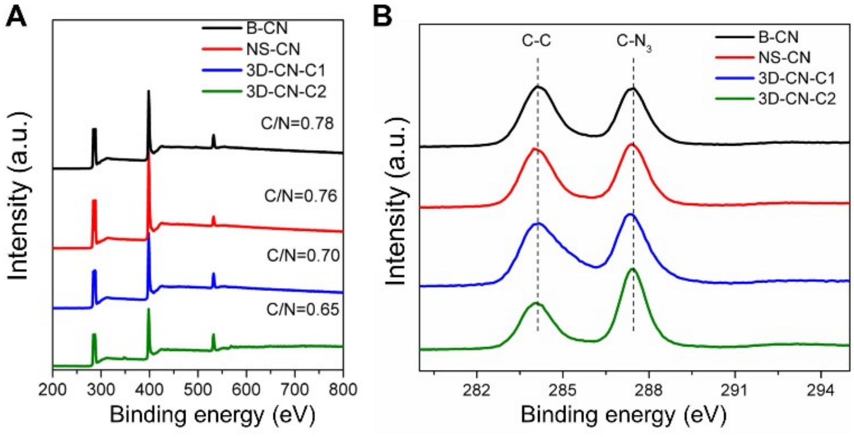

Figure S5. XPS characterizations.

(A) Full XPS spectra and (B) high-resolution XPS spectra of C1s of B-CN, NS-CN and 3D-CN-C samples.

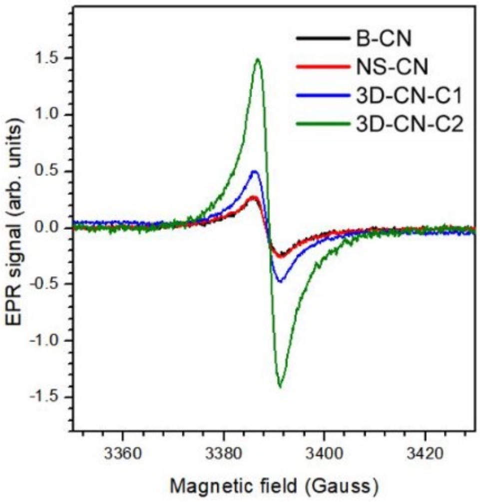

Figure S6. EPR spectra of the as-prepared samples.

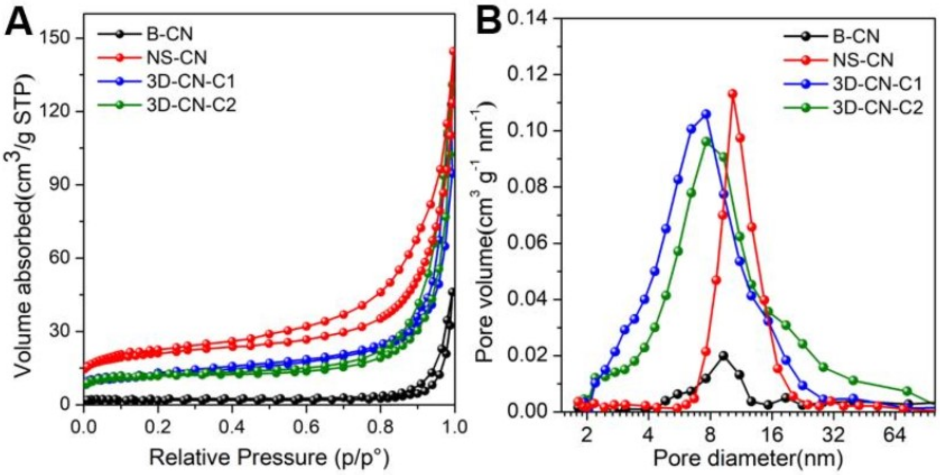

Figure S7. Textural properties.

(A) N2 adsorption-desorption isotherms and (B) pore size distribution curves of the as-prepared samples.

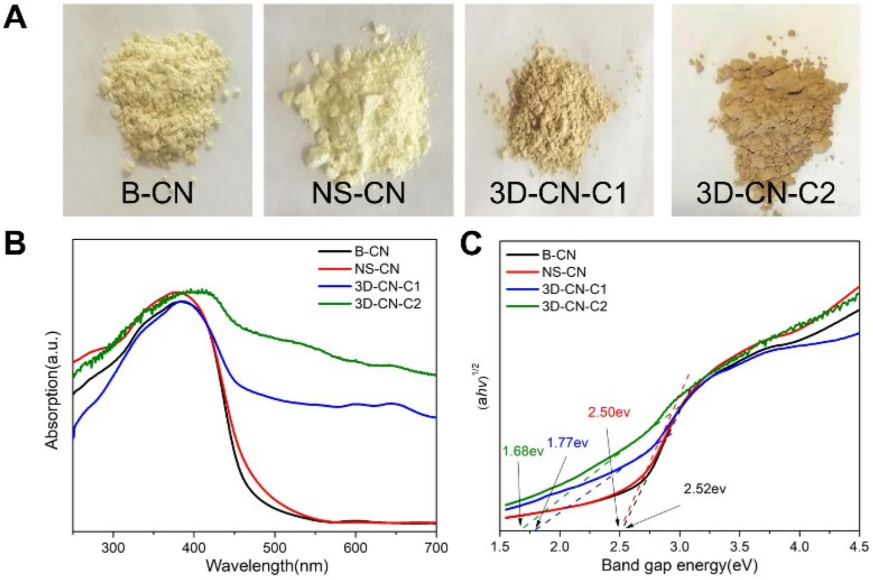

Figure S8. Optical and electronic properties.

(A) Photographs, (B) UV-vis absorption spectra and (C) Tauc plots of as-prepared samples.

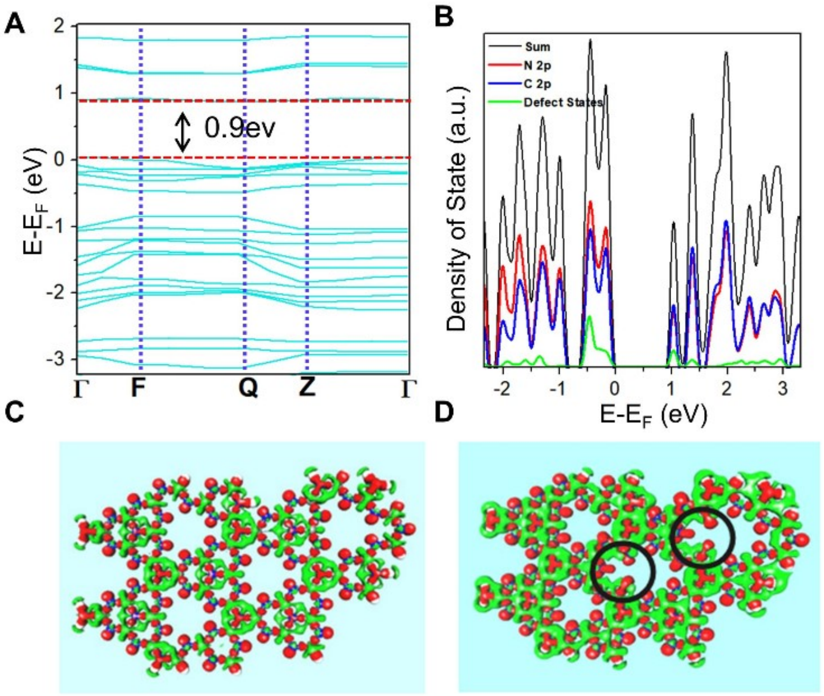

Figure S9. Theoretical calculations and simulations.

(A and B) Calculated band structure (A) and the corresponding PDOS (B) for 3D-CN-C2 sample. (C and D) Electron density difference (EDD) plots of (C) B-CN and (D) 3D-CN-C (Green indicates electron density depletion and red represents Electron density enrichment).

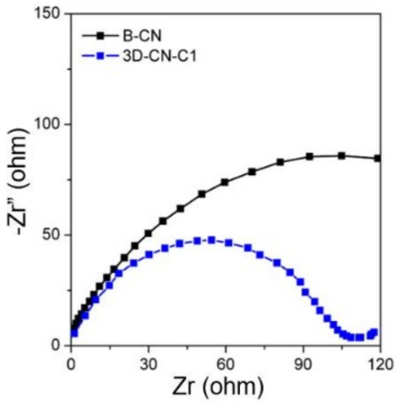

Figure S10. The electrochemical impedance spectra (EIS) of B-CN and 3D-CN-C1 samples.

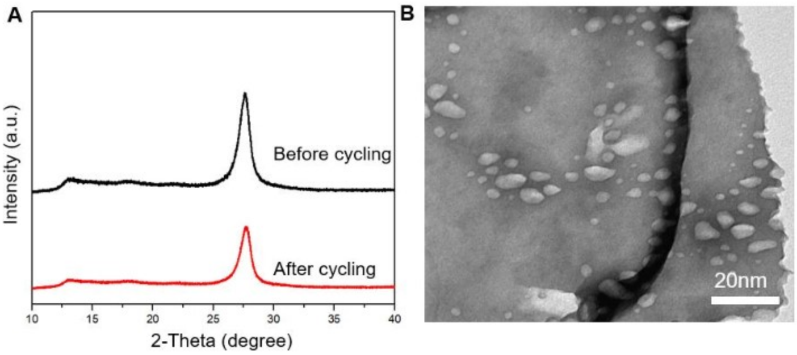

Figure S11. The characterizations of photocatalyst after cycling test.

(A) XRD pattern and (B) TEM image of 3D-CN-C1 sample after cycling test for 100 h.

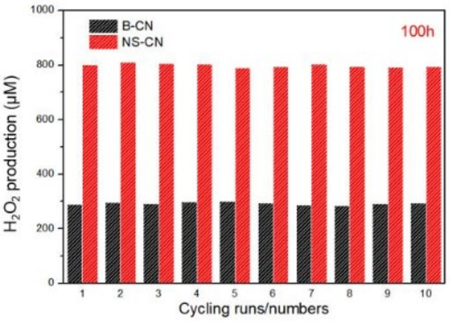

Figure S12. Cycling tests of the B-CN and NS-CN samples for H_2O_2 production.

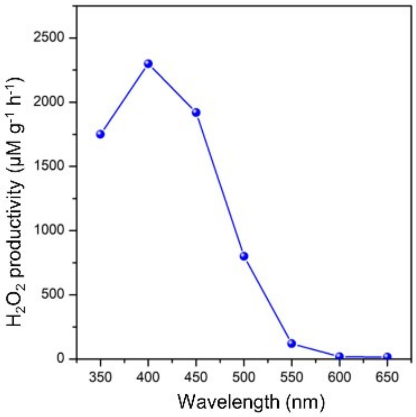

Figure S13. Photocatalytic H_2O_2 evolution rates over 3D-CN-1 photocatalyst in the "O2+isopropanol" system under various monochromatic light illumination.

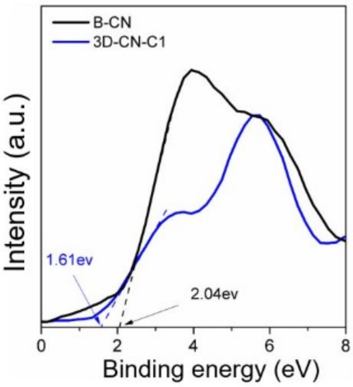

Figure S14. The XPS valence band spectra of bulk CN and 3D-CN-C1.

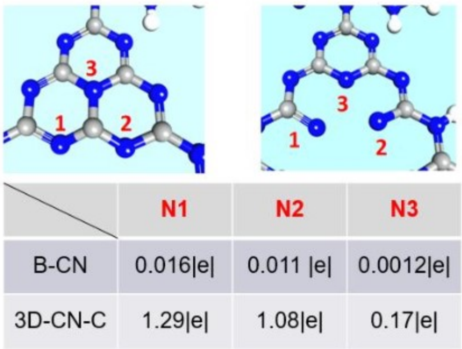

	N1	N2	N3
B-CN	0.016|e|	0.011 |e|	0.0012|e|
3D-CN-C	1.29|e|	1.08|e|	0.17|e|

Figure S15. The Fukui charge values of various N sites in bulk CN and 3D-CN-C1.

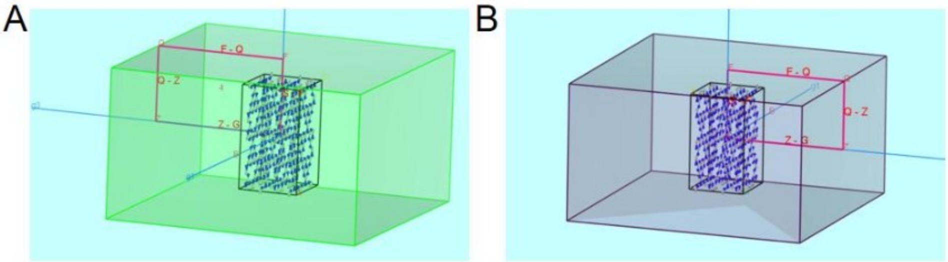

Figure S16. The K point paths for band structures of (a) bulk CN and (b) 3D-CN-C1.

Data S1. The detailed route of photosynthetic H2O2 production process can be described as follows:

$$3D-CN-C1 \xrightarrow{hv} e^- + h^+ \ldots\ldots\ldots(1)$$
$$C_3H_7OH + 2h^+ = CH_3COCH_3 + 2H^+ \ldots\ldots(2)$$
$$e^- + O_2 = {}^\bullet O_2^- \ldots\ldots\ldots\ldots\ldots\ldots\ldots\ldots(3)$$
$${}^\bullet O_2^- + e^- + 2H^+ = H_2O_2 \ldots\ldots\ldots\ldots\ldots(4)$$

Table S1. The specific surface areas and the relative ratios of C-N=C/H-N=C, N-$(C)_3$, N-H_2 and C/N determined by XPS spectra and the bulk relative contents of C, N, and H from elemental analysis for the as-prepared samples.

Samples	S_{BET} (m^2/g)	C-N=C/H-N=C %	N-$(C)_3$ %	N-H_2 %	C/N Atomic ratio (XPS)	C %	N %	H %	C/N Atomic ratio (Elemental analysis)
B-CN	12.8	63.2	27.2	9.6	0.78	40.67	55.73	1.71	0.73
NS-CN	99.7	64.7	25.3	10	0.76	39.59	56.12	1.74	0.71
3D-CN-C1	78.8	60.7	20.8	18.5	0.70	37.95	59.12	1.83	0.66
3D-CN-C2	86.9	59.8	15.4	24.8	0.65	36.81	59.2	1.88	0.62

Table S2. Comparison of photosynthetic H_2O_2 production by different photocatalysts.

Photocatalysts	Conditions	H_2O_2 production rate	Long-term cycling performance	Ref.
3D-CN-C1	Isopropanol+water, O_2, 20 mg, $\lambda \geq 400$ nm, 120w	6287.5 $\mu M\ g^{-1}\ h^{-1}$	Almost no changed after 100 h of cycling reaction	This work

g-C_3N_4/MTI	Water, O_2, $\lambda>420$ nm	22.9 μM g^{-1} h^{-1}	N/A	1
g-C_3N_4 aerogels	Water, O_2, $\lambda>420$ nm, 300 W	28.8 μM g^{-1} h^{-1}	N/A	2
g-C_3N_4/PDI-BN-rGO	Water, O_2, $\lambda>420$ nm, 2000 W	30.8 μM g^{-1} h^{-1}	N/A	3
g-C_3N_4/BDI	Water, O_2, $\lambda>420$ nm	34.2 μM g^{-1} h^{-1}	N/A	4
C-N-g-C_3N_4	Water, O_2, $\lambda>420$ nm	50.5 μM g^{-1} h^{-1}	48h of cycling reaction	5
g-C_3N_4	Alcohol+water, O_2, $\lambda>420$ nm, 2000 W	62.5 μM g^{-1} h^{-1}	N/A	6
Cv-g-C_3N_4	O_2, $\lambda\geq420$nm 300W	90 μM μM g^{-1} h^{-1}	N/A	7
g-C_3N_4 with hole defects	2-propanol+water, $\lambda>420$ nm	96.8 μM g^{-1} h^{-1}	7 h of cycling reaction	8
3DOM g-C_3N_4	Pure water, O_2, $\lambda\geq320$nm 300W	130 μM g^{-1} h^{-1}	2.5 h of cycling reaction	9
Covalent triazine frameworks	Pure water, O_2, $\lambda\geq420$ nm, 44.5 mW cm^{-2}	166.7 μM g^{-1} h^{-1}	N/A	10
Sb-g-C_3N_4	Water, O_2, $\lambda>420$ nm, 300 W	182.4 μM g^{-1} h^{-1}	N/A	11
Mesoporous g-C_3N_4	Ethanol+water, O_2, λ = 420-500nm 26.9 W	200 μM g^{-1} h^{-1}	N/A	12
CdS-graphene	Methanol+water, O_2, 50 mg, AM1.5G	213.3 μM g^{-1} h^{-1}	Productivity decaying after 3h of reaction	13
g-C_3N_4-Carbon	Isopropanol+water, O_2, 50 mg, UV-vis	317.75 μM g^{-1} h^{-1}	N/A	14
g-C_3N_4-CNTs	Formic acid+water, O_2, 100 mg, $\lambda\geq400$nm, 300 W	326 μM g^{-1} h^{-1}	Productivity decaying after 4h of reaction	15

Au/g-C_3N_4	Ethanol+water, O_2, 30 mg, λ≥420nm, 300 W	330 $\mu M\ g^{-1}\ h^{-1}$	Productivity decaying after 4h of reaction	16
K, P, O-doped g-C_3N_4	Ethanol+ water, λ≥420nm	485.7 $\mu M\ g^{-1}\ h^{-1}$	48 h of reaction cycling	17
KH_2PO_4/g-C_3N_4	Ethanol+water, O_2, 50 mg, λ≥420nm, 300 W	500 $\mu M\ g^{-1}\ h^{-1}$	N/A	18
g-C_3N_4/PDI51	Pure water, O_2, 50 mg, λ≥420 nm, 100w	700 $\mu M\ g^{-1}\ h^{-1}$	N/A	19
Ag@U-g-C_3N_4-NS	HClO+water, 100 mg 300W Xe lamp	750 $\mu M\ g^{-1}\ h^{-1}$	Productivity decaying after 1.5h of reaction	20
CdS-GO	Methanol+water, O_2, 0.5 g/L, λ = 635 nm, 23 mW/cm^2	950 $\mu M\ g^{-1}\ h^{-1}$	N/A	21
OCN-500	Isopropanol+water, O_2, 50 mg, λ≥420 nm,100w	1200 $\mu M\ g^{-1}\ h^{-1}$	N/A	22
g-C_3N_4/PI	Water, O_2, 300 W λ>420 nm, 0.56 W/cm^2	1240 $\mu M\ g^{-1}\ h^{-1}$	Productivity decaying after 2 h of reaction	23
K+/Na+-doped g-C_3N_4	Water, O_2, λ>400 nm, 250 W	1277.8 $\mu M\ g^{-1}\ h^{-1}$	Productivity decaying after 6 h of reaction	24
g-C_3N_4/PDI/rGO0.05	2-propanol+water, O_2, 50 mg, 420−500 nm, 43.3 W	1333.3 $\mu M\ g^{-1}\ h^{-1}$	N/A	25
Cu-doped g-C_3N_4	Water, O_2, λ>400 nm, 250 W	1340.3 $\mu M\ g^{-1}\ h^{-1}$	N/A	26
g-C_3N_4 with N vacancies	Ethanol+water, O_2, λ>400 nm, 250 W	1444.4 $\mu M\ g^{-1}\ h^{-1}$	Productivity decaying after 6 h of reaction	27
phosphate-modified g-C_3N_4	EDTA+water, O_2, λ>400 nm, 250 W	1500 $\mu M\ g^{-1}\ h^{-1}$	Productivity decaying after 6 h of reaction	28
Reduced g-C_3N_4	Pure water, O_2, 400 mg, λ≥420nm, 300	1700 $\mu M\ g^{-1}\ h^{-1}$	N/A	29

	W			
Br-H-g-C_3N_4	EDTA+water, O_2, λ>400 nm	1990 μM g^{-1} h^{-1}	Productivity decaying after 3 h of reaction	30
$Cu_2(OH)_2CO_3$/ g-C_3N_4	Water, O_2, λ>400 nm, 300 W	2472 μM g^{-1} h^{-1}	Productivity decaying after 6 h of reaction	31
Ti_3C_2/pores g-C_3N_4	Isopropanol+water, O_2, 100 mg, λ≥420nm, 300 W	3170 μM g^{-1} h^{-1}	3 h of cycling reaction	32
CoP/g-C_3N_4	Ethanol+water, O_2, 20 mg, λ≥400nm	3500 μM g^{-1} h^{-1}	N/A	33
Nv-g-C_3N_4	Ethanol+water, O_2, λ>400 nm, 250 W	4400 μM g^{-1} h^{-1}	Productivity decaying after 6 h of reaction	34
B-C_3N_4	Isopropanol+water, O_2, 50 mg, λ≥420nm, 300W	5740.5 μM g^{-1} h^{-1}	3 h of cycling reaction	35

Note S1. The concentration of excited states of the as-prepared B-CN, NS-CN, 3D-CN-C1, and 3D-CN-C2, respectively was roughly estimated by integrating the absorption intensity under different photo energy according to the the UV-vis absorption spectra (Figure S8) to be 1023K, 1052K, 1717K and 1982K (K is a constant), respectively. Although the precise calculation of the concentration of excited states is difficult, we hope that the result can still explain at a certain scientific fact. The higher concentrations of excited states for the deficient samples may provide more photoinduced charges to join in the photoredox reaction.

Note S2. EDD plots suggest the enrichment of electron density at the N sites. Obviously, the color changes to red near the uncoordinated N atoms, indicating that the electron density enhances around the sites and acting as active electron rich sites for photoreduction.

Note S3. In pristine C_3N_4, N1, N2 and N3 site present Fukui charge values of 0.016|e|, 0.011 |e| and N3 0.0012|e|, respectively. After introduction of C defects, these three N sites has

Fukui charge values of 1.29|e|, 1.08|e| and 0.17|e|. The tremendous manifold times enhancement in Fukui charges strongly demonstrate the boosted affinity of defect centres for superoxygen radical attack which is crucial for efficient photoreduction to H_2O_2.

Supplemental References

1. Kofuji, Y., Ohkita, S., Shiraishi, Y., Sakamoto, H., Ichikawa, S., Tanaka, S., and Hirai, T. (2017). ACS Sustain. Chem. Eng. *5*, 6478–6485.

2. Ou, H., Yang, P., Lin, L., Anpo, M., and Wang, X. (2017). Carbon nitride aerogels for the photoredox conversion of water. Angew. Chem. Int. Ed. *129*, 11045–11050.

3. Kofuji, Y., Isobe, Y., Shiraishi, Y., Sakamoto, H., Ichikawa, S., Tanaka, S., and Hirai, T. (2018). Hydrogen peroxide production on a carbon nitride-boron nitride-reduced graphene oxide hybrid photocatalyst under visible light. ChemCatChem *10*, 2070–2077.

4. Kofuji, Y., Ohkita, S., Shiraishi, Y., Sakamoto, H., Tanaka, S., Ichikawa, S., and Hirai, T. (2016). Graphitic carbon nitride doped with biphenyl diimide: efficient photocatalyst for hydrogen peroxide production from water and molecular oxygen by sunlight. ACS Catal. *6*, 7021–7029.

5. Fu, Y., Liu, C. A., Zhang, M., Zhu, C., Li, H., Wang, H., Song, Y., Huang, H., Liu, Y., and Kang, Z. (2018). Photocatalytic H_2O_2 and H_2 Generation from Living Chlorella vulgaris and Carbon Micro Particle Comodified g-C_3N_4. Adv. Energy Mater. *8*, 1802525.

6. Shiraishi, Y., Kanazawa, S., Sugano, Y., Tsukamoto, D., Sakamoto, H., Ichikawa, S., and Hirai, T. (2014). Highly selective production of hydrogen peroxide on graphitic carbon nitride (g-C_3N_4) photocatalyst activated by visible light. ACS Catal. *4*, 774–780.

7. Li, S., Dong, G., Hailili, R., Yang, L., Li, Y., Wang, F., Zeng, Y., and Wang, C. (2016). Effective photocatalytic H_2O_2 production under visible light irradiation at g-C_3N_4 modulated by carbon vacancies. Appl. Catal. B *190*, 26–35.

8. Shi, L., Yang, L., Zhou, W., Liu, Y., Yin, L., Hai, X., Song, H., and Ye, J. (2018). Photoassisted Construction of Holey Defective g-C_3N_4 Photocatalysts for Efficient Visible-Light-Driven H_2O_2 Production. Small *14*, 1703142.

9. Zhao, S., Zhao, X., Zhang, H., Li, J., and Zhu, Y. (2017). Covalent combination of polyoxometalate and graphitic carbon nitride for light-driven hydrogen peroxide production. Nano Energy *35*, 405–414.

10. Chen, L., Wang, L., Wan, Y., Zhang, Y., Qi, Z., Wu, X., and Xu, H. (2020). Acetylene and diacetylene functionalized covalent triazine frameworks as metal-free photocatalysts for hydrogen peroxide production: a new two-electron water oxidation pathway. Adv. Mater. *32*, 1904433.

11. Teng, Z., Zhang, Q., Yang, H., Kato, K., Yang, W., Lu, Y. R., Liu, S., Wang, C., Yamakata, A., Su, C., et al. (2021). Atomically dispersed antimony on carbon nitride for the artificial photosynthesis of hydrogen peroxide. Nat. Catal. 4, 374–384.

12. Shiraishi, Y., Kofuji, Y., Sakamoto, H., Tanaka, S., Ichikawa, S., and Hirai, T. (2015). Effects of Surface Defects on Photocatalytic H_2O_2 Production by Mesoporous Graphitic Carbon Nitride under Visible Light Irradiation. ACS Catal. 5, 3058-3066.

13. Thakur, S., Kshetri, T., Kim, N. H., and Lee, J. H. (2017). Sunlight-driven sustainable production of hydrogen peroxide using a CdS-graphene hybrid photocatalyst. J Catal. *345*, 78–86.

14. Wang, R., Zhang, X., Li, F., Cao, D., Pu, M., Han, D., Yang, J., and Xiang, X. (2018). Energy-level dependent H_2O_2 production on metal-free, carbon-content tunable carbon nitride photocatalysts. J. Energy Chem. *27*, 343–350.

15. Zhao, S., Guo, T., Li, X., Xu, T., Yang, B., and Zhao, X. (2018). Carbon nanotubes covalent combined with graphitic carbon nitride for photocatalytic hydrogen peroxide production under visible light. Appl. Catal. B *224*, 725–732.

16. Chang, X., Yang, J., Han, D., Zhang, B., Xiang, X., and He, J. (2018). Enhancing light-driven production of hydrogen peroxide by anchoring Au onto C_3N_4 catalysts. Catalysts *8*, 147.

17. Moon, G. H., Fujitsuka, M., Kim, S., Majima, T., Wang, X., and Choi, W. (2017). Eco-friendly photochemical production of H_2O_2 through O_2 reduction over carbon nitride frameworks incorporated with multiple heteroelements. ACS Catal. *7*, 2886–2895.

18. Tian, J., Wu, T., Wang, D., Pei, Y., Qiao, M., and Zong, B. (2019). One-pot synthesis of potassium and phosphorus-doped carbon nitride catalyst derived from urea for highly efficient visible light-driven hydrogen peroxide production. Catal. Today 330, 171–178.

19. Shiraishi, Y., Kanazawa, S., Kofuji, Y., Sakamoto, H., Ichikawa, S., Tanaka, S., and Hirai, T. (2014). Sunlight-driven hydrogen peroxide production from water and molecular oxygen by metal-free photocatalysts. Angew. Chem. Int. Ed. *53*, 13454–13459.

20. Cai, J., Huang, J., Wang, S., Iocozzia, J., Sun, Z., Sun, J., Yang, Y., Lai, Y., and Lin, Z. (2019). Crafting Mussel-Inspired Metal Nanoparticle-Decorated Ultrathin Graphitic Carbon Nitride for the Degradation of Chemical Pollutants and Production of Chemical Resources. Adv. Mater. *31*, 1806314.

21. Kim, H. I., Kwon, O. S., Kim, S., Choi, W., & Kim, J. H. (2016). Harnessing low energy photons (635 nm) for the production of H_2O_2 using upconversion nanohybrid photocatalysts.Energy Environ. Sci. *9*, 1063–1073.

22. Wei, Z., Liu, M., Zhang, Z., Yao, W., Tan, H., and Zhu, Y. (2018). Efficient visible-light-driven selective oxygen reduction to hydrogen peroxide by oxygen-enriched graphitic carbon nitride polymers. Energy Environ. Sci. *11*, 2581–2589.

23. Yang, L., Dong, G., Jacobs, D. L., Wang, Y., Zang, L., and Wang, C. (2017). Two-channel photocatalytic production of H_2O_2 over g-C_3N_4 nanosheets modified with perylene imides. J Catal. *352*, 274–281.

24. Qu, X., Hu, S., Bai, J., Li, P., Lu, G., and Kang, X. (2018). Synthesis of band gap-tunable alkali metal modified graphitic carbon nitride with outstanding photocatalytic H_2O_2 production ability via molten salt method. J. Mater. Sci. Technol. *34*, 1932–1938.

25. Kofuji, Y., Isobe, Y., Shiraishi, Y., Sakamoto, H., Tanaka, S., Ichikawa, S., and Hirai, T. (2016). Carbon nitride-aromatic diimide-graphene nanohybrids: metal-free photocatalysts for solar-to-hydrogen peroxide energy conversion with 0.2% efficiency. J. Am. Chem. Soc. *138*, 10019–10025

26. Hu, S., Qu, X., Li, P., Wang, F., Li, Q., Song, L., Zhao, Y., and Kang, X. (2018). Photocatalytic oxygen reduction to hydrogen peroxide over copper doped graphitic carbon nitride hollow microsphere: the effect of Cu (I)-N active sites. Chem. Eng. J. *334*, 410–418.

27. Qu, X., Hu, S., Li, P., Li, Z., Wang, H., Ma, H., and Li, W. (2018). The effect of embedding N vacancies into g-C_3N_4 on the photocatalytic H_2O_2 production ability via H_2 plasma treatment. Diamond Relat. Mater. *86*, 159–166.

28. Bai, J., Sun, Y., Li, M., Yang, L., and Li, J. (2018). The effect of phosphate modification on the photocatalytic H_2O_2 production ability of g-C_3N_4 catalyst prepared via acid-hydrothermal post-treatment. Diamond Relat. Mater. *87*, 19.

29. Zhu, Z., Pan, H., Murugananthan, M., Gong, J., and Zhang, Y. (2018). Visible light-driven photocatalytically active g-C_3N_4 material for enhanced generation of H_2O_2. Appl. Catal. B: Environ. *232*, 19.

30. Zhang, C., Bai, J., Ma, L., Lv, Y., Wang, F., Zhang, X., Yuan, X., and Hu, S. (2018). Synthesis of halogen doped graphite carbon nitride nanorods with outstanding photocatalytic H_2O_2 production ability via saturated NH_4X (X= Cl, Br) solution-hydrothermal post-treatment. Diamond Relat. Mater. *87*, 215–222.

31. Li, Z., Xiong, N., and Gu, G. (2019). Fabrication of a full-spectrum-response $Cu_2(OH)_2CO_3$/g-C_3N_4 heterojunction catalyst with outstanding photocatalytic H_2O_2 production performance via a self-sacrificial method. Dalton Trans. *48*, 182–189.

32. Yang, Y., Zeng, Z., Zeng, G., Huang, D., Xiao, R., Zhang, C., Zhou, C., Xiong, W., Wang, W., Cheng, M., et al. (2019). Ti_3C_2 Mxene/porous g-C_3N_4 interfacial Schottky junction for boosting spatial charge separation in photocatalytic H_2O_2 production. Appl. Catal. B: Environ. *258*, 117956.

33. Peng, Y., Wang, L., Liu, Y., Chen, H., Lei, J., and Zhang, J. (2017). Visible-light-driven photocatalytic H_2O_2 production on g-C_3N_4 loaded with CoP as a noble metal free cocatalyst. Eur. J. Inorg. Chem. *17*, 4797–4802.

34. Li, X., Zhang, J., Zhou, F., Zhang, H., Bai, J., Wang, Y., and Wang, H. (2018). Preparation of N-vacancy-doped g-C_3N_4 with outstanding photocatalytic H_2O_2 production ability by dielectric barrier discharge plasma treatment. Chin. J. Catal. *39*, 1090–1098.

35. Feng, C., Tang, L., Deng, Y., Wang, J., Luo, J., Liu, Y., Ouyang, X., Yang, H., Yu, J., and Wang, J. (2020). Synthesis of leaf-vein-like g-C_3N_4 with tunable band structures and charge transfer properties for selective photocatalytic H_2O_2 evolution. Adv. Funct. Mater. *30*, 2001922.

Chapter 4

3DOM-Pt/Bi_2MoO_6/TiO_2 for photo/electro/thermal/catalytic applications

In this chapter, a ternary three-dimensional ordered macroporous (3DOM) heterojuncted nanocomposites (3DOM-Pt/Bi_2MoO_6/TiO_2) were designed and synthesized as multifunctional platform for photocatalytic dye degradation, photoelectrocatalytic (PEC) water splitting and thermal-catalytic toluene decomposition with high performance. The detailed mechanisms for the increased catalytic performance were thoroughly revealed. Specifically, my contribution for the work is that the fabrication of the new 3DOM-Pt/Bi_2MoO_6/TiO_2 structure, which can efficiently exert the advantages of 3DOM structure and the active materials (Pt and Bi_2MoO_6). Moreover, I also conducted a series of materials characterization (XRD, XPS, SEM, TEM, PEC and UV-vis et al.) and the discussion of the experimental results. The major achievement for the work is construction of the ternary 3DOM photocatalyst model, which can inspire some new ideas in synthesizing other 3DOM photocatalysts.

(This work has been published on **Advanced Materials Interfaces 2020, 2001879** by Yang Ding et al.)

A novel 3DOM TiO_2 based multifunctional photocatalytic and catalytic platform for energy regeneration and pollutants degradation

Yang Ding[1,2], Lina Huang[1,2,3], Tarek Barakat[1,2], and Bao-Lian Su[1,2,4]*

[1]Laboratory of Inorganic Materials Chemistry (CMI), University of Namur, 61 rue de Bruxelles, B5000, Namur, Belgium. (E-mail: bao-lian.su@unamur.be)

[2] Namur Institute of Structured Matter (NISM), University of Namur, 61 rue de Bruxelles, B-5000, Namur, Belgium.

[3] Guangdong Provincial Key Laboratory of Durability for Marine Civil Engineering, Shenzhen Durability Center for Civil Engineering, College of Civil Engineering, Shenzhen University, 518060, Shenzhen Guangdong, China.

[4] State Key Laboratory of Advanced Technology for Materials Synthesis and Processing, Wuhan University of Technology, 122, Luoshi Road, 430070 Wuhan, Hubei, China.

Abstract: The ternary three-dimensional ordered macroporous (3DOM) heterojuncted nanocomposites (3DOM-$Pt/Bi_2MoO_6/TiO_2$) were designed and synthesized as multifunctional platform for photocatalytic dye degradation, photoelectrocatalytic (PEC) water splitting and thermal-catalytic toluene decomposition with high performance. A series of structural, optical and electronic characterizations demonstrated that the remarkably improved photocatalytic degradation and PEC water splitting activities were attributed to the combined effects of enhanced light harvesting, abundant reactive sites, facile reactants transfer and efficient charges-holes pair separation. Through optimizing the loading amounts of Pt and Bi_2MoO_6, it was found that the 1%Pt/10%Bi_2MoO_6/TiO_2 nanocomposite exhibited the highest photocatalytic RhB degradation rate and PEC water splitting activity, which were 10 and 2.2 times higher than that of the titania photonic crystal (PC-TiO_2) photocatalyst, respectively. Our work clearly illustrated that the ternary photocatalyst with 3DOM structure and intimate heterostructure can significantly facilitate the transfer of reaction intermediates and the separation of photogenerated carriers. Considering its unique 3DOM structure and excellent photocatalytic/PEC performances, the ternary nanocomposite has been used in catalytic toluene decomposition and inspiringly showed high efficiency, being very promising in thermocatalytic applications. This work provides new solutions in developing new ternary nanocomposites for versatile applications in photocatalytic, photoelectrochemical and catalytic fields.

Keywords: 3DOM, ternary, photocatalysis, photoelectrocatalysis, thermocatalysis

1. Introduction

The three-dimensionally ordered macroporous (3DOM) materials have attracted great interest in photocatalysis and photoelectrocatalysis fields because of their characteristic slow photon effect,[1-6] which could largely increase the residence time of the incident light with certain wavelengths in the 3DOM structure, and significantly enhance the light harvesting efficiency. In addition to the slow photon effect, the unique 3DOM structure has an open interconnected porous network, facilitating the diffusion of molecules and providing the sufficient active sites, both being quite favourable for photocatalytic reaction process. As an important semiconductor material, TiO_2 has been extensively studied as the one of most promising photocatalytic materials because of its good stability, low-cost and environment-friendly. However, the wide electronic band gap (about 3.2 eV) restricts its utilization in the field of visible light photocatalysis.[7-9] However, the high recombination rate of photogenerated electron-hole pairs leads to its low photocatalytic efficiency. Up to now, many strategies have been developed to solve these shortcomings and improve the photocatalytic efficiency. Coupling narrow bandgap semiconductors, such as CdS, CuO and BiOBr is one of straightforward choices. The formed binary nanocomposites have not only the increased visible light harvesting but also favors the separation of the photogenerated carriers.[10-20] In addition, depositing noble metal such as Pt and Au on the surface of semiconductor photocatalyst could also improve their photocatalytic activity because the outstanding conductivity of noble metal facilitates the transfer of photogenerated carriers and the surface plasmon resonance (SPR) effect of noble metal further enhances the visible light harvesting.

Monoclinic bismuth molybdate (Bi_2MoO_6) has drawn important attention in photoelectric field because of its excellent chemical stability and high photo-response ability, and also demonstrated to be a promising visible light photocatalyst for its moderate photocatalytic activity.[21-23] Moreover, Bi_2MoO_6 is widely used as a photosensitizer due to its narrow band gap. Many works have been conducted to couple Bi_2MoO_6 with wide bandgap semiconductors such as ZnO and WO_3, the obtained composites presented highly enhanced visible light photocatalytic activity,[13-15] indicating that constructing the narrow and broad bandgap semiconductors composite is an efficient way to promote the photocatalytic activity.

In order to benefit from the advantages of 3DOM structure, composite system and excellent conductivity of noble metal, the innovative ternary 3DOM nanocomposites ($Pt/Bi_2MoO_6/PC-TiO_2$) were designed and synthesized in this work. A series of photocatalytic activity tests showed that the $1\%Pt/10\%Bi_2MoO_6/TiO_2$ nanocomposite exhibited the highest photocatalytic RhB degradation rate and PEC water splitting activity, which were 10 and 2.2 times higher than that of the titania photonic crystal ($PC-TiO_2$) catalyst, respectively. Thoroughly structural, morphology and energy band studies suggested that the ternary photocatalyst with 3DOM structure and intimate heterostructure can significantly facilitate the transfer of reaction intermediates and the separation of photogenerated carriers. Considering its unique 3DOM structure and excellent photocatalytic/PEC performances, the volatile organic compounds (VOC) decomposition using toluene as VOC probe molecule by the ternary nanocomposites was also conducted. More intriguingly, the ternary nanocomposites presented high activity in thermocatalytic toluene degradation. This work displays the potential to construct a multifunctional platform for photocatalytic, photoelectrocatalytic and thermocatalytic applications.

2. Experimental

All the chemical reagents were purchased from Aldrich and used without further purification. Deionized water was used throughout this work.

2.1 Synthesis of polystyrene (PS) spheres

Polystyrene (PS) spheres were prepared by an emulsion polymerization method.[12] Typically, 20 mL of styrene was washed three times by a solution of NaOH (1 M) to remove the polymerization inhibitor, and then mixed with 300 mL of deionized water in a three-neck flask. Meanwhile, 0.3 g of $K_2S_2O_8$ was also added to the flask to induce polymerization. The mixture was stirred at 80°C for 4h under N_2 atmosphere. After stirring, the milky white mixture was cooled to room temperature. Finally the PS colloidal spheres were obtained via drying the mixture at 40°C.

2.2 Synthesis of $PC-TiO_2$

The preparation of titania photonic crystal ($PC-TiO_2$) was achieved via a templating method. Firstly, the self-assembled PS spheres were deposited onto a filter paper in a Buchner funnel under vacuum. Then titanium isopropoxide was slowly added to completely cover the PS spheres whilst under vacuum such that it occupied the voids inside the PS assembly. The precursor–template mixture was air dried for 12 h and subsequently calcined in oxygen at 550°C for 5 h at a heating rate of 4°C min^{-1} to obtain PC-TiO_2 with an inverse opal structure.

2.3 Synthesis of Bi_2MoO_6/PC-TiO_2

The typical binary 10%Bi_2MoO_6/PC-TiO_2 (denoted as 10B-T) composite was synthesized through a deposition-precipitation method. PC-TiO_2 (9 mmol), $(NH_4)_6MO_7O_{24}.4H_2O$ (0.15 mmol), $Bi(NO_3)_3.2H_2O$ (2 mmol), CTAB(0.1g) and DMF (15 mL) were loaded into a 50mL three-neck flask with stirring at 80°C for 60 min. After the reaction, the mixture was cooled naturally to room temperature. The precipitate was collected by centrifuging and washing three times with mixture of ethanol and deionized water. Finally, the sample was dried at 60°C for 1h. A series of binary composites such as 1%Bi_2MoO_6/PC-TiO_2 (1B-T), 5%Bi_2MoO_6/PC-TiO_2 (5B-T) and 20%Bi_2MoO_6/PC-TiO_2 (20B-T) were also prepared by the same method. In addition, the pure Bi_2MoO_6 sample used as a reference was synthesized by the same procedure without adding PC-TiO_2.

2.4 Synthesis of ternary Pt/Bi_2MoO_6/PC-TiO_2 composites

The typical ternary Pt/Bi_2MoO_6/PC-TiO_2 nanocomposite containing 1% Pt (1P-10B-T) was prepared by impregnation of the as-prepared 10B-T (0.2 g) in 20 ml of H_2PtCl_6 (0.05 gmL^{-1}) aqueous solution. The mixture was stirred for 5min, then 2mL of freshly prepared $NaBH_4$ aqueous solution (2 mg mL^{-1}, containing 0.5 M NaOH) was rapidly added into the mixture with vigorous stirring at room temperature. After 1 h, another 2 ml of freshly prepared $NaBH_4$ aqueous solution was further added into the mixture, and kept under stirring for 2 h. The precipitate after centrifugation was washed with deionized water for three times and dried at 40°C for 0.5 h in a vacuum drying oven. The 1P-10B-T photocatalyst was thus obtained. The series of ternary photocatalysts with different Pt loading content were prepared by adding H_2PtCl_6 aqueous solution with different concentrations (0.005, 0.025, to 0.075 gmL^{-1}). The obtained samples were labeled as 0.1P-10B-T, 0.5P-10B-T and 1.5P-10B-T for 0.1%, 0.5% and 1.5% Pt loading, respectively. Similarly, 1Pt/10Bi_2MoO_6/P25 used as reference was also prepared by the same method and the obtained sample was denoted as 1P-10B-P25. The detailed procedure for the fabrication of ternary Pt/Bi_2MoO_6/PC-TiO_2 nanocomposites is illustrated in **Scheme** 1.

2.5 Materials Characterization

Powder X-ray diffraction (XRD) patterns of all the samples were recorded on a PANalytical X'pert Pro with Cu Ka radiation (k = 0.15405 A, 45 kV, 30 mA), with a scanning rate and range of 4 degree/min and 20-80, respectively. Textural properties of the materials were studied using nitrogen adsorption-desorption at -196°C using a Micromeritics Tristar 3000 with prior degassing process at 150 for 6h. The morphological properties, energy dispersive X-ray spectroscopy (EDX) and elements mapping patterns of the samples were obtained by scanning electron microscopy (SEM) (JEOL-7500F), operated at 200 kV. The transmission electron microscopy (TEM) characterizations were preformed by the Tecnai 10 instrument. X-ray photoelectron spectroscopy analysis was performed on a K-Alpha™ + X-ray photoelectron spectrometer (XPS). The binding energy for the C (1s) peak at 284.9 eV (relative to adventitious carbon from the XPS instrument itself) was used as a reference. The UV-vis absorbance spectra were acquired by a UV-vis spectrophotometer in the range of 200-700 nm. Photoluminescence properties of the samples were investigated by Perkin Elmer LS45 spectrometer.

2.6 Photocatalytic activity evaluation using degradation of RhB as probe reaction

Photocatalytic activity evaluation tests were conducted under visible light irradiation (400-800 nm) using 6 neon lamps of 18 W, the luminous power of each lamp was 1250 lm. The reaction temperature was maintained at room temperature. In each experiment, 20 mg of photocatalyst was added in 50 mL of reaction solution with an initial concentration of 10 ppm of RhB used as probe molecule. The suspension was poured into a beaker, put into the reactor and uniformly stirred in the dark ambient for 120 min to ensure adsorption/desorption equilibrium before the visible light irradiation. During irradiation, 2 mL of the suspension was picked up and centrifuged to filter out the photocatalyst at a given time interval for subsequent RhB concentration analysis, a UV-Vis spectrometer was used to determine the concentrations.

2.7 Photoelectrochemical measurements

The photoelectrochemical measurement was carried out on a conventional three-electrode cell by using computer-controlled electrochemical workstation (CHI 660E).[7] Typically, 5 mg sample, 20 μL water and 20 μL nafion solution were loaded into a beaker and ultrasonicated to form the uniform suspension. Then, 10 μL of the mixed solution was deposited on the conductive slide of ITO glass (1.0 × 1.0 cm) and dried in a vacuum oven. A three-electrode system consisting of an saturated calomel electrode (SCE), an ITO glass electrode and a Pt plate was used as the reference, working and counter electrodes, respectively. 0.1 M Na_2SO_4 solution was adopted as the electrolyte in this three-electrode system. The current-time (I-t) curves were obtained at the open-circuit potential of 0.6 V. The Mott-Schottky plot and electrochemical impendence spectroscopy (EIS) were collected under the same conditions without the Xe lamp irradiation. For the PEC water splitting characterization, the linear sweep voltammetry with a scanning rate of 50 mV s^{-1} was carried out under AM 1.5G illumination (100 mW cm^{-2}) by using a simulated sunlight source. The collected potentials versus SCE electrode were converted to the reversible hydrogen electrode (RHE) according to the following formula: E (RHE) = 0.242 + 0.059 pH + E(SCE).[17]

2.8 Catalytic tests for toluene degradation

Toluene complete oxidation reaction as probe reaction to evaluate the catalytic performance of our materials for volatile organic compound degradation was conducted in a fixed-bed reactor (0.9 cm inner diameter) at atmospheric pressure. A thermal detector connected to a PID temperature controller was placed on side of the catalyst bed. The toluene oxidation reaction was performed using an air stream with a total flow rate of 100 mL/ min passing through liquid toluene at 333 K, and the resulting mixture of Air/toluene with a 1000 ppm toluene amount passed over 100 mg of catalyst. All products were analyzed via gas chromatography (GC) through a 12-ft Porapak-Q column, the gas chromatography was equipped with a thermal conductivity detector (TCD). According to gas chromatography, all reacted toluene was converted into CO_2. The conversion is calculated using the following formula[46]:

$$Conv\% = 100 \times \frac{(CO_{2(formed)})}{CO_{2(formed)} + 7 \times (Toluene_{(remained)})}\%$$

3. Results and discussion

3.1 Structure and morphology

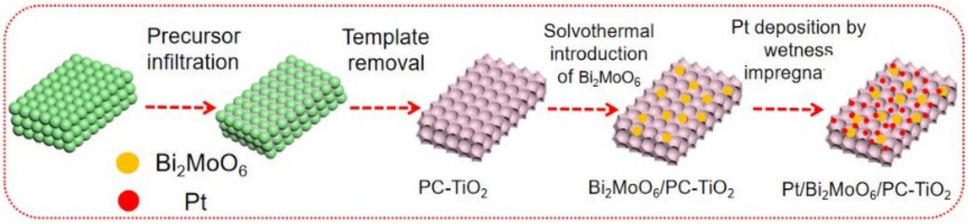

Scheme. 1 The detailed procedure for the fabrication of ternary Pt/Bi_2MoO_6/PC-TiO_2 nanocomposites.

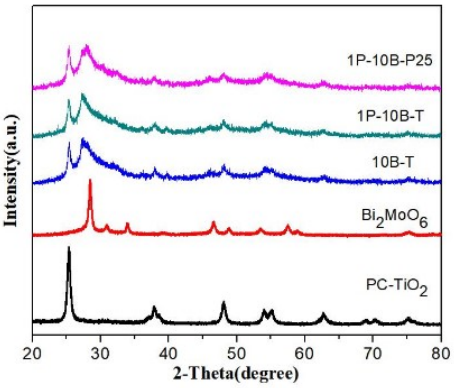

Figure. 1 X-ray diffraction patterns of the as-prepared PC-TiO_2 ,Bi_2MoO_6, 10B-T, 1P-10B-T and 1P-10B-P25 samples.

XRD patterns of the as-prepared photocatalysts are shown in Figure 1. For the pure PC-TiO_2, the diffraction peaks at 25.3°, 37.9°, 48.0°, 54.6° and 62.8° can be well indexed to the crystal planes of (101), (004), (200), (211), and (204), respectively (JCPDS 14-0688), which indicates a pure anatase phase.[24-28] The peaks of Bi_2MoO_6 sample correspond to the monoclinic scheelite phase (JCPDS 14-0688).[22] These two diffraction profiles indicate that both PC-TiO_2 and Bi_2MoO_6 samples are highly crystalline. For the binary 10B-T composite, the peaks from both PC-TiO_2 and Bi_2MoO_6 are present. The diffraction peaks of ternary 1P-10B-T and 1P-10B-P25 samples are similar to that of 10B-T, no peak of Pt is found, suggesting the low loading amount of Pt precursor.[8] Especially, the peak at 28.2° from 10B-T, 1P-10B-T and 1P-10B-P25 samples is much weaker and broader than that of the pure Bi_2MoO_6, indicating the decreased particle size and low amount of Bi_2MoO_6 in these nanocomposites. Moreover, the slightly shifted peak at 25.3° from these three composite samples is ascribed to the intimate contact between PC-TiO_2 and Bi_2MoO_6 and the heterojunction is formed.[26]

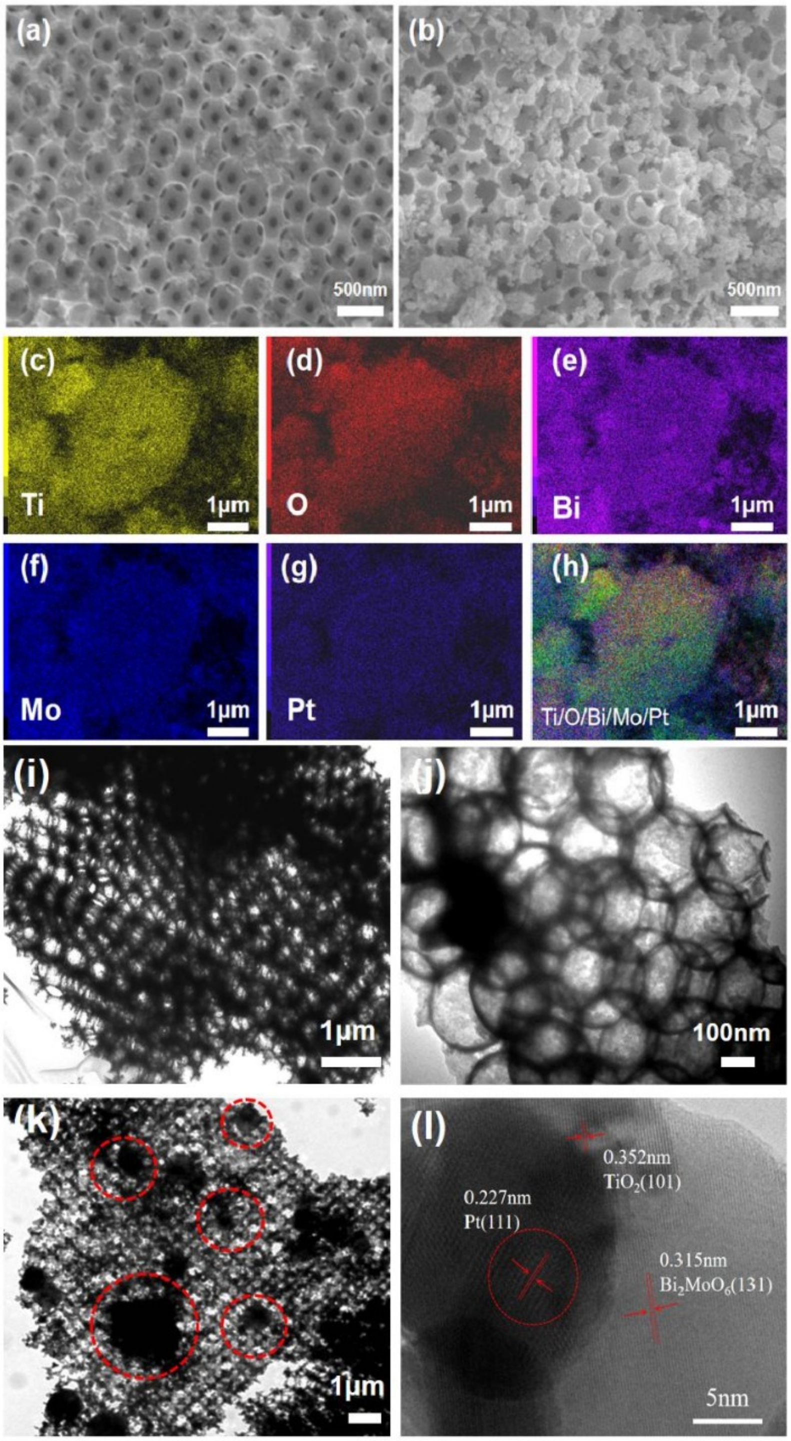

Figure. 2 SEM images of (a) PC-TiO_2 and (b) 1P-10B-T samples. (c-h) Elements mapping patterns of 1P-10B-T photocatalyst. (i-j) TEM images of the as-synthesized PC-TiO_2. (k) TEM and (l) HR-TEM images of 1P-10B-T photocatalyst.

The morphologies of as-prepared samples were characterized by SEM. **Figure** 2a shows a highly ordered 3DOM structure with interconnected pore of PC-TiO_2 and the average large void size is about 300 nm. This unique 3DOM structure can maintain the reflectance property at different incident light angles and decrease the effect of random orientation during the photocatalytic reaction when the solution is constantly stirred. Moreover, the 3DOM structure can also facilitate the diffusion of molecules and provide sufficient reactive sites, both are beneficial to the photocatalytic reaction process.[29-33] **Figure S1** shows a series of binary nanocomposites with various Bi_2MoO_6 amounts. The highly ordered periodic structures are well maintained after loading Bi_2MoO_6 and some irregular nanoparticles adhere on the surface of PC-TiO_2, which is in good agreement with XRD results. The morphology of pure Bi_2MoO_6 sample was also studied and presented in **Figure** S2. The pure Bi_2MoO_6 sample exhibits agglomerated structure and the large block consists of numerous spherical particles with the size about 50 nm. **Figure** 2b presents the SEM image of the typical 1P-10B-T nanocomposite. Similar to the binary nanocomposite samples, the 3DOM structure of 1P-10B-T is well kept and the irregular Bi_2MoO_6 nanoparticles decorate on the surface of the macropores. EDX pattern (**Figure** S3) suggests that the presence of Pt, Ti, Bi, Mo, and O elements in 1P-10B-T nanocomposite, demonstrating that the Pt and Bi_2MoO_6 are successfully combined with PC-TiO_2. The elements mapping images of 1P-10B-T in **Figure** 2c-h reveal the uniform distribution of Ti, O, Bi, Mo and Pt atoms in 1P-10B-T sample. The TEM images of PC-TiO_2 sample are shown in **Figure** 2i-j. The ordered macropores with size about 300nm can be clearly observed, which is consistent with the SEM result. **Figure** 2k depicts the low magnification TEM image of the 1P-10B-T catalyst. It is found that the 1P-10B-T sample maintains well uniform 3DOM structure and the Bi_2MoO_6 nanoparticles are (in the red circle) decorate on the 3DOM skeleton. The HRTEM images of the 1P-10B-T are depicted in **Figure** 2l and **Figure S4.** The existence of Pt and Bi_2MoO_6 in the ternary composite is confirmed through measuring lattice spacing corresponding to the Pt (111) and Bi_2MoO_6 (131) planes. The overlapping of lattices fringes planes of TiO_2, Pt and Bi_2MoO_6 indicate strong bonding interactions among the three components.[26]

3.2 Textural properties

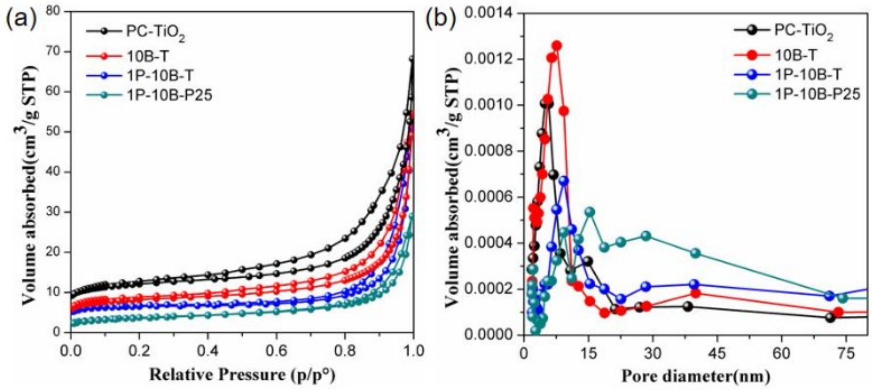

Figure 3 (a) N_2 adsorption–desorption isotherms and (b) pore size distributions of PC-TiO_2, 10B-T, 1P-10B-T and 1P-10B-P25 samples.

Figure 3a, b present the nitrogen adsorption-desorption isotherms and pore size distribution curves of PC-TiO_2, 10B-T, 1P-10B-T and 1P-10B-P25 samples. All the N_2 adsorption–desorption curves show the type II isotherms.[34-38] For PC-TiO_2, the pore size distribution plot calculated by the Barrett–Joyner–Halenda (BJH) method shows a narrow pore size distribution centred at 8 nm, resulting from the aggregation of TiO_2 nanoparticles. When the Bi_2MoO_6 was loaded on PC-TiO_2, one sharp peak and a very broad peak centred at 9 and 40 nm, respectively were observed. The pore size at 9 nm originates from the aggregation of TiO_2 nanoparticles while pores at 40 nm come from the aggregation of Bi_2MoO_6 nanoparticles. The pore distribution of ternary 1P-10B-T is similar to that of binary 10B-T, suggesting that the introduction of tiny Pt has no major influence on its porosity. It should be mentioned that the mesoporous structure of 1P-10B-P25 may be derived from the random interstitial holes formed by aggregating of TiO_2 and Bi_2MoO_6 particles. The detailed BET specific surface area, average pore size and pore volume of the series of samples are summarized in **Table** S1. From the table, it is seen that the specific surface areas gradually decreases with increasing the amounts of Bi_2MoO_6, which is attributed to the occupation of Bi_2MoO_6 in the macropores of PC-TiO_2. When Pt is further introduced into Bi_2MoO_6/PC-TiO_2, the relevant parameters of the pore almost no change due to the tiny amounts of Pt.

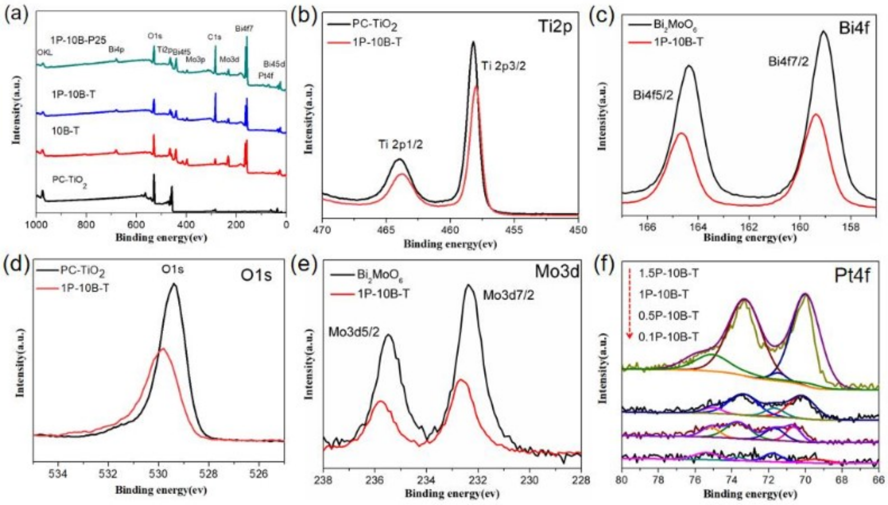

Figure 4 (a) XPS survey spectra of PC-TiO_2, 10B-T, 1P-10B-T and 1P-10B-P25 samples and high-resolution XPS spectra of (b) Ti 2p, (c) Bi 4f, (d) O 1s, (e) Mo 3d and (f) Pt 4f of the as-prepared samples.

The specific chemical environments and oxidation states of the elements in as-prepared samples were characterized using XPS. **Figure** 4a shows the XPS spectra of PC-TiO_2, 10B-T, 1P-10B-T and 1P-10B-P25 samples. The different spectral regions corresponding to different elements can be clearly recognized. **Figure** 4b presents two bands with binding energies of 458.8 and 464.5 eV assigned to Ti $2p_{3/2}$ and Ti $2p_{1/2}$, respectively and corresponding to Ti^{4+} in pure PC-TiO_2.[8] Compared with PC-TiO_2, a red shift of 0.2 eV to a lower binding energy in the peak positions of 1P-10B-T (458.6 and 464.3 eV) is clearly observed, illustrating that the charge transfer between Bi_2MoO_6 and TiO_2 very probably occurs.[16-17] For the high resolution Bi_{4f} spectra of Bi_2MoO_6 sample (**Figure** 4c), the two peaks located at 164.2 and 158.9 eV are attributed to the orbit of $Bi4f_{5/2}$ and $Bi7f_{7/2}$, respectively, corresponding to the characteristic binding energy values of Bi^{+3}.[21] A clear shift of 0.3 eV to a higher binding energy of the peak locations of Bi for 1P-10B-T further demonstrates that electron transfer between Bi_2MoO_6 and PC-TiO_2 could occur.[17] Similar to the Ti 2p and Bi 4f, the high-resolution XPS spectra of O 1s and Mo 3d for ternary 1P-10B-T exhibit the shift of 0.31 eV and 0.22 eV to high energy compared with that of pure PC-TiO_2 and Bi_2MoO_6, respectively. Moreover, the peak intensities of Ti 2p, O 1s, Bi 4f and Mo 3d for ternary 1P-10B-T are reduced compared with that of pure samples. All the results strongly indicate that the intimate interaction between Bi_2MoO_6 and PC-TiO_2 in 1P-10B-T nanocomposite and the heterojunction is generated. The Pt 4f high solution spectra of the four ternary samples are shown in **Figure** 4f. It is observed that 1P-10B-T sample has four peaks at 70.2, 71.7, 73.7, and 75.2 eV for Pt 4f. The peaks at 70.2 and 73.7 eV belong to metallic Pt^0 states of Pt $4f_{7/2}$ and Pt $4f_{5/2}$, respectively.[21] The peaks of Pt $4f_{7/2}$ and Pt $4f_{5/2}$ located at 71.7 and 75.2 eV correspond to Pt^{2+} bound to oxygen, respectively. These results confirm the coexistence of metallic Pt^0 and oxidized Pt^{2+} in 0.1P-10B-T. 0.1P-10B-T, 0.5P-10B-T and 1.5P-10B-T samples. The reason for the coexistence of metallic Pt^0 and oxidized Pt^{2+} may be due to the slow nucleation speed of Pt nanocrystallites at the low concentration, so the partially Pt^{2+} was formed. The above results are also in good agreement with previous reports.[39-42] It is worth noticing that oxidized Pt^{2+} represents only a small portion of total Pt and Pt is mainly present in Pt^0 form in these ternary samples.

3.3 Photoelectric properties

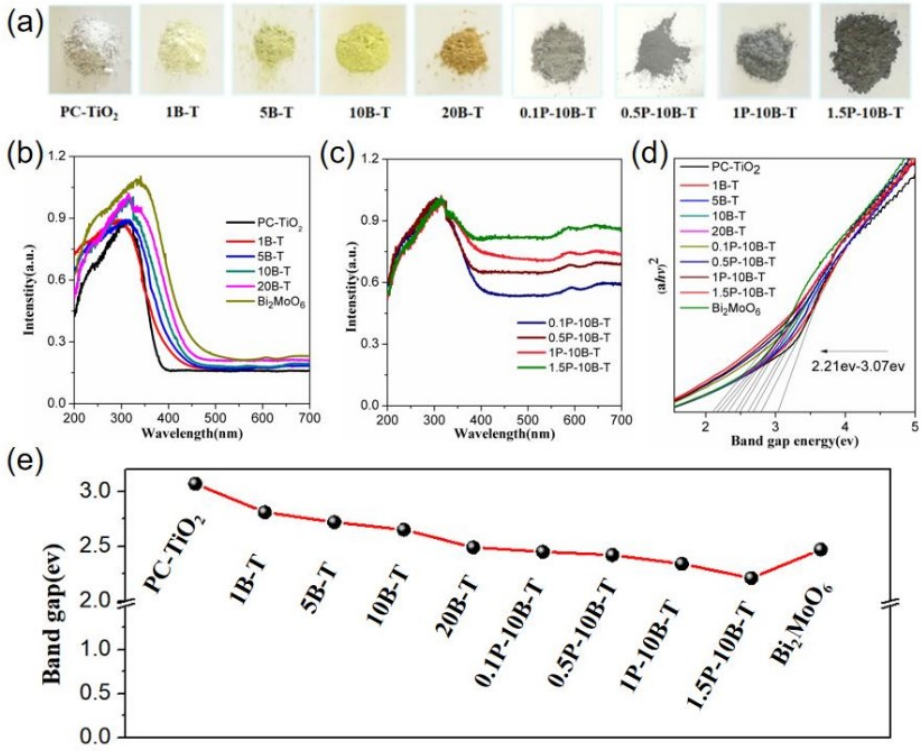

Figure 5 (a) Photographs of as-prepared samples, (b,c) UV-vis diffuse absorbance spectra and (d) the plot of $(\alpha h\nu)^2$ versus bandgap energy of as-prepared photocatalysts. (e) The electronic energy band gaps of as-prepared samples.

Figure 5a presents the photographs of the as-prepared photocatalysts under sun light. Compared with $PC\text{-}TiO_2$ sample, the obtained $Bi_2MoO_6/PC\text{-}TiO_2$ powders show a gradual color evolution from pale yellow to brown with increasing molar percentages of Bi_2MoO_6, implying their gradually enhanced visible light absorption. From the UV-vis absorption spectra in **Figure** 5b, the visible light absorption edges of the binary composites are red shifted with the molar percentage of Bi_2MoO_6 from 1 to 20%, indicating that the Bi_2MoO_6 can serve as a photosensitizer to promote the visible light harvesting of the Bi_2MoO_6/PC-TiO_2 nanocomposites. The pure Bi_2MoO_6 sample shows an absorption edge at around 490 nm, which could be responsible for any potential visible-light induced photocatalytic activity. As the Pt is further introduced into the binary nanocomposite, the visible light absorption is further improved (**Figure** 5c). The small peak located at 580 nm belonging to the surface plasmon resonance of Pt nanoparticles is well observed.[24] With increasing Pt content, the gray color of ternary nanocomposites becomes more and more intense and visible light absorption more and more enhanced, which favors for the enhanced photocatalytic activity. The band gap energy can be calculated from the Tauc's plots by the equation $\alpha h\nu = A(h\nu\text{-}Eg)^{1/2}$, where the a, h, A, m and Eg are the absorption coefficient near the absorption edge, the Planck constant, light frequency and the absorption band gap energy, respectively.[30-33] Plots of $(\alpha h\nu)^2$ versus $h\nu$ of the as-prepared samples are shown in **Figure** 5d. The band gaps are estimated to be 3.07 and 2.34 eV for PC-TiO_2 and 1P-10B-T, respectively. The calculated electronic energy band gap values for all the photocatalysts are listed in **Figure** 5e and **Table** S2. It can be obviously found that the introduction of Bi_2MoO_6 and Pt can effectively reduce the band gap of PC-TiO_2 and improve its visible light harvesting ability.

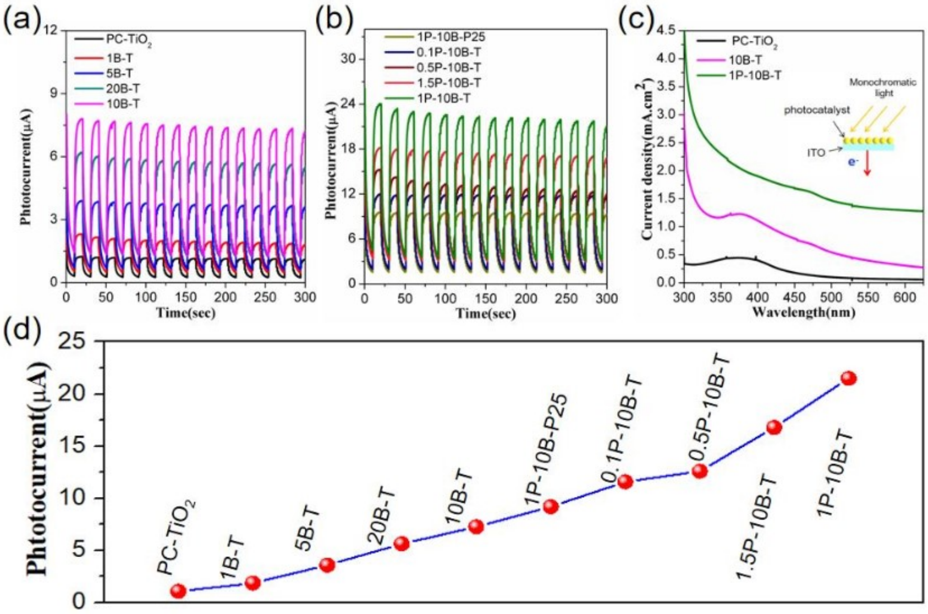

Figure. 6 (a,b) Photocurrent-time (I-t) curves (c) Photocurrents at different monochromatic light irradiation of as-prepared samples.(d) The photocurrents of all samples under irradiation of a Xe lamp ($\lambda > 400$ nm).

3.4 Photocatalytic performance

Photocurrent test can provide the evidence for the separation rate of the photogenerated electron-hole pairs in photocatalysts, the transient photocurrent measurement and the photocurrent response versus different monochromatic light were conducted.[43-45] **Figure** 6a,b show the transient photocurrent curves of the as-prepared samples. Under chopped irradiation of a Xe lamp ($\lambda > 400$ nm), both the photocurrents and dark currents for all the samples can immediately reach the equilibrium state, demonstrating the intrinsic photoresponse ability of these semiconductor materials. Compared with the pristine PC-TiO_2, the photocurrents of the binary Bi_2MoO_6/PC-TiO_2 nanocomposites are dramatically improved, suggesting that the introduction of Bi_2MoO_6 component favors the rapid separation and transfer of photogenerated carriers. However, when the molar percentage of Bi_2MoO_6 reaches 20%, the photocurrent slightly decreases, which may be assigned to the light-shielding effect of high ratio of Bi_2MoO_6.[6, 10] For the ternary samples, the addition of Pt leads to the further promoted photocurrent intensity as the conductive Pt on the catalyst surface could promote the transfer of photo-induced electrons. Notably, the photocurrent reduces as the molar percentage of Pt over 1%, which is attributed to the partial carriers recombination because of the high Pt concentration. Among these photocatalysts, the 1P-10B-T sample exhibits the highest photocurrent intensity and is expected for a higher photocatalytic performance. The photocurrent responses versus different monochromatic light of PC-TiO_2, 10B-T and 1P-10B-T samples are depicted in **Figure** 6c. PC-TiO_2 shows the weak photocurrent response in the visible region due to its intrinsic wide band gap. For the binary 10B-T, the increased photocurrents in both visible and UV ranges are attributed to the photosensitive effect of Bi_2MoO_6. The ternary 1P-10B-T photocatalyst presents further enhanced photoresponse and its photocurrent is 200 times higher than that of the pristine PC-TiO_2 under 550nm monochromatic light irradiation. The detailed photocurrent values of all samples at 180s are presented to give the intuitive evidence of the photogenerated carriers separation rates (**Figure** 6d). The above results further illustrate that the introduction of Bi_2MoO_6 and Pt improves the visible light response ability and accelerates the separation and transfer of photogenerated electron-hole pairs. The photoluminescence (PL) test was also performed to investigate the separation rate of the photogenerated electron-hole pairs. The PL spectra of

PC-TiO$_2$, 10B-T and 1P-10B-T are presented in **Figure** S5. Compared with PC-TiO$_2$, 10B-T and 1P-10B-T show the significantly reduced PL intensities, indicating that the formed heterojunctions between Bi$_2$MoO$_6$ and PC-TiO$_2$ can effectively promote the separation of electron-hole pairs and the conductive Pt facilitates the transfer of electrons. The 1P-10B-T showing the weakest PL intensity demonstrates the fastest electron-hole pairs separation rate. Moreover, the electrochemical impedance spectroscopy (EIS) of PC-TiO$_2$, 10B-T and 1P-10B-T were investigated and shown in **Figure** S6, the reduced diameters of the Nyquist circle of 10B-T and 1P-10B-T compared with that of PC-TiO$_2$ imply that the impedance of charge transfer in 10B-T and 1P-10B-T is significantly reduced, benefiting for the enhanced photocatalytic activity. 1P-10B-T gives the smallest diameters of the Nyquist circle. The conclusion is well consistent with photocurrents and PL results.

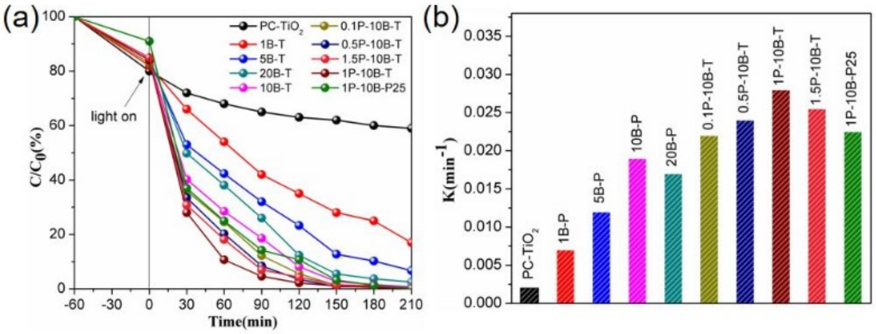

Figure 7 (a) The variation of RhB concentrations (C/C$_0$) with UV-Visible irradiation time over different photocatalysts (b) The kinetics of RhB degradation with photocatalysts.

Photocatalytic activity of the as-prepared samples was evaluated towards the RhB degradation used as photocatalytic activity probe reaction. The photocatalytic efficiency is defined as C/C$_0$, where C$_0$ and C are the initial concentration and the concentration of RhB during the reaction time, respectively. Before the light irradiation, all the samples were stirred in RhB solution under dark box for 1h. The variation of RhB concentrations (C/C$_0$) with visible light irradiation time over different photocatalysts are presented in **Figure** 7a. The as-prepared 3DOM structural samples show an obvious absorption effect because the 3DOM structure favors for the absorption of RhB under dark environment.[30] PC-TiO$_2$ exhibits very low photocatalytic activity, with only 30% of RhB being degraded in 60 min, due to its limited absorption in the visible region.[26-28] The improved photocatalytic performances of binary Bi$_2$MoO$_6$/PC-TiO$_2$ photocatalysts can be attributed to the effective interfacial charge transfer between Bi$_2$MoO$_6$ and PC-TiO$_2$ and improved light harvesting in the visible light range. As the molar percentage of Bi_2MoO_6 is higher than 10%, the photocatalytic rate for RhB degradation decreases because the excess Bi_2MoO_6 adhered in the PC-TiO_2 could block the transfer of molecule and photocatalytic process was thus partially restricted. This result is in good agreement with previous reports.[12] The photocatalytic activity of the ternary nanocomposites is further improved. For the 1P-10B-T photocatalyst, the co-catalyst Pt plays significant role in photocatalytic degradation, about 82% of RhB is degraded within 60 min and almost totally degraded for 1.5 h, which is higher than the results previously reported use same kind of photocatalysts.[6-8] When the molar percentage of Pt is higher than 1%, the photocatalytic activity is seen to decrease because the excess Pt conversely promotes electron-hole pairs recombination. The corresponding apparent reaction kinetic constants were calculated and displayed in **Figure** 7b. It is found that 1P-10B-T presents 10 times higher kinetic constant than that of PC-TiO_2, indicating the outstanding photocatalytic performance of the ternary photocatalyst. The photocatalytic stability test of the 1P-10B-T photocatalyst was conducted and shown in **Figure** S7. The photodegradation rate keeps similar level after five consecutive cycles, implying that 1P-10B-T photocatalyst possesses high chemical and physical stability. The SEM image in **Figure** S8 suggests that the morphology of 1P-10B-T has no major change after the cycles.

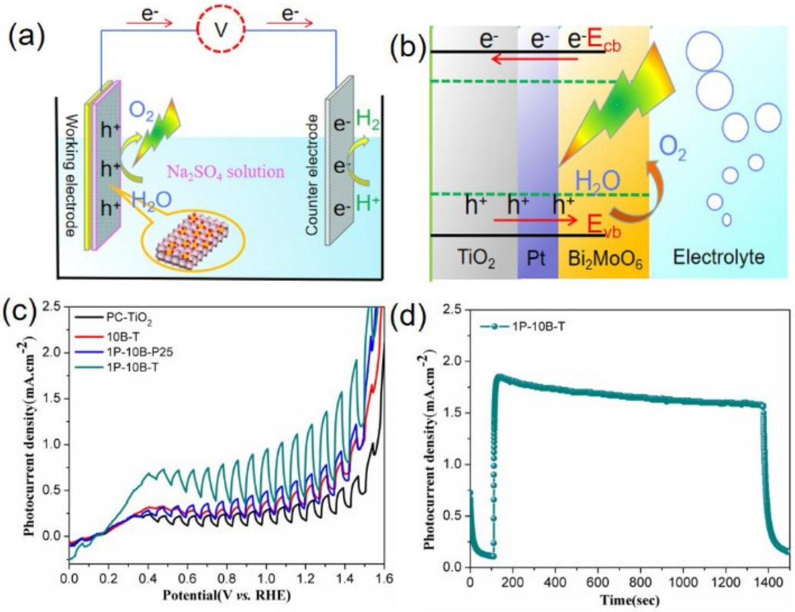

Figure 8 (a) Schematic diagram illustrating the working mechanism of 1P-10B-T based photoelectrode for PEC water splitting (b) Energy diagrams for the photoinduced charge transfer based on the 1P-10B-T photoanode (c) Current-voltage (I-V) curves of PC-TiO_2, 10B-T, 1P-10B-T and 1P-10B-P25 photoelectrode under chopped visible light in 0.5 M Na_2SO_4 solution (d) Time-dependence photocurrent density of 1P-10B-T film under AM 1.5G illumination.

From all above results, it is clearly that these ternary 3DOM-Pt/Bi_2MoO_6/TiO_2 nanocomposites possess all the necessary properties as high performance photocatalysts owing to their unique structural, optical and electronic properties. The novel ternary catalysts have been used in PEC water splitting.[42-43] The 1P-10B-T which exhibits the best photocatalytic performance in degradation of RhB was used as representative sample. **Figure** 8a depicts the working mechanism of 1P-10B-T based photoelectrode for PEC water splitting. The photogenerated electrons are transported to the counter electrode for water reduction and water oxidation is conducted on the working electrode. **Figure** 8b presents the energy diagrams for the photoinduced charge transfer based on the 1P-10B-T photoanode, O_2 could be generated on photoanode due to the oxidation of H_2O. The unique 3DOM structure of 1P-10B-T not only increases the accessible surface area, but also accelerates the hole transfer to the semiconductor/electrolyte interface, leading to more efficient water oxidation kinetics. The PEC performance of the as-prepared samples were detected using the linear sweep current-voltage (LSV) method under alternating on and off conditions under AM 1.5G illumination. As shown in **Figure** 8c, the photocurrents of the PC-TiO_2, 10B-T, 1P-10B-T and 1P-10B-P25 photoelectrodes all rapidly increase when the light is on and drop when the light is off over a wide potential range, indicating that the photocurrents are generated under irradiation. The weak photocurrent for the PC-TiO_2 is ascribed to its low electron transfer ability and limited light absorption, which is consistent with the previously reports[16-18]. Remarkably, the photocurrent of 1P-10B-T is much higher than that of PC-TiO_2, 10B-T and 1P-10B-P25 in the whole potential range. The photocurrents are 0.368, 0.531, 1.238 and 0.654 mA/cm^2 for PC-TiO_2, 10B-T, 1P-10B-T and 1P-10B-P25 at 1.23 V, respectively. The photocurrent at 1.23 V (versus RHE) of 1P-10B-T is about 3.4 times higher than that of PC-TiO_2. The onset photocurrent potentials are 0.33 and 0.29 V for PC-TiO_2 and 1P-10B-T photoelectrodes, respectively (**Figure** S9). The slightly negative shift for 1P-10B-T is attributed to the intimate contact of Bi_2MoO_6 and PC-TiO_2, which is beneficial for the fast transfer of the photoinduced holes from semiconductor to the reaction interface[40]. The photocurrent densities of all the as-prepared photocatalysts based photoelectrodes at 1.23 V under AM 1.5G illumination are presented in **Figure** S10. It is clearly seen that the 1P-10B-T sample presents the highest photocurrent density. The stability of 1P-10B-T photoelectrode in

PEC process was tested and shown in **Figure** 8d, the photocurrent density has no apparently change after 1000 s run, illustrating an excellent stability of the 1P-10B-T photoelectrodes. The ternary nanocomposites with 3DOM structure show much better PEC water splitting performance than that of 1P-10B-P25 which in its turn is better than binary composites and PC-TiO_2. Among these ternary nanocomposites, 1P-10B-T gives the best performance.

3.5 Mechanism

In order to acquire a deeper understanding for the excellent photocatalytic and PEC performance of the ternary photocatalysts, it is important to analyze the thorough separation and transfer process of photoinduced electron-hole pairs and the electronic structures of the photocatalysts. The Mott-Schottky characterization and XPS valence band spectroscopy analysis were conducted to study the band structure of the ternary photocatalyst.[14] The positive slopes of the Mott-Schottky plots in **Figure** S11a demonstrate the n-type semiconducting characters of both Bi_2MoO_6 and PC-TiO_2. The valence band positions of the materials can be determined by XPS valence band spectroscopy (**Figure** S11b), which implies that the valence bands of Bi_2MoO_6 and PC-TiO_2 are 1.72 and 2.91 V, respectively. The CB and VB positions for Bi_2MoO_6 and PC-TiO_2 could be quantitatively calculated as the band gap could be easily obtained from the the plot of $(\alpha h\nu)^2$ versus bandgap energy in **Figure** 6c. **Table** S3 lists the exact CB and VB position values for Bi_2MoO_6 and PC-TiO_2. Based on the above results and discussion, the charge transfer process is proposed to better understand the enhanced photocatalytic and PEC activities of the ternary photocatalyst under visible light and UV-Vis light irradiation.

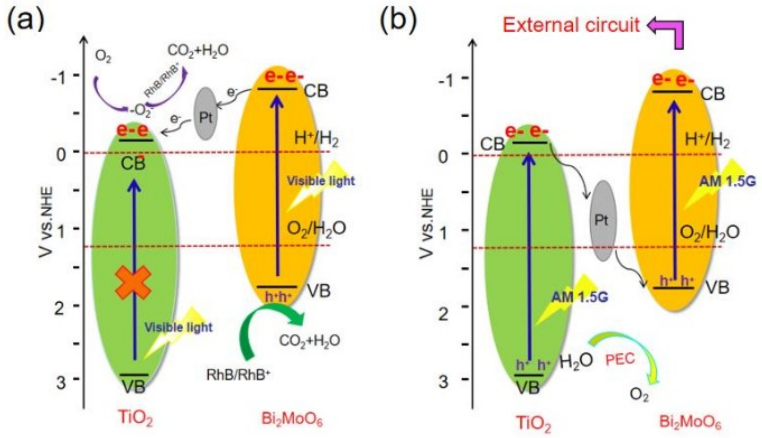

Figure 9 (a) Photocatalytic mechanism of Pt/Bi_2MoO_6/PC-TiO_2 nanocomposite under visible light irradiation. (b) PEC water splitting mechanism of Pt/Bi_2MoO_6/PC-TiO_2 nanocomposite under AM 1.5G illumination.

As shown in **Figure** 9a, when the ternary photocatalyst is irradiated under visible light, the Bi_2MoO_6 can be excited while the TiO_2 could not because of its wide band gap. The photogenerated electrons on Bi_2MoO_6 could be prone to transfer to the conduction band of TiO_2, the accumulated electrons on the CB of TiO_2 can capture the adsorbed O_2 and reduce it to O^{2-} with subsequent transformation of water molecules into hydroxyl radicals for the oxidation of dye molecules. While, the holes on the VB of Bi_2MoO_6 coupled with H_2O to form hydroxyl radicals OH•. The formed OH• active species could also degrade RhB molecules into final products (H_2O and CO_2).[27] Moreover, the co-catalyst Pt could facilitate the migration of electrons and accelerate the photocatalytic reaction process. When the ternary photocatalyst was used in PEC water splitting system under AM 1.5G illumination (**Figure** 9b), both Bi_2MoO_6 and PC-TiO_2 were excited to supply the electron-hole pairs. The photogenerated electrons of PC-TiO_2 would transfer to the valence band of Bi_2MoO_6 through a Pt bridge, and then couple with the holes of Bi_2MoO_6, which can separate the electrons and holes effectively, forming the typical electron-transfer pathway of Z-scheme photocatalyst. The water oxidation reaction is conducted on the VB of PC-TiO_2 and O_2 can be generated on photoanode. The electrons on the VB of PC-TiO_2 were transported to the counter electrode thorough external circuit to participate H_2 evolution reaction. As a result, the promoted separation efficiency of photogenerated carriers can be achieved to enhance the PEC efficiency of the ternary photocatalysts.[43]

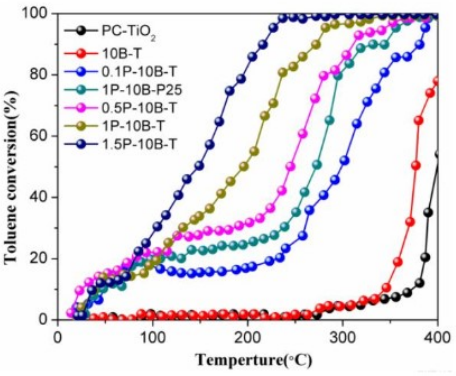

Figure 10. The thermal-catalytic performances for toluene degradation of the series of samples.

The volatile organic compounds (VOCs) are major contributors to the atmospheric pollution. The catalytically aided oxidation is an efficient method to decompose the VOCs.[46-48] Decreasing the temperature of the degradation processes reducing energy costs is highly desirable. Lots of ways such as noble metals loading and metal atoms doping have been conducted to decrease reaction temperature. Herein, we used the prepared ternary catalysts for the catalytic decomposition of toluene used as probe molecule of VOCs. **Figure** 10 shows toluene conversion curves over the as-prepared catalysts between 20 and 400°C. The toluene is totally converted into CO_2 over as-prepared catalysts. From the conversion curves, we can clearly see that the ternary nanocomposites exhibit a drastically increased catalytic performance towards toluene total oxidation. With increasing the Pt amounts, the catalytic performance was gradually increased and the order of catalytic performance of these samples is as follows: 1.5P-10B-T > 1P-10B-T > 0.5P-10B-T > 1P-10B-P25 > 0.1P-10B-T > 10B-T > PC-TiO_2. Compared with the binary 10B-T and 1P-10B-P25, the ternary catalysts based on 3DOM TiO_2 exhibited much higher activity due to the noble metal loading and the more reaction sites from the 3DOM structure. Among these catalysts, 1.5P-10B-T presents the best catalytic performance. These results indicate that the noble metal loading and 3DOM favored the enhanced the thermal-catalytic activity of the TiO_2.

4. Conclusion

A series of novel ternary photocatalysts with 3DOM structure (Pt/Bi_2MoO_6/PC-TiO_2) have been successfully synthesized. The ternary nanocomposites showed the outstanding performances in visible light photocatalytic degradation of RhB and PEC water splitting due to the combined effects of enhanced light harvesting, abundant reactive sites, facile reactants transfer and efficient charges-holes pair separation. Through optimizing the loading amounts of Pt and Bi_2MoO_6, the optimal ternary catalyst was determined. It was found that the 1%Pt/10%Bi_2MoO_6/PC-TiO_2 exhibited the highest photocatalytic RhB degradation rate and PEC water splitting activity, which are 10 and 3.4 times higher than that of PC-TiO_2 photocatalyst, respectively. Moreover, the charge transfer mechanism and band gap configuration of the ternary Pt/Bi_2MoO_6/PC-TiO_2 composites have been proposed and the results suggested that the formed heterostructure favored the charges separation and inhibited the recombination of photogenerated electrons and holes, thereby facilitating the improvement of photocatalytic degradation and PEC water splitting performances. In addition, we also applied the ternary samples for catalytic toluene decomposition. Interestingly, the ternary nanocomposites also showed much higher efficiencies in catalytic decomposition than that of PC-TiO_2 and binary nanocomposites. This work highlights the potential use of multi-component semiconductors with different band gaps and unique 3DOM structure as high efficient visible light photocatalyst, electrocatalyst and thermal-catalyst.

Acknowledgements

Y. Ding thanks the financial support from the China Scholarship Council (201808310127). This project was financially supported by the Foundation of Natural Science (No. 61905159). This work is financially supported by National Natural Science Foundation of China (U1663225) Program for Changjiang Scholars and Innovative Research Team (IRT_15R52) and this research was supported by the project "DepollutAir" of Interreg V France-Wallonie-Vlaanderen.

Conflict of Interest

The authors declare no conflict of interest.

References

[1] Zhao, H, Hu, Z, Liu, J, Li, Y, Wu, M, Van Tendeloo, G, Su, B, *Nano Energy.* 2018, 47, 266.

[2] Lin, B, Yang, G, Wang, L, *Angew. Chem., Int. Ed* 2019, 58, 4587.

[3] Lin, B, Yang, G, Yang, B, Zhao, Y, *Appl. Catal., B* 2016, 198, 276.

[4] Yu, K, Zhang, C, Chang, Y, Feng, Y, Yang, Z, Yang, T, Lou, L, Liu, S, *Appl. Catal., B* 2017, 200, 514.

[5] Zhao, H, Wu, M, Liu, J, Deng, Z, Li, Y, Su, B, *Appl. Catal., B* 2016, 184, 182.

[6] Chang, Y, Yu, K, Zhang, C, Yang, Z, Feng, Y, Hao, H, Jiang, Y, Lou, L, Zhou, W, Liu, S, *Appl. Catal., B* 2017, 215, 74.

[7] Xu, M, Chen, Y, Qin, J, Feng, Y, Li, W, Chen, W, Zhu, J, Li, H, Bian, Z, *Environ. Sci. Technol* 2018, 52 , 13879.

[8] X. Ren, Z. Hu, J. Jin, L. Wu, C. Wang, J. Liu, F. Liu, M. Wu, Y. Li, G. V. Tendeloo, B. Su, ACS Appl. Mater. Inter. 2017, 9, 29687.

[9] Loryuenyong, V, Jarunsak, N, Chuangchai, T, Buasri, A, *Adv Mater Sci Eng* 2014, 2014, 1.

[10] M. Zhou, S. Wang, P. Yang, C. Huang, X. Wang, ACS Catal. 2018, 8, 4928.

[11] Zhang, YC, Li, J, Zhang, M, Dionysiou, DD, *Environ. Sci. Technol* 2011, 45, 9324.

[12] Zhang, H, Lv, X, Li, Y, Wang, Y, Li, J, *ACS Nano* 2009, 4, 380.

[13] Liang, N, Zai, J, Xu, M, Zhu, Q, Wei, X, Qian, X, *J. Mater. Chem. A* 2014, 2, 4208.

[14] Xu, J, Wang, W, Sun, S, Wang, L, *Appl. Catal., B* 2012, 111, 126

[15] Qi, D, Lu, L, Xi, Z, Wang, L, Zhang, J, *Appl. Catal., B* 2014, 160, 621.

[16] Feng, Y, Li, H, Ling, L, Yan, S, Pan, D, Ge, H, Li, H, Bian, Z, *Environ. Sci. Technol* 2018, 52, 7842.

[17] K. Lan, R. Wang, Q. Wei, Y. Wang, A. Hong, P. Feng, D. Zhao, *Angew. Chem., Int. Ed* 2020, 59, 17676-17683.

[18] Tong, R, Liu, C, Xu, Z, Kuang, Q, Xie, Z, Zheng, L, *ACS Appl. Mater. Interfaces* 2016, 8, 21326.

[19] T. Zhao, P. Qiu, Y. Fan, J. Yang, W. Jiang, L. Wang, Y. Deng, W. Luo, *Adv Sci* 2019, 6, 1902008.

[20] Zhang, X, Liu, Y, Lee, S, Yang, S, Kang, Z, *Energy Environ. Sci* 2014, 7, 1409.

[21] Dai, Z, Qin, F, Zhao, H, Ding, J, Liu, Y, Chen, R, *ACS Catal* 2016, 6, 3180.

[22] Samdani, KJ, Park, JH, Joh, DW, Lee, KT, *ACS Sustain Chem Eng* 2018, 6, 16702.

[23] Zhao, Z, Zhang, W, Sun, Y, Yu, J, Zhang, Y, Wang, H, Dong, F, Wu, Z, Bi *J. Phys. Chem. C* 120, 11889.

[24] Xue, C, Zhang, T, Ding, S, Wei, J, Yang, G, *ACS Appl. Mater. Interfaces* 2017, 9, 16091.

[25] Xiao, S, Zhang, D, Pan, D, Zhu, W, Liu, P, Cai, Y, Li, G, Li, H, *Nat Commun* 2019, 10 (1).

[26] Fang, Y, Li, X, Wang, X, *ACS Catal* 2018, 8, 8774.

[27] Pan, Z, Zhang, G, Wang, X, *Angew. Chem., Int. Ed* 2019, 58, 7102.

[28] Tian, Z, Zhang, P, Qin, P, Sun, D, Zhang, S, Guo, X, Zhao, W, Zhao, D, Huang, F, *Adv Energy Mater* 2019, 1901287.

[29] Wang, S, Chen, P, Bai, Y, Yun, J, Liu, G, Wang, L, *Adv Mater* 2018, 30, 1800486.

[30] Hejazi, S, Mohajernia, S, Wu, Y, Andryskova, P, Zoppellaro, G, Hwang, I, Tomanec, O, Zboril, R, Schmuki, P, *Electrochem Commun* 2019, 98, 82.

[31] Xu, S, Du, AJ, Liu, J, Ng, J, Sun, DD, *Int J Hydrogen Energ* 2011, 36, 6560.

[32] Wang, W, Zhu, S, Cao, Y, Tao, Y, Li, X, Pan, D, Phillips, DL, Zhang, D, Chen, M, Li, G, Li, H, *Adv. Funct. Mater* 2019, 1901958.

[33] Xiao, S, Liu, P, Zhu, W, Li, G, Zhang, D, Li, H, *Nano Lett* 2015, 15, 4853.

[34] Zhang, M, Lin, H, Cao, J, Guo, X, Chen, S, *Chem Eng J* 2017, 321, 484.

[35] Dai, F, Zai, J, Yi, R, Gordin, ML, Sohn, H, Chen, S, Wang, D, *Nat Commun* 2014, 5.

[36] Zhao, J, Tran, PD, Chen, Y, Loo, JSC, Barber, J, Xu, ZJ, *ACS Catal* 2015, 5, 4115.

[34] Wu, M, Wang, Y, Xu, Y, Ming, J, Zhou, M, Xu, R, Fu, Q, Lei, Y, *ACS Appl. Mater. Interfaces* 2017, 9, 23647.

[38] Kou, Z, Wang, T, Gu, Q, Xiong, M, Zheng, L, Li, X, Pan, Z, Chen, H, Verpoort, F, Cheetham, AK, Mu, S, Wang, J, *Adv Energy Mater* 2019, 9, 1803768.

[39] Xu, N, Li, F, Gao, L, Hu, H, Hu, Y, Long, X, Ma, J, Jin, J, N, *ACS Sustain Chem Eng* 2018, 6, 7257.

[40] Wang, Y, Sun, J, Li, J, Zhao, X, *Langmuir* 2017, 33, 4694.

[41] Fang, Y, Xu, Y, Li, X, Ma, Y, Wang, X, *Angew. Chem., Int. Ed* 2018, 57, 9749.

[42] Yang, Y, Wang, S, Jiao, Y, Wang, Z, Xiao, M, Du, A, Li, Y, Wang, J, Wang, L, *Adv. Funct. Mater* 2018, 28, 1805698.

[43] Butburee, T, Bai, Y, Wang, H, Chen, H, Wang, Z, Liu, G, Zou, J, Khemthong, P, Lu, GQM, Wang, L, *Adv Mater* 2018, 30, 1705666.

[44] Li, L, Xiao, S, Li, R, Cao, Y, Chen, Y, Li, Z, Li, G, Li, H, *ACS Appl Energy Mater* 2018, 1, 6871.

[45] Jin, J, Wang, C, Ren, X, Huang, S, Wu, M, Chen, L, Hasan, T, Wang, B, Li, Y, Su, B, *Nano Energy* 2017, 38, 118.

[46] Barakat, T, Idakiev, V, Cousin, R, Shao, GS, Yuan, ZY, Tabakova, T, Siffert, S, Total, *Appl. Catal., B* 2014, 146, 138.

[47] Chen, H, Nanayakkara, CE, Grassian, VH, *Chem Rev* 2012, 112, 5919.Rooke, JC, Barakat, T, Finol, MF, Billemont, P, De Weireld, G, Li, Y, Cousin, R, Giraudon, JM, Siffert, S, Lamonier, JF, Su, BL, *Appl. Catal., B* 2013, 142, 149.

[48] Rooke, JC, Barakat, T, Finol, MF, Billemont, P, De Weireld, G, Li, Y, Cousin, R, Giraudon, JM, Siffert, S, Lamonier, JF, Su, BL, *Appl. Catal., B* 2013, 142, 149.

Graphical Abstract

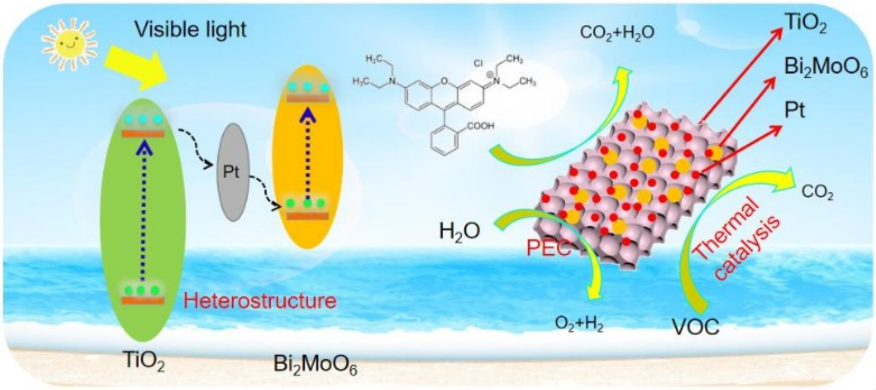

Supporting information

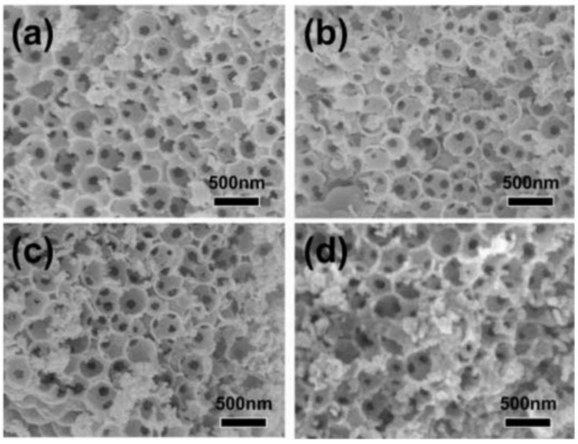

Figure S1. SEM images of the as-prepared (a) 1B-T, (b) 5B-T, (c) 10B-T and (d) 20B-T samples.

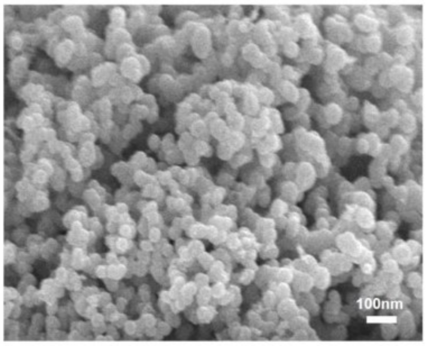

Figure S2. SEM images of the pure Bi_2MoO_6 nanoparticles

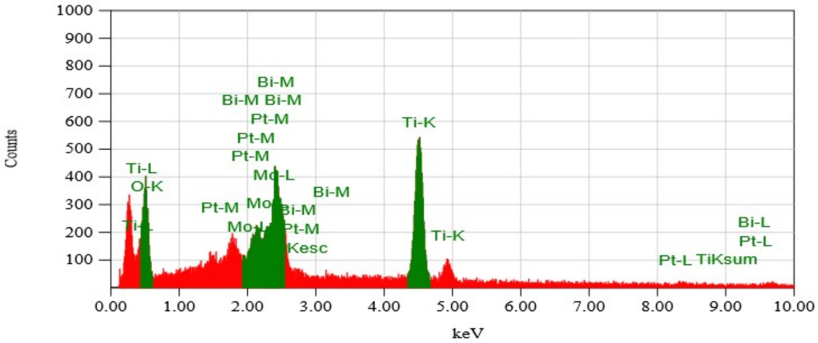

Figure S3. The EDX pattern of 1P-10B-T sample.

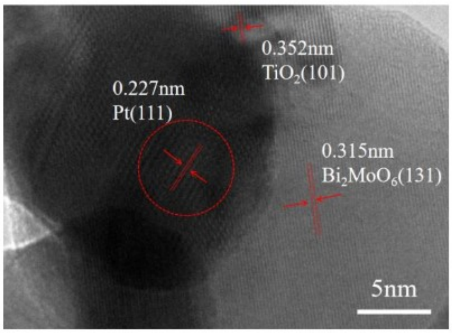

Figure S4. HR-TEM image of 1P-10B-T photocatalyst.

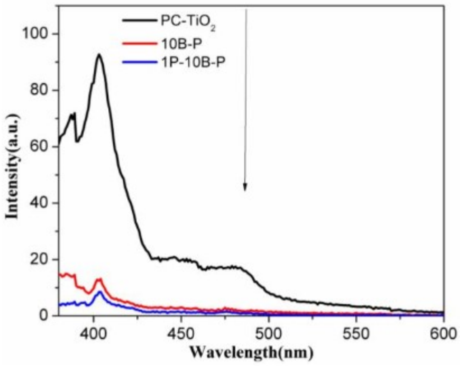

Figure S5. Photoluminescence spectra of as-prepared photocatalysts.

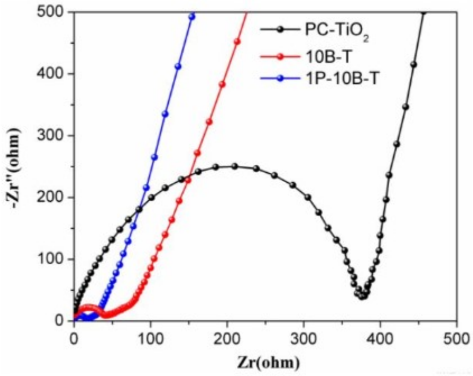

Figure S6. EIS Nyquist plots of PC-TiO$_2$, 10B-T and 1P-10B-T samples.

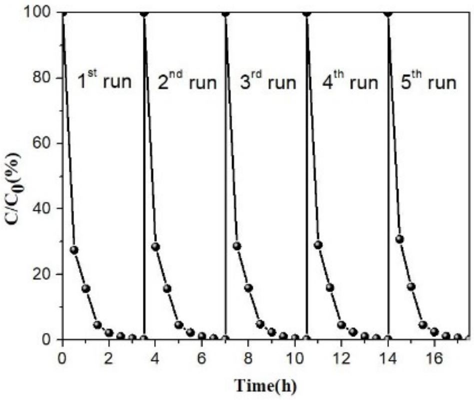

Figure S7. Photocatalytic stability tests for the RhB degradation of 1P-10B-T under visible light irradiation.

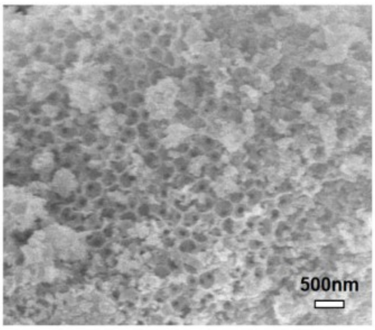

Figure S8. SEM of 1P-10B-T photocatalyst after 5 consecutive cycles for RhB degradation.

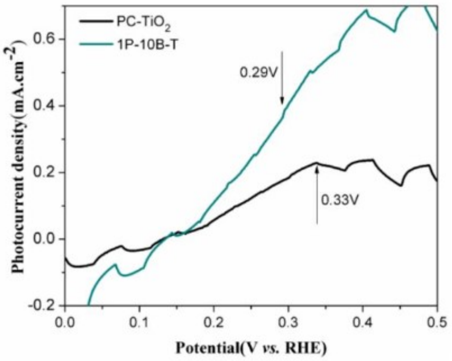

Figure S9. The onset photocurrent potentials of as prepared PC-TiO$_2$ and 1P-10B-T films.

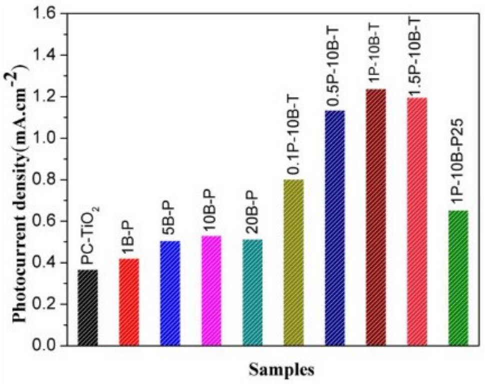

Figure S10. The photocurrent densities of all the as-prepared photocatalysts based photoelectrodes at 1.23 V under AM 1.5G illumination.

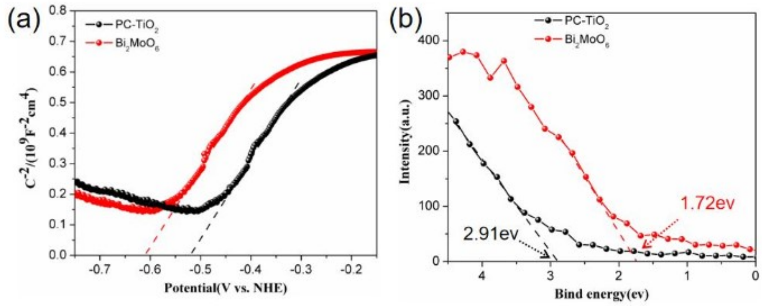

Figure S11. Mott−Schottky plots and Valence band spectra for the Bi_2MoO_6 and PC-TiO_2.

Samples	S_{BET} m^2 g^{-1}	Pore size/nm	Pore volume cm^3 g^{-1}
PC-TiO_2	42	6	0.00982
1B-T	41	9/40	0.00875
5B-T	30	9/40	0.00465
10B-T	28	10/40	0.00426

20B-T	20	10	0.00358
0.1P-10B-T	27	11/40	0.00482
0.5P-10B-T	27	11/40	0.00475
1P-10B-T	26	11/40	0.00465
1.5P-10B-T	26	12/40	0.00426
1P-10B-P25	8	9/17	0.00402

Table S1. BET specific surface area, average pore diameter, pore volume and absorbed N_2 volume of as-prepared samples

Samples	**Band gap (ev)**	**Samples**	**Band gap (ev)**
PC-TiO_2	3.07	0.1P-10B-T	2.45
1B-T	2.81	0.5P-10B-T	2.42
5B-T	2.72	1P-10B-T	2.34
10B-T	2.65	1.5P-10B-T	2.21
20B-T	2.49	Bi_2MoO_6	2.47

Table S2. The electronic energy band gaps (Eg) of all the samples.

Sample	Band gap	Evb	Ecb
Bi_2MoO_6	2.47	1.72	-0.75

PC-TiO_2	3.07	2.91	-0.16

Table S3. Values of band-gap structure parameters of Bi_2MoO_6 and PC-TiO_2 samples.

Chapter 5

Conclusions and perspectives

In this chapter, the results and conclusion for the works on the applications of porous semiconductor materials were summarized. Meanwhile, the perspective and challenges for the practical utilization of porous semiconductor materials in energy and environmental fields were outlooked and discussed.

Conclusions and perspectives

1. Conclusions

1. An innovative and facile method to synthesize hydrophilic bifunctional hierarchically assembled 2D B-doped g-C_3N_4 nanoplatelets was developed. Briefly, g-C_3N_4 is in-situ doped by B ions through a one pot thermal polymerization of a mixture of melamine and boron oxide to create bulk B doped g-C_3N_4 (bulk BCN). Nanoplatelets with about 2.5 nm in thickness are then obtained from this using an effective ultrasonic oxidative exfoliation process and are self-assembled to give a hierarchically stacked architecture of nanoplatelets. By controlling the doping amounts of B ions, visible light absorption, charge separation and surface charge transfer capacity of the obtained materials can be effectively controlled. Density functional theory (DFT) calculations further illustrate the electronic structure evolution of g-C_3N_4 upon B ions doping, which significantly broadens the absorption in the visible light range and efficiently promotes the photoinduced carrier separation for photoredox reaction. Photocatalytic tests reveal that the 2D-B-CN-4 sample shows an excellent H_2O_2 photocatalytic production rate of 4240.3 lM g^{-1} h^{-1}. The improved photocurrent density of 1.72 mA cm^{-1} at 1.23 V versus RHE under AM 1.5 G illumination for PEC water splitting was also reached. The unprecedented photocatalytic and PEC performance of hierarchically assembled 2D B-doped g-C_3N_4 nanoplatelets is attributed to the synergistic effects of B doping and hydrophilic character. Our photocatalysts demonstrate the excellent performance both in photocatalytic H_2O_2 production and in photoelectrochemical water splitting for H_2 production, thus validating our strategy towards large scale exploitation of modified g-C_3N_4 as a highly efficient photocatalyst.

2. A significantly enhanced photocatalytic H_2O_2 production with an extraordinary stability is achieved by a novel carbon-deficient 3D hierarchical porous g-C_3N_4 scaffold prepared by an innovative hydrolysis-freeze-drying-thermal treatment (HFDT) process. Specifically, the melamine powder was firstly dissolved in water, leading to the formation of cyanuric acid upon hydrolysis. Subsequently, cyanuric-acid-melamine supramolecular networks are generated through the hydrogen bonding interactions between melamine and cyanuric acid. The resultant white supramolecular polymer precipitate was freeze dried in liquid nitrogen to obtain a fluffy flaky material and then calcined. A three-dimensional (3D) hierarchical architecture made of assembled porous g-C_3N_4 nanoplatelets with abundant carbon vacancies is obtained. The carbon vacancies in the C_3N_4 lattice are found to decrease the band gap and generate mid-gap electronic levels, broadening the visible-light absorption and facilitating the photoinduced carrier separation. On the other hand, the unique 3D hierarchical porous g-C_3N_4 structure, with a larger specific surface area and abundant pores, provides numerous reactive centers and a convenient pathway for the transport of reactants and products. Density-functional theory (DFT) calculations of the band structure and partial density of states (PDOS) for B-CN and 3D-CN-C were conducted to establish the intrinsic relationship between carbon vacancies and the decreased band gap values. Electron density difference (EDD) plots show the enrichment of electron density at the uncoordinated N atom sites, hence favoring for photoreduction. Fukui function (FF) and electrostatic potential plots reveal the essential role of carbon vacancies as reaction active sites, with a strong electron affinity and radicals generating ability, all being favorable for the enhanced photocatalytic H_2O_2 generation. The above merits are responsible for the enhanced photocatalytic H_2O_2 production.

3. A series of novel ternary photocatalysts with 3DOM structure (Pt/Bi_2MoO_6/PC-TiO_2) have been successfully synthesized. A highly ordered 3DOM structure with interconnected pore of PC-TiO_2 and the average large void size about 300 nm were obtained. This unique 3DOM structure can maintain the reflectance property at different incident light angles and decrease the effect of random orientation during the photocatalytic reaction when the solution is constantly stirred. Moreover, the 3DOM structure can also facilitate the diffusion of molecules and provide sufficient reactive sites, both are beneficial to the photocatalytic reaction process. Through optimizing the loading amounts of Pt and Bi_2MoO_6, the optimal ternary catalyst was obtained. It was found that the 1%Pt/10%Bi_2MoO_6/PC-TiO_2 exhibited the highest photocatalytic RhB degradation rate and PEC water splitting activity, which are 10 and 3.4 times higher than that of PC-TiO_2 photocatalyst, respectively. Moreover, the charge transfer mechanism and band gap configuration of the ternary Pt/Bi_2MoO_6/PC-TiO_2 composites have been proposed and the results suggested that the formed heterostructure favored the charges separation and inhibited the recombination of photogenerated electrons and holes, thereby facilitating the improvement of photocatalytic degradation and PEC water splitting performances. In addition, we also applied the ternary samples for catalytic toluene decomposition. Interestingly, the ternary nanocomposites also showed much higher efficiencies in catalytic decomposition than that of PC-TiO_2 and binary nanocomposites. This work highlights the potential use of multi-component semiconductors with different band

gaps and unique 3DOM structure as high efficient visible light photocatalyst, electrocatalyst, and thermal-catalyst.

4. A general conclusion: For the chapters 2 and 3, two modified C_3N_4 samples were prepared for photocatalytic H_2O_2 generation, the 3D deficient sample showed a higher performance than that of 2D B-doped g-C_3N_4 nanoplatelets due to the merits of carbon defects and 3D structure. However, the hydrophilic properties of 2D B-doped g-C_3N_4 nanoplatelets endowed the bi-functional ability in both photocatalysis and PEC water splitting. Moreover, both B doping and defects introduction in can lead to the mid-gap electronic levels within the band structure, thus favoring carriers separation and efficient photocatalytic activity. For the chapters 4, the advantages of active materials (Pt and Bi_2MoO_6) loading and 3DOM structure are favorable for the efficient photocatalytic ability.

All in all, the unique structure and fantastic characters endow hierarchically porous semiconductors significant advantages in pollutants elimination and sustainable energy evolution. In comparison to other nanostructures, the hierarchically porous structure exhibits the superior performance in photo/electro/thermal-catalytic regions owing to the efficient mass diffusion and transfer, good electron conductivity, high surface area and plentiful surface reaction centers.

2. Perspectives and challenges

Although the great achievements and progresses have been achieved in the utilization of hierarchically porous semiconductor materials for efficient pollutants elimination and sustainable energy evolution, there are still several challenges and obstacles in this field.

1. Firstly, a series of strategies have been exploited for the fabrication of hierarchically porous semiconductor materials, the template strategy is still a predominant choice for the synthesis, thus leading to the complicated manipulation and time-consuming process. Therefore, the template free route should be paid more attention by scientists.

2. Secondly, to further elevate the performance of hierarchically porous semiconductor materials, various methods such as heterostructure construction, ions doping and noble metal particles deposition have been often adopted. Thus how to elevate the inherent performance of hierarchically porous semiconductor materials should be in-depth explored.

3. Finally, although hierarchically porous semiconductor materials actually display certainly excellent results in energy formation and pollutants elimination, it should be clear that the performance of the hierarchically porous materials is far from commercial standards yet and the large-scale preparation of uniform hierarchically porous structure is still a big problem.

List of Publications

1. **<u>Ding, Y</u>**., Maitra, S., Halder, S., Wang, C., Chen, L-H.,* & Su, B-L.,* et al. Emerging semiconductors and metal-organic compounds related photocatalysts for sustainable hydrogen peroxide production. ***Matter***, 2022, 5, 2119-2167. (**IF= 19.967**)

2. **<u>Ding, Y</u>**., Maitra, S., Li, Y.,* & Su, B-L.* et al. Hydrophilic bi-functional B-doped g-C_3N_4 hierarchical architecture for excellent photocatalytic H_2O_2 production and photoelectrochemical water splitting, ***Journal of Energy Chemistry***, 2022, 70, 236-247. (**IF= 13.599**) (chapter 2)

3. **<u>Ding, Y</u>**., Maitra, S., Barakat, T., Li, Y.,* & Su, B-L.* et al. Bi-functional Cu- TiO_2/CuO photocatalyst for large scale one-shot synergistic treatment of waste sewage containing organic and heavy metal ions. ***Science China Materials*,** 2022, doi.org/10.1007/s40843-022-2148-4. (**IF= 8.64**)

4. **<u>Ding, Y</u>**., Maitra, S., Daniel, E., Sara, B., Barakat, T., Li, Y.., & Su, B-L.* et al. Photochemical production of hydrogen peroxide by digging pro-superoxide radical carbon vacancies in porous carbon nitride, ***Cell Reports Physical Science***, 2022, 3, 100874. (**IF= 7.832**) (chapter 3)

5. **<u>Ding, Y</u>**., Huang, L., Barakat, T., & Su, B-L.* A Novel 3DOM TiO_2 Based Multifunctional Photocatalytic and Catalytic Platform for Energy Regeneration and Pollutants Degradation, ***Advanced Materials Interfaces***, 2021, 8, 2001879 (**IF= 6.389, Cover Paper**) (chapter 4)

6. **<u>Ding, Y</u>**., Maitra, S., Wang, C., Somoprova, H., Roy, S., Chen, L-H,* & Su, B-L.* et al. Vacancy defect engineering in semiconductors for solar light-driven environmental remediation and sustainable energy production, ***Interdisciplinary Materials***, 2022, 1, 213-255 (**Cover Paper**).

7. **<u>Ding, Y</u>**., Wang, C., Zheng, R., Maitra, S., Roy, S., Chen, L-H,* & Su, B-L.* et al. Three-dimensionally ordered macroporous materials for photo/electrocatalytic sustainable energy conversion, solar cell and energy storage, ***EnergyChem***, 2022, 100081. (**CiteScore= 33.4**)

8. Zheng, R., Yu, H., Zhang, X., **<u>Ding, Y</u>**., Shu, J.,* & Su, B-L..* et al. A $TiSe_2$-Graphite Dual Ion Battery: Fast Na-Ion Insertion and Excellent Stability, ***Angewandte Chemie-International Edition***, 2021, 60(34), 18430-18437. (**IF= 16.823, Cover Paper**)

9. Wang, C., Huang, H., Weng, B.,.. **<u>Ding, Y</u>**... & Roeffaers, M. B*. Planar heterojunction boosts solar-driven photocatalytic performance and stability of halide perovskite solar photocatalyst cell, ***Applied Catalysis B: Environmental***, 2022, 301, 120760. (**IF= 24.319**)

10. Wang, C., Weng, B., Keshavarz, ... **<u>Ding, Y</u>**., ... & Roeffaers, M. B.* (2022).

Photothermal Suzuki Coupling Over a Metal Halide Perovskite/Pd Nanocube Composite Catalyst, ***ACS Applied Materials & Interfaces***. 2022, 14, 17185-7194. (**IF= 10.383**)

11. Wang, C., Weng, B.,... **Ding, Y**., ... & Roeffaers, M. B.* (2022). Simultaneous photocatalytic H_2 generation and organic synthesis over crystalline-amorphous Pd nanocube decorated $Cs_3Bi_2Br_9$, ***Chemical Communications***. 2022, doi.org/10.1039/D2CC02453E. (**IF= 6.065**)

12. Rebecca, K., Savita, K.,...**Ding, Y**.,... Stephane, S*., & Su, B-L..* (2022). Boosting VOCs elimination by coupling different techniques, ***Chemical Synthesis***, 2022, 2, 13.

Conference presentations and posters

1. First China-Belgium Science and Technology Exchange Symposium	29/06/2019
2. 1st UNAMUR-SCU Molecules and Materials Science Symposium	30/07/2019
3. Twitter Poster Conference by the RSC Porous Materials Group	23/07/2020
4. International online summer school on electrocatalyst for energy applications	1/07/2020
5. NISM Annual Meeting 2020	20/11/2020
6. Virtual Symposium “Lithium Metal Anode”	18/01/2021
7. RSC Materials Chemistry Division poster symposium	20/01/2021
8. Belgian Photonics Online Meetup	23/08/2021
9. Sorption Science Symposium	23/09/2021
10. Nano-Next Generation of Sensors	24/03/2021
11. Interdisciplinary Training School for Doctoral students 2022	27/06/2022
12. NISM Scientific Meeting 2022	06/09/2022
13. 3rd bePOM conference 2022	29-30/09/2022

Acknowledgments

November 03th, 2018, I landed in Brussels Airport and started my first morning in Belgium. After a 4 years' study in the Laboratory of Inorganic Materials Chemistry (CMI) group of University of Namur, my colorful journey in Belgium is nearly finishing. I thank all the nice people I met in Belgium and appreciate them for their help and company.

First and foremost, I would like to thank my supervisor Prof. Bao-Lian Su, thank you for giving me the opportunity to do my PhD work in CMI group. I am proud of what I have been doing and achieved during my PhD period. This would not be possible without your scientific guidance and supervision. Moreover, you gave me lots of chances to conduct my research work with such great and kind colleagues in our CMI group as well as deep collaborations with other groups. I'm sincerely grateful for these opportunities that led me to do my PhD work in CMI laboratory and meet with such brilliant friends and scientists all over the world.

I also want to express my deep appreciation to Mrs. Isabelle Virlet. I understand it is not an easy work to help a shy Chinese PhD student to adapt a new life in Belgium and quickly integrate into a new group, but you are always so patient, kind, enthusiastic and willing to give me help. Your careful and patient help and guidance makes me feel at home in Belgium and CMI group. Thank you very much for maintaining the harmonious and joyful atmosphere in the lab.

I would also like to deliver my sincere thanks to my PhD thesis committee: Prof. Vincent Liègeois, Prof. Olivier Deparis from Unamur, Prof Alexandru Vlad from UCLouvain, Prof. Li-Hua Chen from WHUT and Dr. Tarek Barakat from Vocalise, who gave me lots of professional suggestion and patient guidance on my thesis.

Many thanks to Prof. Yu Li, Prof. Li-Hua Chen and Dr. Jing Liu from Wuhan University of Technology, Prof. Tawfique Hasan from University of Cambridge, Prof. Henk Vrielinck from Ghent University, Prof. Gustaaf Van Tendeloo, Prof. Sara Bals and Dr. Daniel Arenas Esteban from University of Antwerp, who gave me lots of professional suggestion on my papers and helped me with some material characterizations. I also thank Mrs. Valérie Charles for her kind help in ordering chemical products and managing devices.

My sincerely thanks goes to the CMIsts: Dr. Tarek Barakat, Dr. Minghui Sun, Dr. Li Wang, Dr Yingying Wang, Dr. Yanxin Chen, Dr. Chao Li, Dr Myriam Neumann, Dr. Cyrille Delneuville, Dr. Quentin Bizot, Dr Ivalina Trendafilvoa, Mr. Runtian Zheng, Mr. Marvin Laboureur, Mr. Miss Hongyan Li, Mr. Pengcheng Xing, Mr. Thomas Madanu, Mr. Parrick Sangier, Miss Jamila Igouzoln, Mr. Xikun Zhang, Miss Liuxi Yang. I am really grateful to them for their friendship and the enthusiastic help during my PhD stage in CMI group and for their amiable attitude making me feel highly welcomed. None of my work would be achieved without your kind help. I also thanks to Dr. Chunhua Wang at KU Leuven for his kind help of some characterization and discussion. I also thanks to Dr. Subhasis Roy and Mr. Soumyajit Maitra at University of Calcutta for their kindly help in theoretical calculations. I also thanks to Dr. Meiyu Zhang at Lanzhou University and Mr. Genwei Zhang at Fudan University for their kind help in materials characterizing and experience sharing.

I am also grateful to the fund supporting from the Chinese Scholarship Council (CSC), which support all the living fees and a round trip flight tickets from China to Belgium.

Most importantly, I would also like to deliver my greatest thanks to my family for their loving considerations and great confidence in me all through these years. Especially for my parents and sister, who are always giving their persistent support to me in pursuing my dream.

Thank you all for everything in Belgium! My beloved colleagues and friends, I wish all the best to your future!

Yang Ding

October, 2022, Namur